Microwave ablation of uterine fibroids

by

Ghina Zia

B.S., National University of Sciences & Technology Pakistan, 2013
M.S., National University of Sciences & Technology Pakistan, 2017

AN ABSTRACT OF A DISSERTATION

submitted in partial fulfillment of the requirements for the degree

DOCTOR OF PHILOSOPHY

Mike Wiegers Department of Electrical & Computer Engineering
Carl R. Ice College of Engineering

KANSAS STATE UNIVERSITY
Manhattan, Kansas

2021

Abstract

Uterine fibroids are the most common tumors of the uterus, with a ~70-80% lifetime prevalence in women of childbearing age. Uterus sparing procedures are of increasing interest for the treatment of fibroids to avoid surgical complications, preserve fertility, and reduce treatment costs. Image-guided microwave thermal ablation is under investigation as a minimally-invasive alternative to gold-standard hysterectomy, offering potential to provide symptom alleviation while preserving the patient's fertility. This dissertation presents studies towards the technical feasibility assessment of hysteroscopic transcervical microwave ablation (MWA) technology for treating uterine fibroids with the objective of achieving localized thermal destruction of fibroids while precluding thermal damage to adjacent healthy tissues.

Computational models, a powerful tool for the design and evaluation of candidate ablation technologies, require accurate specification of tissue dielectric properties and how these properties vary as a function of temperature during an ablation procedure. The dielectric properties of uterine fibroids within the microwave frequency range have not been previously reported, thus stunting the development of accurate modeling tools. This study presents, for the first time, the dielectric properties within the microwave frequency range (500 MHz to 6 GHz) of human uterine fibroids excised following hysterectomy procedures, and their variation across temperatures ranging between 23–150 °C. At room temperature (23 °C), values of ε_r ranged between 44.5-57.5 units with a decreasing trend seen at higher frequencies and σ_{eff} varied between 0.91-6.02 Sm^{-1} with an increasing trend at higher frequencies. At temperatures close to the water vaporization point, ε_r, drops considerably i.e. to 12-14% of its baseline values for all measured frequencies. The σ_{eff} initially rises till 98 °C and then falls to 11-13% of its baseline values at 125 °C for frequencies $\leq$ 2.45 GHz. The σ_{eff} follows a decreasing trend for frequencies > 2.45 GHz and drops to ~ 6 % of

its room temperature values. Furthermore, parametric models of temperature and frequency dependent dielectric properties of uterine fibroids were presented, which can be readily used in computer simulations for accurate modeling of MWA.

While MWA applicators are in clinical use for a variety of indications, existing antenna designs are not well suited to ablation of 1 – 3 cm type 2 uterine fibroids. Currently 2.45 GHz applicators are used for the MWA of fibroid tissues; these antennas typically have longer active lengths (~7-15 mm) compared to the radius of type 2 fibroids. A higher frequency 5.8 GHz applicator, which was expected to reduce the antenna radiating length was investigated. A 5.8 GHz water-cooled MWA applicator, suitable for insertion into targeted fibroids via the instrument channel of a hysteroscope, was designed for the treatment of small fibroids (1-3 cm diameter) using electromagnetic–bioheat transfer simulations. The prominent features of this applicator are applicator diameter (2.15 mm < hysteroscope operating channel diameter ~ 3 mm), radiating length (2.5 mm < radius of 1 cm fibroid), internal impedance matching (antenna return loss < -10 dB i.e. around 90% power transferred to antenna), a balun for achieving near spherical ablation profiles to align with the shape of the fibroids, and a rapid transition from ablated to non-ablated regions, in the range ~2-5 mm for 1 – 3 cm fibroids, respectively. The fabricated applicator was tested in *ex vivo* animal tissue for the experimental assessment of computer models. To eliminate the sources of variability which are inherent in a biological tissue and to reduce the error in the placement of monitoring temperature sensors, tissue mimicking phantoms were fabricated and their thermal and electrical properties were experimentally characterized. Notably, a thermo-chromic phantom was developed for assessment of thermal ablation patterns from candidate ablation technologies. Changes in phantom color were assessed following baseline heating studies

in a temperature-controlled bath. During MWA experiments, spatial extents of color changes in phantoms were used to characterize thermal profiles.

Pre-clinical studies of ablation procedures presume central positioning of applicators within the targeted tissue; however, precise central placement of the applicators within the fibroids may not be feasible in clinical practice due to limited control of instruments through the hysteroscope. The impact of MWA applicator insertion angle and position within targeted uterine was assessed for the treatment of type 2 submucosal fibroids. Using experimentally validated finite element computer models, the sensitivity of ablation outcome was assessed with respect to applicator insertion angles (30°, 45°, 60°), depth and offset from the fibroid center (±1 mm for 1 cm fibroid and ±2 mm for 3 cm fibroid) while constraining the thermal dose in adjacent myometrium i.e. 40 cumulative equivalent minutes at 43 °C (CEM43). Simulations indicate that MWA is capable to deliver ~ 34.1- 67.9% (within 30 - 50 s) and ~ 34.9 - 83.6% (within 140 - 400 s) ablation volumes in 1 cm and 3 cm fibroids with applied power of 15 W and 35 W, respectively, while limiting thermal dose to surrounding normal tissues to 40 CEM43. This study demonstrates that 1-3 cm fibroids can be safely ablated when applicator position is within 30-60° insertion angle and ±1-2 mm displacement from the center of the fibroid.

To summarize, this dissertation presents development of computational and experimental platforms for assessing the candidate technologies for MWA of uterine fibroids. A 5.8 GHz antenna for the ablation of small (≤ 3 cm) type 2 uterine fibroids was also demonstrated. The methodology introduced in this dissertation can be extended to the design of site-specific MWA technologies for other indications.

Microwave ablation of uterine fibroids

by

Ghina Zia

B.S., National University of Sciences & Technology Pakistan, 2013
M.S., National University of Sciences & Technology Pakistan, 2017

A DISSERTATION

submitted in partial fulfillment of the requirements for the degree

DOCTOR OF PHILOSOPHY

Mike Wiegers Department of Electrical & Computer Engineering
Carl R. Ice College of Engineering

KANSAS STATE UNIVERSITY
Manhattan, Kansas

2021

Approved by:

Major Professor
Dr. Punit Prakash

Copyright

Abstract

Uterine fibroids are the most common tumors of the uterus, with a ~70-80% lifetime prevalence in women of childbearing age. Uterus sparing procedures are of increasing interest for the treatment of fibroids to avoid surgical complications, preserve fertility, and reduce treatment costs. Image-guided microwave thermal ablation is under investigation as a minimally-invasive alternative to gold-standard hysterectomy, offering potential to provide symptom alleviation while preserving the patient's fertility. This dissertation presents studies towards the technical feasibility assessment of hysteroscopic transcervical microwave ablation (MWA) technology for treating uterine fibroids with the objective of achieving localized thermal destruction of fibroids while precluding thermal damage to adjacent healthy tissues.

Computational models, a powerful tool for the design and evaluation of candidate ablation technologies, require accurate specification of tissue dielectric properties and how these properties vary as a function of temperature during an ablation procedure. The dielectric properties of uterine fibroids within the microwave frequency range have not been previously reported, thus stunting the development of accurate modeling tools. This study presents, for the first time, the dielectric properties within the microwave frequency range (500 MHz to 6 GHz) of human uterine fibroids excised following hysterectomy procedures, and their variation across temperatures ranging between 23–150 ℃. At room temperature (23 ℃), values of ε_r ranged between 44.5-57.5 units with a decreasing trend seen at higher frequencies and σ_{eff} varied between 0.91-6.02 Sm^{-1} with an increasing trend at higher frequencies. At temperatures close to the water vaporization point, ε_r, drops considerably i.e. to 12-14% of its baseline values for all measured frequencies. The σ_{eff} initially rises till 98 ℃ and then falls to 11-13% of its baseline values at 125 ℃ for frequencies $\leq$ 2.45 GHz. The σ_{eff} follows a decreasing trend for frequencies > 2.45 GHz and drops to ~ 6 % of

its room temperature values. Furthermore, parametric models of temperature and frequency dependent dielectric properties of uterine fibroids were presented, which can be readily used in computer simulations for accurate modeling of MWA.

While MWA applicators are in clinical use for a variety of indications, existing antenna designs are not well suited to ablation of 1 – 3 cm type 2 uterine fibroids. Currently 2.45 GHz applicators are used for the MWA of fibroid tissues; these antennas typically have longer active lengths (~7-15 mm) compared to the radius of type 2 fibroids. A higher frequency 5.8 GHz applicator, which was expected to reduce the antenna radiating length was investigated. A 5.8 GHz water-cooled MWA applicator, suitable for insertion into targeted fibroids via the instrument channel of a hysteroscope, was designed for the treatment of small fibroids (1-3 cm diameter) using electromagnetic–bioheat transfer simulations. The prominent features of this applicator are applicator diameter (2.15 mm < hysteroscope operating channel diameter ~ 3 mm), radiating length (2.5 mm < radius of 1 cm fibroid), internal impedance matching (antenna return loss < -10 dB i.e. around 90% power transferred to antenna), a balun for achieving near spherical ablation profiles to align with the shape of the fibroids, and a rapid transition from ablated to non-ablated regions, in the range ~2-5 mm for 1 – 3 cm fibroids, respectively. The fabricated applicator was tested in *ex vivo* animal tissue for the experimental assessment of computer models. To eliminate the sources of variability which are inherent in a biological tissue and to reduce the error in the placement of monitoring temperature sensors, tissue mimicking phantoms were fabricated and their thermal and electrical properties were experimentally characterized. Notably, a thermo-chromic phantom was developed for assessment of thermal ablation patterns from candidate ablation technologies. Changes in phantom color were assessed following baseline heating studies

in a temperature-controlled bath. During MWA experiments, spatial extents of color changes in phantoms were used to characterize thermal profiles.

Pre-clinical studies of ablation procedures presume central positioning of applicators within the targeted tissue; however, precise central placement of the applicators within the fibroids may not be feasible in clinical practice due to limited control of instruments through the hysteroscope. The impact of MWA applicator insertion angle and position within targeted uterine was assessed for the treatment of type 2 submucosal fibroids. Using experimentally validated finite element computer models, the sensitivity of ablation outcome was assessed with respect to applicator insertion angles (30°, 45°, 60°), depth and offset from the fibroid center (±1 mm for 1 cm fibroid and ±2 mm for 3 cm fibroid) while constraining the thermal dose in adjacent myometrium i.e. 40 cumulative equivalent minutes at 43 °C (CEM43). Simulations indicate that MWA is capable to deliver ~ 34.1- 67.9% (within 30 - 50 s) and ~ 34.9 - 83.6% (within 140 - 400 s) ablation volumes in 1 cm and 3 cm fibroids with applied power of 15 W and 35 W, respectively, while limiting thermal dose to surrounding normal tissues to 40 CEM43. This study demonstrates that 1-3 cm fibroids can be safely ablated when applicator position is within 30-60° insertion angle and ±1-2 mm displacement from the center of the fibroid.

To summarize, this dissertation presents development of computational and experimental platforms for assessing the candidate technologies for MWA of uterine fibroids. A 5.8 GHz antenna for the ablation of small (≤ 3 cm) type 2 uterine fibroids was also demonstrated. The methodology introduced in this dissertation can be extended to the design of site-specific MWA technologies for other indications.

Table of Contents

List of Figures

List of Tables

Acknowledgements

Dedication

This work is dedicated to my beloved parents Mrs. Azmat Zohra and Mr. Ziauddin Ahmed Khan.

Preface

As a woman I can understand how difficult and painful it would be for the patients of uterine fibroids to survive with the symptoms of uterine fibroids. The occurrence of fibroids can impact a patient's reproductive health and overall quality of life and in some cases, the fertility of the patient is compromised due to this disease. Minimally invasive technologies for the treatments for fibroids are needed to provide symptom relief to the patients while preserving their fertility and preventing the surgical contraindications. In this dissertation, I tried to identify the research gaps in developing minimally invasive needle based thermal ablation technologies for uterine fibroids and proposed solutions to a few research questions by introducing the concept of transcervical hysteroscopic microwave ablations for the treatment of fibroids.

Chapter 1 - Introduction

Uterine fibroids are the most common gynecological benign tumors in females. The worldwide prevalence of uterine fibroids has been estimated to range between 4.5 - 68.6% based on the study design, method of diagnosis and population characteristics [1]. In the United States, the lifetime prevalence of uterine fibroids in women of childbearing age is ~70-80% [2]–[8]. Fibroids have a significant adverse impact on the quality of a patient's life, and can require hospitalizations and affect productivity [9][10]. 50-80% fibroids are asymptomatic [11] and frequently go undetected [5], until the patient develops symptoms like dysmenorrhea, abnormal uterine bleeding (AUB), increased pelvic/bowel pressure, weight gain, urinary incontinence, pain during intercourse, and in severe cases, can lead to complications during pregnancy/labor, miscarriages and infertility [11] [12]. Known risk factors for uterine fibroids include age, race, reproductive status, family history, diet and comorbidities (e.g. diabetes, hypertension) [1].

Fibroids are highly heterogeneous tissues in terms of their size, number, composition and location [13] [14] [15]. Fibroids normally grow inside the muscular layer (myometrium) of the uterus and can distort the morphology of the endometrial cavity. Unlike the normal myometrium which contains organized smooth muscle cells, fibroid tissues are composed of disorganized smooth muscle cells separated by varying amounts of extracellular matrix (ECM) for example fibronectin, collagen and proteoglycans [13], [16]. There can be multiple fibroids in a uterus ranging from less than a centimeter up to ~34 cm [17][16]. The broader classification of uterine fibroids is based on the anatomical location of their growth which includes; sub-mucosal (inside or adjacent to the uterine cavity), sub-serosal (at the outer wall of the uterus), intramural (within the myometrium) and intra-cavitary (attached to endometrium by a thin stalk) [14]. As illustrated

in Figure 1.1, the International Federation of Gynecology and Obstetrics (FIGO) classifies fibroids [15] based on their position within the uterine cavity or wall.

Sub-mucous
0 Pedunculated Intracavitary
1 < 50% Intramural
2 ≥ 50% Intramural

3 100% Intramural, contracts endometrium

Others
4 Intramural
5 Sub-serous ≥ 50% Intramural
6 Sub-serous < 50% Intramural
7 Sub-serous Pedunculated
8 Cervical, parasitic

Endometrium
Myometrium
Fibroid
Endometrial Cavity
Cervix
Peritoneal Cavity

Hybrid 2-5 (contains both endometrium and serosal layer) Sub-mucous and sub-serous, each with less than half diameter in the endometrial and peritoneal cavities respectively.

Figure 1.1 FIGO sub-classification system for uterine leiomyoma.

Hysterectomy, surgical removal of the uterus, is the gold standard treatment for alleviating symptoms in symptomatic fibroid patients [11]. Symptomatic fibroids (mostly submucosal fibroids) constitute ~30-40% of all hysterectomy cases in the United States [18]–[20]. Uterine artery embolization (UAE) [21] and myomectomy [22] are among the uterine-sparing treatments that may be considered for patients with symptomatic fibroids. UAE aims to occlude the uterine artery supplying a fibroid via trans-catheter embolization or laparoscopic occlusion. Myomectomy refers to surgical removal of a fibroid while trying to preserve the healthy tissues of the uterus; myomectomies may be performed via laparotomy (open surgery) [23], laparoscopy [24] or via hysteroscopy [25]. Conventional surgical treatments are invasive and require in-patient admission and general anesthesia, and are associated with a prolonged return to daily activities. The complete

resection of submucosal fibroids [25] may require multiple resections/procedures with a risk of perforating the non-target tissues [26] [27] [28], intrauterine adhesions or Asherman syndrome [29], [30] [31], fluid overload [32], and can negatively impact the reproductive health of the patient. Hence, patients desiring uterus preservation in the case of small ($\leq$ 3 cm diameter) submucosal fibroids may desire less invasive procedures like thermal ablation for the treatment of fibroids especially for type 2 fibroids ($\geq$ 50% intramural component) [33] [34] [35] [36].

Image-guided thermal ablation techniques provide a minimally-invasive alternative to gold-standard hysterectomy, with the potential for considerably less blood loss, shorter hospitalization, faster recovery rates and lower incidence of complications, adhesion formation and potential to preserve the patient's fertility. Thermal ablation techniques that have been investigated for fibroid ablation include: high intensity focused ultrasound (HIFU), radiofrequency ablation (RFA), microwave ablation (MWA), laser thermal ablation (LTA)) where the target tissue temperature is raised to temperatures >55°C [37][38]. Moreover, cryoablations have also been used for treatment of fibroids; cryoablation procedures treat fibroids by lowering the tissue temperature to -20 °C [39] [38]. During thermal ablation, cytotoxic temperatures are induced in the target tissue, leading to protein denaturation and cell death by coagulative necrosis in the fibroid tissues. The surrounding myometrium gradually starts resorbing myoma which causes shrinkage in fibroid volume thereby reducing symptoms. Unlike the treatment of malignant tumors, the goal of fibroid ablation is symptom alleviation for which 100% ablation of the fibroid tissue may not be needed [40] [41]. There is considerably more emphasis on thermal sparing of normal uterus tissue to avoid further complications [31]. The extent of thermal ablation in fibroids is typically assessed with contrast-enhanced imaging, with the ablation zone appearing as a non-perfused volume [42]. Hence, the objective of fibroid ablation treatment is to maximize the non-

perfused volume of fibroid for symptom relief [43] by inducing cytotoxic temperatures (>55-60°C [37]) in the fibroid tissue, while strictly minimizing the collateral damage to the surrounding healthy tissues of uterus [44], [45] and the organs around uterus [46] (e.g. bowel, bladder and rectum) by ideally maintaining sub-ablative temperatures in the adjacent non target tissues.

Microwave ablation (MWA) is under investigation as a minimally invasive thermal ablative approach for treatment of uterine fibroids. MWA is already in clinical use for treatment of tumors in the liver, lung and kidney [47]. MWA offers the potential of producing consistently higher tissue temperatures for larger ablation volumes in relatively short duration in highly perfused tissue. There has been a growing research interest in using MWA via percutaneous [10] [11] and transcervical [49]–[52][44], [45] approaches for the treatment of fibroids.

The shape of the ablation zone while using a water-cooled 2.45 GHz monopolar microwave applicator is elliptical, as depicted in Figure 1.2. This poses a technical challenge since the shape of fibroids is mostly spherical. For maximum ablation coverage inside the fibroid tissue, the shape of the ablation profile of the applicator should align well with the shape of the target tissue. There exists a tradeoff between ablation volume coverage inside the fibroid and the safety of the adjacent non-target tissues. Hence, there is a need of designing site specific ablation applicators whose ablation profile is well aligned with the shape of the fibroid tissue.
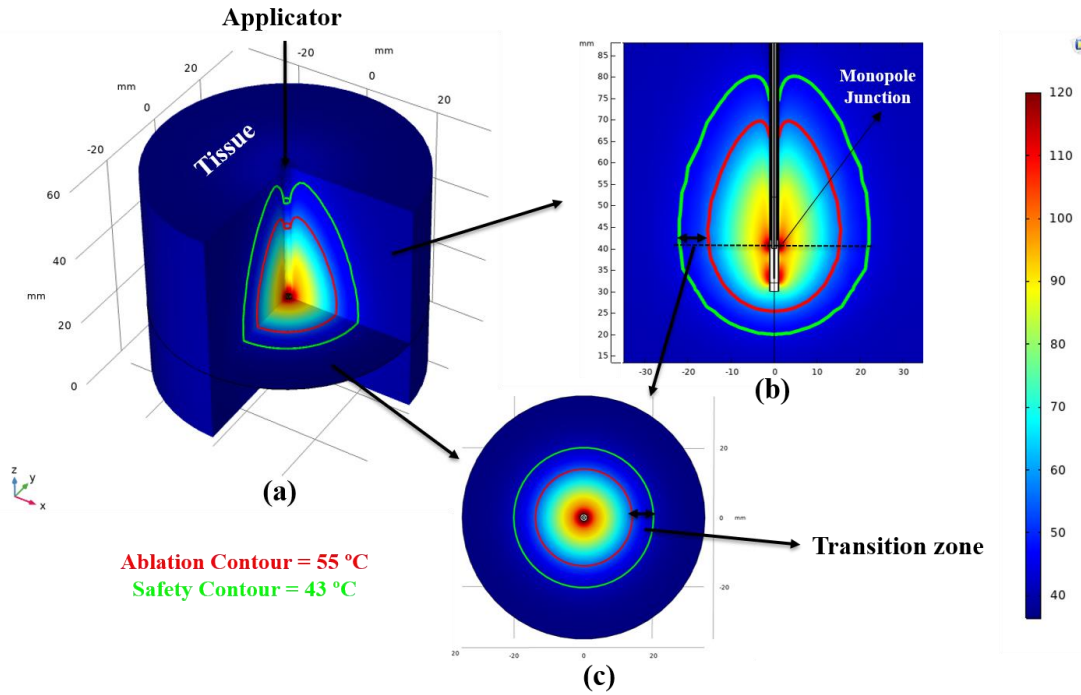
Figure 1.2 Ablation profiles of a 2.45 GHz applicator with 40 W applied power. (a) 3D illustration of applicator insertion inside the tissue and contours for ablation and safety with background temperature map, (b) Longitudinal section of the ablation profile, and (c) Axial section of ablation profile.

1.1 Research Approach

A transcervical approach for fibroid ablation offers the opportunity for a minimally invasive [53] access through a body cavity (cervical canal), thus minimizing the risk of damaging the organs adjacent to uterus (such as, rectum, bladder and intestinal tracks). Thermal sparing of adjacent tissues to the fibroid is of high priority in order to preserve the woman's ability to bear children. Transcervical microwave myolysis technique has been used in combination with microwave endometrial ablation and ultrasound guidance in previous studies [54], [55], [56], [57]. The protection of endometrium, functional layer of the uterus where the embryo implants during conception, remains a challenge in the transcervical approaches. Moreover, the myometrium (muscular layer of the uterus inside which fibroid grows) also needs to be preserved as much as
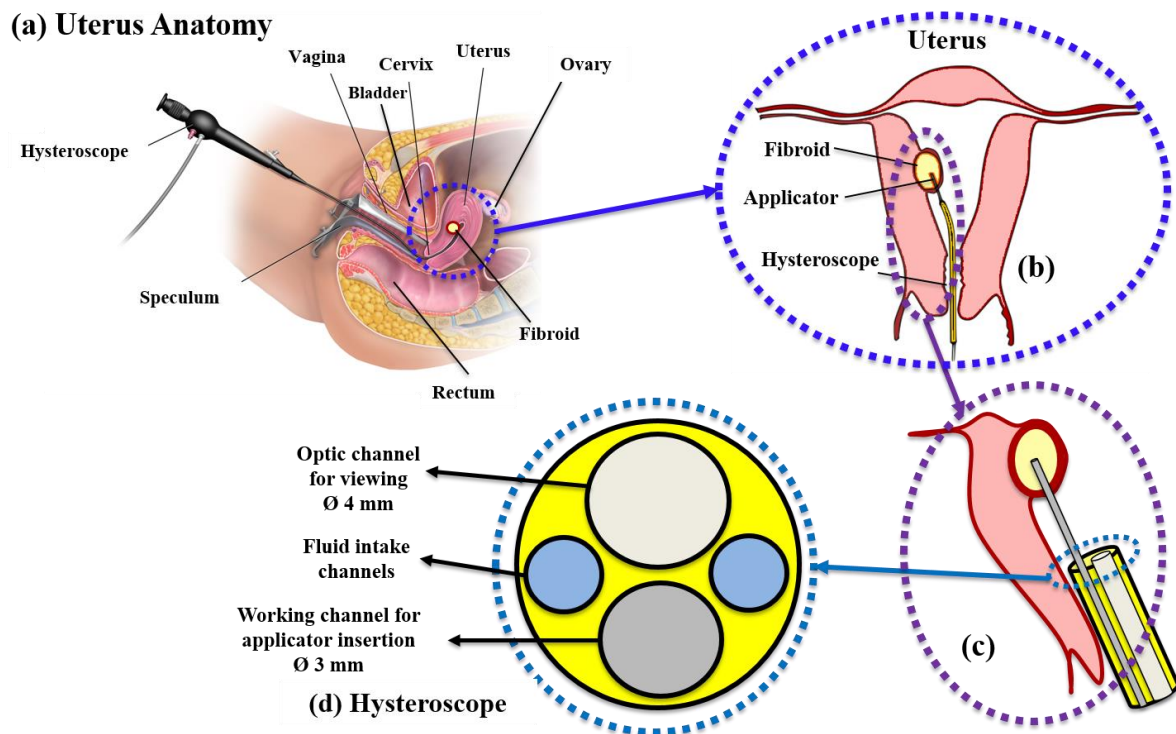
Figure 1.3 Transcervical hysteroscope microwave ablation of fibroids; (a) anatomy of uterus ([58]; https://commons.wikimedia.org/wiki/File:Hysteroscopy.png), (b) insertion of transcervical microwave applicator into the fibroid through the cervix via hysteroscope, c) a closer view of applicator insertion inside the fibroid (d) Terminal portion of hysteroscope with channels with different channels for optics, fluids and working channel for applicator insertion.

possible since it provides flexibility to the uterus to expand/contract during pregnancy/childbirth [16]. Technologies for hysteroscopy-guided ablation of fibroids via a transcervical approach are attractive for submucosal fibroids because of their reduced invasiveness compared to other approaches [53] as illustrated in Figure 1.3. Figure 1.3 (a) was reproduced from [58].

This dissertation reports on research conducted with the overall objective of developing tools and methods to drive the technical feasibility assessment of transcervical MWA.

1.2 Research Topics and Contributions

In this regards, this dissertation addresses the following research topics.

1.2.1 Dielectric property measurements of uterine fibroids

Dielectric properties determine how time-varying electromagnetic fields interact with a material. The temperature-dependent dielectric properties (relative permittivity and effective electrical conductivity) of fibroid tissue are essential for accurate computational modeling for fibroid ablation, which is an important tool for device design and assessment of procedural parameters. From the literature, it is evident that the dielectric properties of other normal/pathologic biological tissues vary considerably across frequency and dynamically with temperature during heating [59]–[64]. Since fibroids do not naturally occur in most animals, there are limited published data on dielectric properties of uterine fibroids. Studies on fibroid ablation technologies have been restricted to the use of *ex vivo* animal tissues at their device development stages [44], [65], which may not be representative of uterine fibroids. Thus, the lack of data and suitable parametric models for describing the broadband temperature-dependent dielectric properties of uterine fibroids is a significant gap in the literature.

Contributions:

We measured the broadband dielectric properties of *ex vivo* human uterine fibroids over the microwave frequency range of 0.5-6 GHz and temperatures ranging between 23-150 ℃. Fibroid tissue was obtained from a tissue bank, with samples shipped to the laboratory shortly after surgical excision. These measurements and associated parametric fits will enable modeling of microwave devices for fibroid ablation and imaging [66] across a range of frequencies. This is one of the few reports of temperature dependent dielectric property measurements of human tissue. The methodology employed in this study can be adapted for measurements of other tissues excised

from human surgeries. Furthermore, the dielectric properties measured for uterine fibroids were compared with the dielectric properties of *ex vivo* bovine muscle, a commonly used surrogate tissue [44], [65] for technologies developed to treat uterine fibroids.

This contribution is discussed in detail in Chapter 3 and in the following publication and presentation:

- G. Zia, J. Sebek, and P. Prakash, "Temperature-dependent dielectric properties of human uterine fibroids over microwave frequencies," *Biomed. Phys. Eng. Express* (under review).

- G. Zia, J. Sebek, and P. Prakash, "Broadband dielectric measurements of *ex vivo* uterine fibroid tissues over the ablative temperature range," *14th European Conference on Antennas and Propagation (EUCAP 2020),* Copenhagen, Denmark; Mar 15-20, 2020.

1.2.2 Transcervical MWA applicators for fibroids; design, testing and evaluation

MWA via hysteroscopy poses several unique challenges at the device development stage: 1) the diameter of the applicator should be small enough to fit through the working channel of a rigid hysteroscope (3 mm) and 2) the ablation profile should be well collimated to the fibroids (1-3 cm diameter) to limit damage to the adjacent endometrium and myometrium. Although MWA technology has been in clinical use for the ablation of tumors in other organs, existing MWA systems are not well suited to transcervical hysteroscopic ablation of fibroids. Firstly, the electromagnetic wavelength inside the tissue is a function of frequency and affects antenna length. The radiating monopole length of the applicator at 2.45 GHz is ~ 7-15 mm, which is considerably larger than radius of 1 cm fibroid, and would thus require insertion of the applicator past the target tissue. Secondly, the gradual fall-off of radial temperature profile from ablation zone to the surrounding tissue introduces a tradeoff between volume of fibroid ablated and damage to non-targeted tissue. Thirdly, the shape of the ablation pattern should match the shape of the fibroid

(mostly spherical) for maximizing the volume coverage of ablation inside fibroid while minimizing the damage to surrounding tissues.

To address these aforementioned challenges new MWA applicators need to be designed with an outer diameter less than the working channel of a hysteroscope (3 mm), a shorter radiating length of the antenna, provides spherical ablation pattern for 1-3 cm fibroids and a sharp transition of radial thermal profile from ablated tissue to thermally unaffected tissue to reduce the damage to adjacent tissues. Furthermore, since there are no established models to estimate the performance of candidate fibroid ablation technologies during device development, the development of experimental platforms for benchtop evaluation of MWA applicators would provide a means for systematic evaluation of candidate technologies.

Contributions:

High frequency applicators offer the opportunity for shorter antenna lengths and the temperature roll-off at the target tissue boundaries may be sharper due to smaller wavelengths and higher attenuation. Therefore, to improve the ablation outcome while minimizing the damage to adjacent tissues, we investigated microwave ablation systems operating at 5.8 GHz for central placement inside the target tissue which is well suited for MWA of fibroids via hysteroscopy and provides a nearly spherical ablation pattern inside 1-3 cm target tissue. The 5.8 GHz applicator presented in this study has some unique features well suited to the precise ablation of small uterine fibroids: 1) reduced diameter i.e. 2.15 mm < 3 mm to fit inside the hysteroscope working channel, 2) shorter radiator length = 2.5 mm (does not require penetration beyond the fibroid boundary), 3) Low reflected power using an internal impedance matching element and 4) Spherical ablation pattern, sharp thermal transition at the boundaries of fibroid and limited backward heating along the shaft using balun, insulated monopole and water cooling. The applicators and design

framework presented in this dissertation can also be potentially employed for the treatment of small sized tumors in other organs of the body.

For testing and evaluation of the applicators, we developed computational and experimental platforms using *ex vivo* animal tissues and tissue mimicking phantoms. The characterization of MW applicators using biological tissues is limited by the tissue heterogeneity and variability. Thermo-chromic tissue phantoms with biophysical properties mimicking target tissue properties are useful tools for development, assessment, and thorough characterization of potential ablation devices since the variations in the medium can be controlled and quantified. The parametric models developed for the dielectric properties of fibroids in the course of this dissertation were used to design and characterize polyacrylamide based tissue phantoms. Apart from the dielectric measurements, the thermal properties of the phantom were also recorded using a dual needle sensor. A framework was designed to modify and tune the phantom properties to mimic those of uterine fibroid tissue. Thermochromic phantoms with a gradual change in color from light yellow to dark magenta for a temperature range of 50 ℃ - 75 ℃ were used to characterize the spatial extent of heating profiles. The experimental results in *ex vivo* animal tissues and tissue mimicking phantoms were compared against corresponding simulations using specific absorption rate and thermal ablation profiles to develop a testing platform for MWA candidate devices for fibroid ablation. The methodology presented in this study can be used for MWA of other site-specific thermal treatments.

This contribution is discussed in detail in Chapter 4 and is published in the following article.

- [44] G. Zia, J. Sebek, E. Alvarez, and P. Prakash, "Assessment of thermal damage to myometrium during microwave ablation of uterine fibroids," *42nd Annual International*

Conference of the IEEE Engineering in Medicine Biology Society (EMBC), Jul. 2020, pp. 5263–5266.

1.2.3 Assessment of device positioning and tissue dielectric properties on fibroid ablation outcome

Hysteroscopy approach places constraints on the geometric parameters for advancing the applicator into the fibroids which are located in different anatomical locations inside the uterus. The limited range of insertion parameters that can be achieved with a rigid hysteroscope may present technical limitations with regards to accurate central placement of the applicator for maximum ablation. Ablative approaches are typically designed for an extensive range of fibroid sizes however, less attention has been placed on applicator insertion inaccuracies which may impact outcomes following ablation procedures. In order to assess the effects of device positioning on the ablation outcome, experimentally validated computer models are needed for the transcervical hysteroscopic ablation of fibroids.

Ex vivo bovine muscle is often used as a surrogate tissue for fibroids during the development stages of ablation devices [44], [65]. Due to the limited data available on physical properties of uterine fibroids, it is unclear if bovine muscle is a suitable representative surrogate. Hence, it would be informative to compare the ablation profiles of candidate devices in bovine muscle and uterine fibroids.

Contributions:

Computer models for the transcervical hysteroscopic ablation of fibroids with the 5.8 GHz applicator were developed and validated with the benchtop experimental tools (developed in study 2). Using the computer models, the ablation outcome were evaluated with respect to applicator insertion angles (30°, 45°, 60°), depth and offset from the fibroid center (±2 mm for 3 cm fibroid

and ±1 mm for 1 cm fibroid) with 35 W and 15 W applied power for 3 cm and 1 cm fibroids, respectively. The study demonstrates the technical feasibility of transcervical microwave ablation for fibroid treatment and the relationship between applicator position within the fibroid and fraction of fibroid that can be ablated while limiting thermal dose in adjacent myometrium. This contribution will help clinicians identify the range of insertion angle and applicator tip positions which yield acceptable ablation profiles depending upon the patient anatomy and fibroid size, location and depth inside the uterus wall. Moreover, the methodology developed in this study can be used for other site-specific treatments to investigate the role of device positioning on the outcomes of ablation.

This contribution is discussed in detail in Chapter 5 and is published in the following article.

- [45] G. Zia, J. Sebek, J. Schenck, and P. Prakash, "Transcervical microwave ablation in type 2 uterine fibroids via a hysteroscopic approach: analysis of ablation profiles," *Biomed. Phys. Eng. Express*, vol. 7, no. 4, p. 045014.

The effect of tissue dielectric properties on the fibroid ablation outcomes was also evaluated. The dielectric properties measured for human uterine fibroids in Chapter 3 were used in the validated computational models and the ablation outcomes were compared with the surrogate tissue (*ex vivo* bovine muscle) models. Since human uterine fibroids are not easily accessible, this contribution will help identify the extent of accuracy in using this surrogate tissue during device development.

Chapter 2 - Background

2.1 Introduction

This chapter reviews the state of the art of thermal needle ablation devices and technologies for fibroid treatment, with particular attention on the physics behind the tissue-energy interactions used in the ablation technologies, guidance techniques employed for the placement of device in the fibroid, imaging for monitoring of the treatment outcomes, factors influencing the treatment outcomes and solutions proposed to improve the treatment of fibroids through needle based thermal ablation.

2.2 Needle based thermal ablation technologies for uterine fibroids

2.2.1 Overview of ablation technologies

The most common needle based thermal ablation technologies used for fibroid ablation are laser thermal ablation (LTA), radiofrequency ablation (RFA) and microwave ablation (MWA) which utilize lasers, radiofrequency current, and microwave energy, respectively. Figure 2.1 represents the position of lasers, radio frequency currents and microwaves in the electromagnetic spectrum. Lasers are the most energetic waves out of the 3 electromagnetic waves under consideration. Laser spectrum encompasses ultraviolet (180 nm), visible (400 nm) and infrared
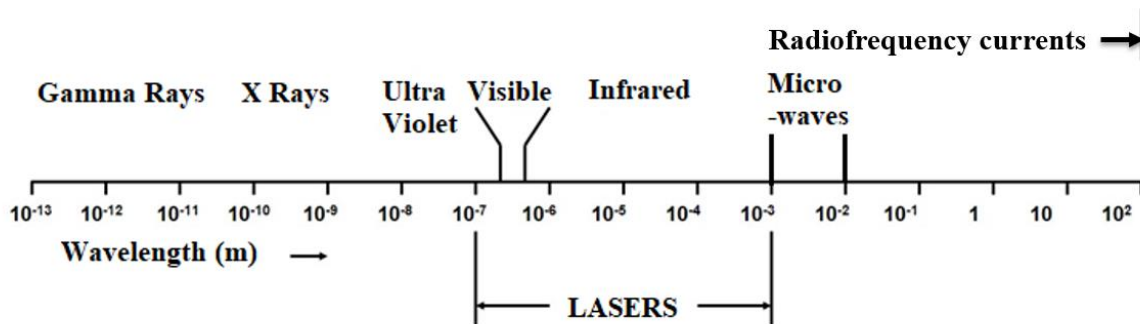
Figure 2.1 Electromagnetic spectrum representing the wavelengths of lasers, microwaves and radio waves.

(700 nm) regions. RFA depends on Joule heating when passing alternating currents typically in the frequency range of ~ 100 kHz - 1 MHz. Microwaves are high energy radio waves in the frequency range of 300 MHz to 300 GHz (i.e. wavelengths = 1 mm - 1 m).

Regardless of the modality used for thermal therapy, the generation of supraphysiological temperatures (>40 °C) inside biological tissues induces changes in the tissue medium at cellular, molecular and structural levels [67].The physiological effects of tissue heating changes with the change in the tissue temperature [47]. Reversible changes like enhancement in metabolic activities of the cells, blood perfusion and oxygenation happen from 40-45°C. Around 50-55 °C), protein denaturation happens. Above 55 °C, coagulative necrosis happens till 100 °C. As biological tissues contain high percentages of water, vaporization occurs from 100-110 °C. Above 120 °C, tissue charring/carbonization takes place. The design and development of fibroid ablation technologies is guided by the clinical goals for the thermal therapy of fibroids i.e. to maximize non-perfused volume inside the fibroids (> 55 °C) for symptom relief while minimizing the damage to surrounding tissues (< 45 °C). It is important to note that the thermal dose accumulated (related to the time-temperature history) inside the target tissue affects the perfusion, electrical, mechanical and thermal characteristics of the target tissue and is responsible for the changes in tissue [67]. Ablation outcomes are often estimated using cumulative equivalent minutes at 43 °C (CEM43) thermal dose [68] which is defined as follows

$$CEM43 = \int_0^t R^{(43-T)} \, dt \ [\text{min}] \tag{2.1}$$

where t = time for which tissue was kept at temperature T, R = compensation factor per °C change in temperature i.e. for $T > 43$ °C, $R = 0.5$ and for $T \leq 43$ °C, $R = 0.25$. The fibroid ablation volume is indicated by 55-60 ºC temperature contour or in terms of 240 CEM43 [69] where the protein denaturation and tissue coagulation occurs. The safety of the surrounding tissues is monitored

using 45 °C contour or 40 CEM43 thermal dose which defines the threshold between reversible

and irreversible thermal effects to the tissue [70] [45].

The heat transfer happening inside the fibroid tissue due to any electromagnetic heat source

can be mathematically approximated by Pennes' bioheat equation which is given by equation 2.2.

$$\rho c \frac{\partial T}{\partial t} = \nabla \cdot k \nabla T + Q_s - m_{bl} c_{bl}(T - T_{bl}) \qquad (2.2)$$

where ρc = volumetric heat capacity [J m^{-3} °C^{-1}], T = temperature [°C], k = thermal conductivity

[W m^{-1} °C^{-1}], Q_s = electromagnetic heat source, m_{bl} = temperature dependent blood perfusion in

tissue, c_{bl} = specific heat capacity of blood. T_{bl} = physiologic temperature of the blood (37 °C)

and t = time (s).

For each ablation technology, the heat source term, 'Q_s', is different which will be

explained for each technology in the following sections.

2.2.2 Device guidance approaches

There are currently three types of device guidance mechanism in use for the needle based thermal ablation of fibroids i.e. laparoscopic, percutaneous and transcervical/transvaginal approach which are discussed in detail in the following section.

2.2.2.1 Laparoscopic approach

As an alternative to hysterectomy or myomectomy [71], laparoscopic ablation can be employed for the treatment of fibroids [72] [73] especially those located at challenging sites inside the uterus. Unlike an open surgery, where different body layers are cut to expose the site of the procedure for tissue extraction, in laparoscopic ablation 2-3 small abdominal incisions are made to provide visual assistance to the surgeon for the placement of ablation device at the desired location inside the fibroid. Following are the main components of the laparoscopic ablation system (shown in Figure 2.2).
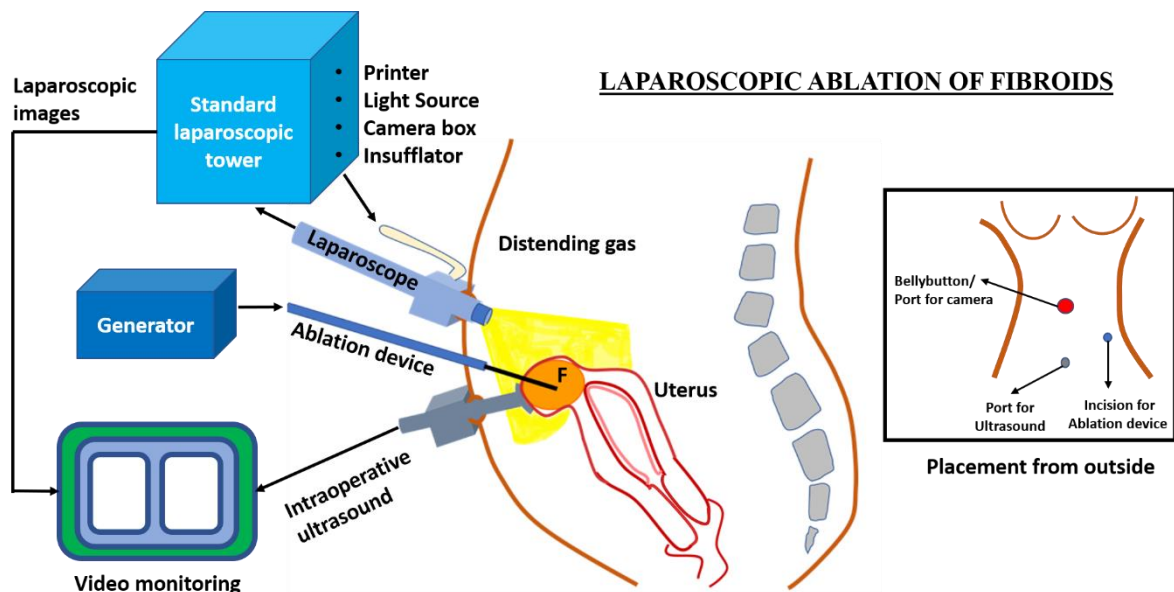
Figure 2.2 Schematic illustration of laparoscopic ablation of fibroids.

A laparoscope (5 or 10 mm, zero degree [72]) is used for direct visualization of the treatment location. A laparoscope is a narrow tube fitted with a 3D video camera which is inserted through a 5 or 10 mm umbilical trocar depending upon the surgeon's standard practice [74] to visualize the treatment site. The system also includes a standard laparoscopic tower consisting of camera box, light source, printer and a surgical insufflator. A surgical insufflator fills CO_2 gas in the abdominal cavity allowing better access to the patient's anatomy and surgical tools.

In a clinical setting for fibroid ablation [75], [76], a laparoscopic ultrasound (Aloka SSD-4000 ultrasound) system is employed with a standard Aloka LUS transducer (UST-5526L-7.5; Hitachi Aloka Medical, Wallingford, CT, USA), which is a rigid, side firing laparoscopic ultrasound transducer with a diameter ≤ 10 mm, and flexible tip for improved scanning and is placed over the uterus via a 10 or 12 mm suprapubic trocar [71],[75][78][79], [80]. The proximity of the transducer to the fibroid allows use of high frequencies (5.0 MHz, 7.5 MHz, and 10.0 MHz) with increased resolution [77], [80]–[83] and permits direct imaging from multiple directions and angles; 1) to map the inside of the uterus, 2) identify the target fibroids for needle device insertion and 3) gauge the depth of insertion of ablation applicator inside the fibroid and 4) ablation monitoring for hyper echogenic changes on the ultrasound images which are produced when the fibroid tissue reaches ablative temperatures (> 60 ℃) due to microbubble generation [41] .

An example needle ablation device inserted percutaneously (through the skin) under laparoscope guidance, is shown in Figure 2.3. Usually, needle diameters for percutaneous insertion are ~ 2 mm [84].
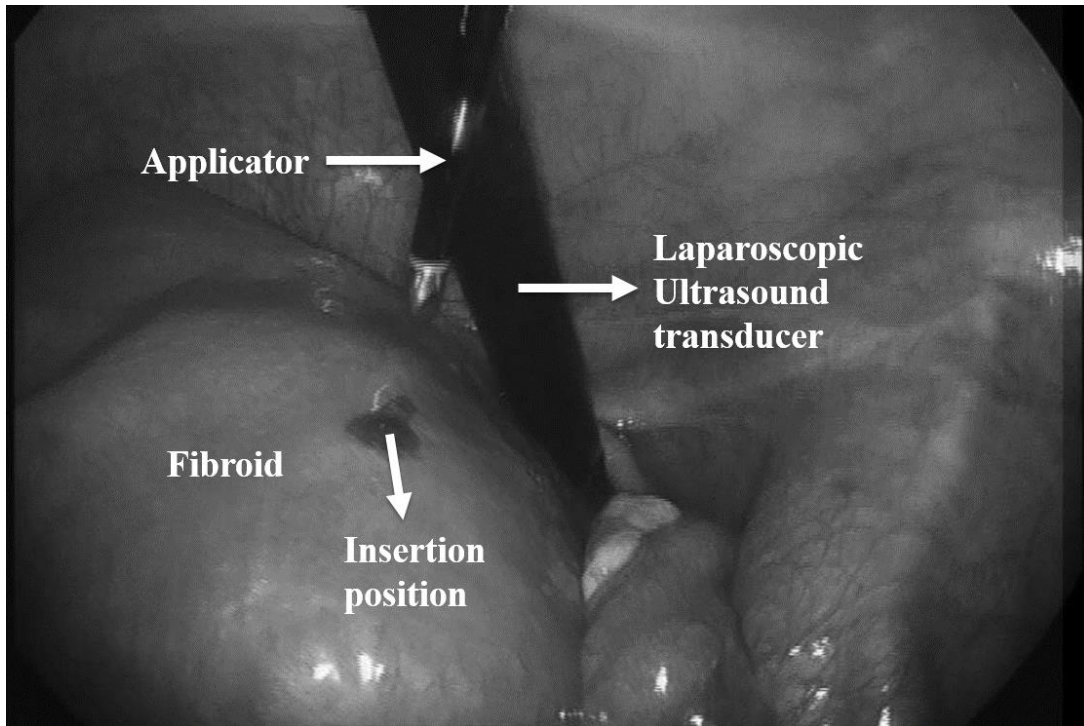
Figure 2.3 Laparoscopic image of needle applicator after radiofrequency ablation. Image is reproduced from Galen et al., *JSLS*, 2014 [20] (open access article with creative common license https://creativecommons.org/licenses/by-nc-nd/3.0/us/. Annotations were added over the image).

Laparoscopic ablation can be performed in an outpatient setting under general anesthesia. In a premarket, prospective, single arm, multicenter (11 international centers) clinical study conducted for laparoscopic RFA of fibroids, Lee et al., [76] reported a mean procedure duration of ~2 ± 1 hours and patient return to daily activities in ~ 3 ± 2 days. In a post market, prospective, single arm, multicenter analysis, Braun et al., [85] reported patient discharge on the day of surgery with mean outpatient hospitalization time ~ 7 ± 3 hours. The safety of the procedure is highly dependent on the skills of the surgeon performing the laparoscopic surgery with the ablation device [72]. Nonetheless, compared to the open surgery, laparoscopic ablation of fibroids offers the benefits of shorter procedure, reduced blood loss, lower re-intervention rates, and lower elective caesarian rates following the procedure.

2.2.2.2 Percutaneous approach

Percutaneous thermal ablation is a method in which a needle based energy applicator is inserted by puncture or minor incision through the skin of the abdomen to reach the fibroid. The percutaneous technique is employed to treat fibroids with less incisions as compared to laparoscopic approach and for the fibroids which are in-accessible or challenging to approach with a vaginal approach [86]. To assist percutaneous puncture, the bowel is displaced away from the puncture site in the abdominal wall [87].

The system comprises of the following components which are shown in the block diagram in Figure 2.4. A percutaneous needle applicator with a diameter typically ≤ 2 mm is normally used to ablate the fibroid [88] and a real time imaging; ultrasonography for RFA [89] and MWA [90] or magnetic resonance imaging (MRI) for laser ablation [87] is employed to help guide and insert the needle applicator inside the fibroid and to monitor the ablation [88].
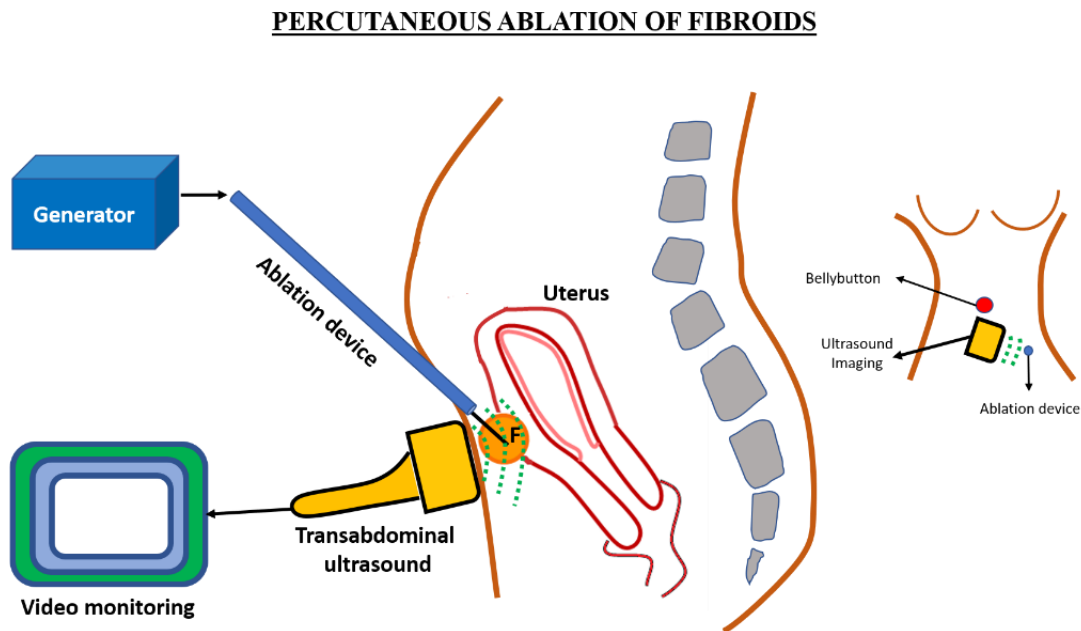
Figure 2.4 Schematic illustration of percutaneous ablation of fibroids

Transabdominal ultrasound probe frequency normally used for fibroid imaging lies between 2.5–4.5 MHz [90]. During real-time ultrasound imaging, the ablation is monitored for hyper echogenic changes in the fibroid as an end point of ablation. Hyper-echoes on the ultrasound images indicate the propagation of heat which resulted in ablative temperatures (> 60 ℃) across the fibroid [41] as illustrated in Figure 2.5.

(a)   **(b)**
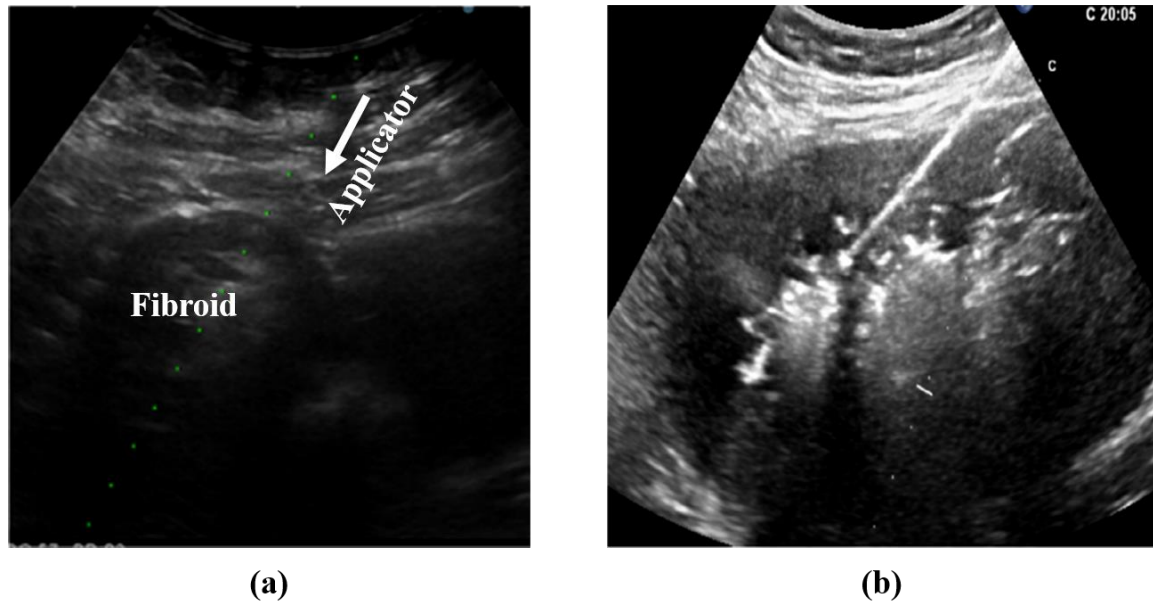
Figure 2.5 Percutaneous ablation of fibroid (a) MWA applicator placed into the fibroid under ultrasound guidance and (b) MWA of fibroid as seen on real-time ultrasound images. Images are reproduced from Ierardi et al., *Seminars in Ultrasound, CT and MRI*, 2021 [46] (with the permission of the journal. Annotations were added over the image).

In a study [87] conducted for percutaneous laser ablation of fibroids using real-time MRI, patients with empty bladder were asked to lie down in supine position in the open MR scanner and a magnetic field was established by placing flexible coil around the lower abdomen of the patient. MR compatible (non-magnetic) needles were placed inside the fibroid using an infrared LED based flashpoint-tracking device (Image Guided Technologies, Boulder, CO). Once the needle was confirmed to be at the right spot, inner trocar was removed and the bare laser fiber was inserted through the outer sheath. The thermal ablation was monitored using real-time image processing

software. The software produces real time maps of thermal ablation using T1-weighted MR imaging signals as illustrated in Figure 2.6. The images were updated every 3.0 seconds.
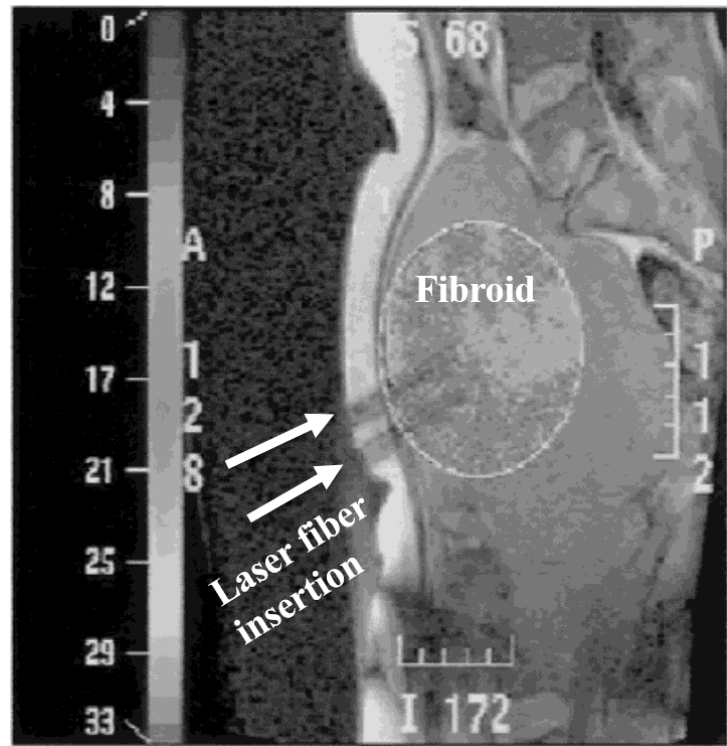
Figure 2.6 Real time monitoring of ablation in percutaneous MR-guided laser ablation. Laser fibers are inserted via MR-compatible needles. Image is reproduced from Law et al., *JMRI,*2000 **[87]** (with the permission of the journal. Annotations were added over the image).

The percutaneous procedure is normally performed in a hospital setting under local anesthesia (injected to numb the insertion site) [91] or intravenous sedation [92] (to alleviate pain and anxiety and reduce patient movement during the treatment). In a study conducted for percutaneous microwave ablation, Zhao et al., [93] reported a median treatment time of ~ 46 min and only one night of hospitalization

2.2.2.3 Transcervical approach

Transcervical ablation approach is considered the least invasive method for intra-uterine treatment of fibroids in which a needle based energy applicator is inserted into the fibroid through the cervical canal. The cervical canal is a natural body passage from vagina to uterus, hence transcervical ablation is incisionless with negligible risk of intrauterine adhesions [29] [40]. The penetration of needle inside the fibroid, real time image guidance and scalable volumetric ablations makes it possible for transcervical ablation to treat the fibroids which are unapproachable or untreatable via hysteroscopic myomectomy [94] [95].

The main components of a transcervical ablation system are 1) needle applicator for fibroid ablation and 2) imaging system as illustrated in Figure 2.7.

TRANSCERVICAL ABLATION OF FIBROIDS
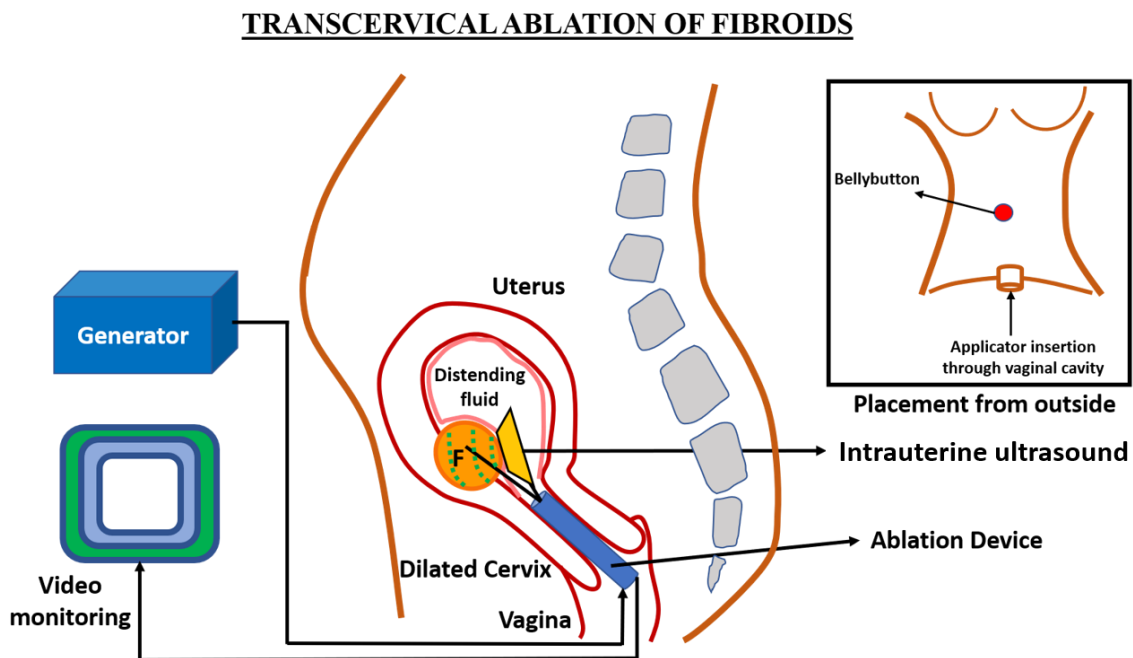
Figure 2.7 Schematic illustration of transcervical ablation of fibroids

23

Intrauterine ultrasound probe is used to provide real time image guidance for needle insertion and monitoring of ablation. Intrauterine ultrasound image provides high resolution images of the uterus and nearby structures (e.g. bowel, bladder). The ultrasound probe image is curvilinear, with s 90° field of view and transmit frequency of 4.8-9 MHz which provides more than 9 cm penetration. Intrauterine ultrasound eliminates the challenges faced in conventional transvaginal sonography as the imaging plane is always directed at a 90° sector to the probe, hence there is only a single imaging plane rather than the sagittal and coronal planes [40].

A hypotonic fluid e.g. sterile water or 1.5 % glycine may be infused into the uterine cavity in small amounts (10-15 mL) through the device for better visualization of uterus walls on ultrasound images [95] [96]. It is to be noted that there are no reported contraindications of uterus injury with the use of such small volumes of distending fluid for acoustic coupling. The external orifice of the cervix which is a centric opening from vagina is normally closed [97]. To insert the device transcervically into the uterus, the cervical dilation may be needed. Depending upon the diameter of the device the cervix may be dilated ~ 8-9 mm either mechanically, osmotically or pharmacologically [95] [98] [99]. The overall diameter and the length of the device is kept within the limits of cervical dilation. Real time ultrasound images with thermal safety borders overlaid on the images (with graphical guidance tools) help the clinician in device insertion and ablation monitoring [95] as illustrated in Figure 2.8.
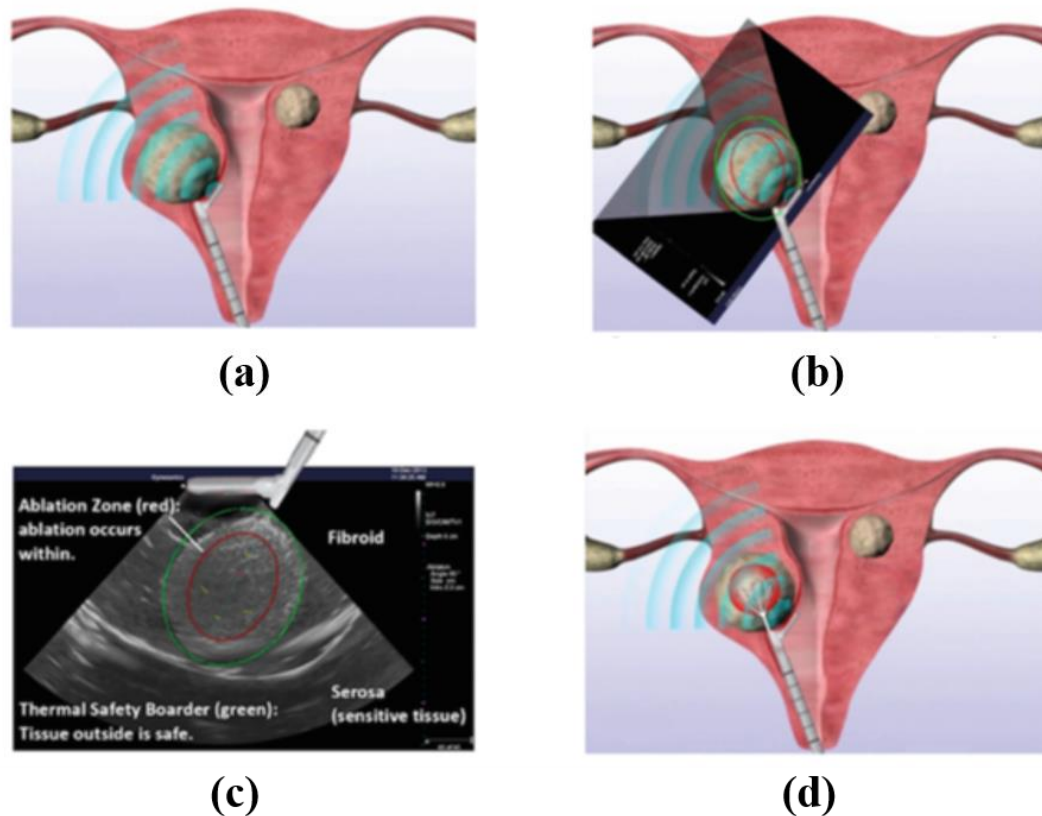
Figure 2.8 Transcervical radiofrequency ablation system for fibroid treatment. (a) Device (introducer) inserted into the fibroid via cervix with IUUS probe guidance, (b) Software projecting ablation boundaries over the graphical ultrasound guidance interface based on electrode tip location and temperature sensor measurements, (c) Projection of ablation and safety contours over the ultrasound image, and (d) Needle electrode deployment to achieve desired ablation sizes according to the predicted ablation contours from the software. Image is reproduced from Toub et al., *Curr Obstet Gynecol Rep*, 2017 [40] (open access article with Creative Commons Attribution 4.0 International License; http://creativecommons.org/licenses/by/4.0/)

The transcervical ablation does not require hospitalization [40] except when it is a clinical necessity based on patient's condition [98]. A general inhalation anesthesia, local anesthesia or conscious sedation may be utilized by the clinician in consultation with the anesthesiologist based on the patient specific procedural requirements [95]. Toub et al. [40] reported that patients return to normal activities in ~ 4 ± 3 days post procedure in a multicenter study conducted for transcervical radiofrequency ablation of fibroids [95], [100].

2.2.3 Laser ablation of fibroids

Laser ablation was the first ablative procedure used for the treatment of fibroids in early 1990s [41], [42]. Laser ablation devices rely on the absorption of laser light in target tissue [103]. The absorption of light in the chromophores (light absorbing components of the tissue i.e. water, hemoglobin and melanin) can generate heat in the tissue [104]. These photo-thermal effects can cause cellular death through coagulative necrosis in the tissue [105] hence forming the basis of laser ablation. The laser source settings (power, energy, and treatment duration), laser light wavelength (near infrared range of the electromagnetic spectrum), applicator's emission characteristics (beam profile, spot size and pulse duration [103]) and tissue's physical (optical and thermal) properties are the main factors contributing to the ablation volumes resulting from laser ablation [106] [107]. The absorption of light can be characterized by the laser wavelength and tissue type [108]. The penetration depth is inversely proportional to the wavelength of laser [109]. Optical penetration of lasers is observed to be more in the tumor cells as compared to healthy tissues typically ~800 nm or ~1064 nm [110]. The proximity of the target tissue from the blood vessels can reduce the ablation size due to blood perfusion effects [111].

The diffusion co-efficient of light, 'D' (mm), inside the tissue [112] can be defined by equation 2.3.

$$D = \frac{1}{3(\mu_a + \mu_s')} = \frac{\mu_a}{\mu_{eff}^2} \tag{2.3}$$

where μ_a = absorption co-efficient (mm-1) and

μ_s' = reduced scattering co-efficient in target tissue (mm-1) which is given by equation 2.4.

$$\mu_s' = \mu_s(1 - g) \tag{2.4}$$

where g is the anisotropy factor accounting for directionally dependent scattering effects. The effective attenuation co-efficient, 'μ_{eff}' (mm^{-1}), can be described by equation 2.5.

26

$$\mu_{eff} = \sqrt{3\mu_a(\mu_a + \mu_s')} \qquad (2.5)$$

The heat distribution inside the fibroid tissue as a result of deposition of laser energy is explained by the Pennes bioheat equation (equation 1) where the laser heat source, 'Q_{laser}' (W mm^{-3}), is a function of time and light fluence rate which is given by the equation 2.6.

$$Q_s = Q_{laser} = \mu_a\Phi \qquad (2.6)$$

Where 'Φ' = light fluence rate (W mm^{-2}) which is a function of radial distance from the source 'r' (mm).

Laser applicator comprises of a laser source and laser fiber tip. The most common laser sources used in fibroid ablation are 1) Neodymium:Yttrium Aluminum Garnet laser (Nd:YAG with 1064 nm [101] [102] [113] [114] and 1068 nm [115] wavelength) and 2) Diode Lasers (with 805 nm [116] and 810 nm [87], [117] [118], [119] wavelength), since optimal penetration of light is achieved in the near-infra red spectrum for tissue ablation [120]. Nd:YAG lasers for fibroid ablation employ ~50-80 W laser power for ~10-50 min based on the guidance technique, size and number of fibroids [101] [102] [113] [114] and in some cases based on the temperature feedback [115] . Laser diodes have similar tissue penetration as Nd:YAG laser however diodes are less costly and more portable [107].

The laser light is delivered using laser fiber which is inserted perpendicular to fibroid and placed within the central region of the fibroid via needles. Flexible bare tip fiber with 300-600 nm diameters are introduced into the tissue via 21 G needles [120] and produce near-spherical ablations of 12-15 mm diameter. Multiple coagulations are made on entire surface of myoma with ~5-7 mm spacing between each coagulation [101] [102] . For a 5 cm fibroid, on an average 50-75 coagulations were performed [113] [114]. Multiple fibers (up to 4 fibers) provides the flexibility of treating tumor sizes >2.5 cm [120] [111] and also targeting multiple small tumors in a single

27

operation. Beam splitters or multi-source devices have been used with multiple fibers for delivering light to each fiber simultaneously [109] [111] for fibroid treatment.

2.2.3.1 Laparoscopic LTA

Laparoscopic laser ablation has been performed with Nd:YAG (1064 nm) laser source and bare tip laser fiber (Sharplan 2100 apparatus, Tel-Aviv, Israel) and 80 W applied power with operating time ranging from 20-45 min for the treatment of large intramural fibroids (3-8 cm diameter) or multiple fibroids. Laser fiber was inserted perpendicular to fibroid and placed at the central part of the fibroid via needles. Multiple coagulations were made on the entire surface of myoma with ~5-7 mm spacing in each coagulation. The mean fibroid volume shrinkage was 41% after 6 months and no regrowth or decrease in volume of fibroid was reported at 12 months. However, the procedure was recommended only for large intramural fibroids which are difficult to treat with myomectomy in patients having no desire for conception because of the potential risks of bowel adhesions and myometrium coagulation [102].

Another group [113] [114] employed the same laparoscopic system as used in the previous study but performed the ablations with gonadotropin-releasing hormone agonist (GnRH-a) therapy 8 weeks before ablation procedure for pre-operative shrinkage of myoma for the treatment of fibroids with pain, pressure and abnormal bleeding symptoms (fibroid size $\leq$ 10 cm). On an average 10 punctures per cm of fibroid were made i.e. for a 5 cm fibroid, 50-75 coagulations were performed with 50-70 W applied power. The operating time for an 8 cm fibroid was ~ 30 min. In this study, 50-70% volume shrinkage was reported beyond GnRH therapy effects with no regrowth of fibroids with patient discharge time ~ 4 h and a recovery time of 1 week. The study recommended laser ablation for patients in menopausal ages who wanted to avoid abdominal myomectomy or hysterectomy.

2.2.3.2 Percutaneous LTA

Percutaneous laser ablation has been performed with Nd:YAG (1068 nm) and bare tip laser fibers placed into the fibroid under MRI guidance via MR compatible 18 G turner needles (Cook, Letchworth, Hertfordshire, UK) for the treatment of symptomatic fibroids (with mean volume 618 cm^3). Laser settings were controlled based on the temperature feedback which was employed for the safety of the surrounding tissues.12 month post ablation imaging data revealed 41% fibroid volume shrinkage with symptom relief and a few patients reported fibroid regrowth [115].

Another group [87], [117] reported percutaneous laser ablation with diode laser (810 nm) and bare tip laser fiber (Diomed, Huntingdon, UK) for large symptomatic fibroids (size range : 22 – 400 cm^3) employing 5 W/ laser fiber and total power output = 25 W/min with mean ablation time = 15 min (range 10–25 min). MR compatible 18 G turner needles (Cook, Letchworth, Hertfordshire, UK) were inserted into the center of the fibroid in a square configuration. Fibers were placed via the outer needle sheath. Sheaths were pulled back by 2 cm to expose the bare fiber tip at the distal end of the needle. The study reported a mean fibroid volume shrinkage of 37.5 % at 3 months post ablation with symptom relief.

Another group [118], [119] employed diode laser source (810 nm with fiber splitter and multiple fibers) for the treatment of large fibroids with 600 µm or 1000 µm quartz bare tip laser fiber. Using 25 W applied power and treatment time depending upon the size of the fibroid with 1 min/coagulation position with each coagulation position 2 cm apart from each other for partial ablation of fibroids, 75% volume shrinkage was achieved after 3 months.

.

2.2.3.3 Transcervical LTA

Transcervical hysteroscopic laser ablation has been performed with Nd:YAG (1064 nm) laser source and bare tip laser fiber (Sharplan 2100 apparatus, Tel-Aviv, Israel) and 80 W applied power, operating time ranging from 10-50 min for the treatment of large submucosal fibroids (1.6 $\pm$ 1.0 cm^3 to 15.4 $\pm$ 7.6 cm^3) [101] and with GnRH-a pretreatment. For type 1 fibroids, laser fiber was inserted perpendicular to fibroid and placed at the centrally inside the fibroid while for type 2 fibroids, laser fiber is perpendicularly inserted 5-10 mm inside the intramural portion of fibroid (based on the depth of the portion). Multiple coagulations were performed on the surface of myoma in Type 1 fibroids or the remaining intramural portion of Type 2 fibroids (after hysteroscopic myomectomy) with ~5-7 mm spacing in each coagulation. Less postoperative blood loss and adhesion formation was reported with GnRH-a therapy. A 38% mean fibroid volume reduction was reported (independent of GnRH-a therapy effects) with symptom relief and no regrowth of fibroid. For patients with infertility issues due to fibroids, 67% patients who attempted for pregnancy conceived within 8 months post treatment [101].

2.2.4 Radiofrequency ablation of fibroids

Radiofrequency ablation (RFA) is the most established technology for the treatment of fibroids out of the three technologies under consideration [121], [122] and provides a volume reduction of fibroid (~70 %) at 6 months [123] . RFA needle applicators can create ~ 5 cm spherical ablative zones within the uterine fibroids with an affordable cost and mean treatment time of 20 min [86], hence superseding the performance of laser ablation devices used for fibroid treatment [84], [121]. A typical RFA system comprises of an RF generator, applicator and interconnecting coaxial cables. RFA applicators employ the principal of electrical resistive heating in the target tissue. The electric current of ~450–500 kHz causes the ions (Na^+, K^+, Cl^-) inside the tissue medium to oscillate rapidly resulting in resistive tissue heating around the active electrode [124]. Necrosis and coagulation happens as soon as the temperature in the tissue reaches the ~55-60 ºC. In monopolar RFA, an RF current is applied through the active electrode (usually multiple adjustable needle arrays based on the size of fibroid) placed in the target tissue whereas the ground pad acting as a return electrode for the current is placed on the patient's skin (at back or thighs). In bipolar RFA, the RF current flows between two electrodes placed inside the tumor [114]. RF systems are typically monopolar and employ temperature or impedance feedback control [72].

The thermal energy generated by the applicator and deposited locally to tissue medium is described in terms of specific absorption rate, 'SAR', which is measured in [W kg^{-1}] and is given by equation 2.7.

$$\text{SAR} = \frac{J^2}{\sigma\,\rho} \qquad\qquad (2.7)$$

Where 'σ ' is the electrical conductivity of the tissue, 'ρ' is the tissue mass density and '**J**' is the electric current density which is a function of electric field strength, '**E**' [V m^{-1}], and electrical conductivity of the tissue, 'σ ' [S m^{-1}] and is given by equation 2.8.

$$\mathbf{J} = \sigma\,\mathbf{E} \tag{2.8}$$

The current density or the electric field strength cause direct heating only in the close vicinity of the electrode, thermal conduction is responsible for propagating the heat at distances away from the electrode [125]. The heat distribution inside the fibroid during RFA is explained by the Pennes bioheat equation (equation 1) where the RF heat source, 'Q_{rf}' (W mm^{-3}), is given by the equation 2.9.

$$Q_s = Q_{rf} = \sigma\,\mathbf{E}^2 \tag{2.9}$$

Hence, the main factors governing the volume of ablation during RFA, apart from the heat losses due to blood perfusion [124], are the tissue temperature, electric field strength around the active electrode and tissue's physical properties (electrical [124] and thermal [126]).

2.2.4.1 Laparoscopic RFA

Initial bipolar diathermy systems for the fibroid coagulation utilized 1.5 cm needles for small fibroid ablations [114]. Later, a new bipolar RFA system was developed using heavy gauge steel needles (Reznik Instrument Company, Skokie, IL and J.E.M. Davis, Hicksville,NY) as electrodes which were supplied a continuous power of 70-120 W from RF generator to ablate fibroids [114], [127]. A 5 cm needle electrode in a 30 cm instrument or a 45 cm needle electrode were used in these systems which could be passed through the operative laparoscope or 5 mm suprapubic trocar. The needles allowed penetration at 90º angle to the uterus. ~3-5 mm coagulation around the electrode was achieved. On an average, 30-50 passes of needles were used in each fibroid. Up to 7 cm fibroid could be treated with these systems within ~20-30 min with minimal risk of postoperative adhesions [114], [127].

The first monopolar RFA system was reported in [128]. In majority of the commercial and clinical RFA systems, the RF needle is inserted percutaneously (2 mm skin incision) using

ultrasound guidance with simultaneous laparoscopic visual assistance [72], therefore the terms: "Percutaneous-Laparoscopic" or "Laparoscopic-Ultrasound guided" are often used interchangeably in literature for laparoscopic RFA approaches [46].

The most widely used laparoscopic ablation technology for fibroids Acessa™ system (Halt Medical, Inc., Brentwood, CA) [20], [74] which has been approved by US Food & Drug Administration (FDA) for inpatient/outpatient treatment of fibroids [73], [129]. The system (illustrated in Figure 2.9) consists of a dual-function monopolar RF generator and a disposable RF applicator hand-piece consisting of 3.4-mm diameter primary needle with multiple deployable active electrodes (7 electrodes needle array) and two dispersive ground electrodes [20] to provide a return path to the current. The primary needle is inserted into the fibroid through a puncture in uterine serosa under simultaneous laparoscopic and ultrasound guidance to confirm the device tip position inside fibroid. The active electrodes are deployed inside the fibroid with electrode tips having thermocouple for continuous monitoring of temperature. Appropriate deployment of electrode array results in maximum volumes of ablation achieved inside the fibroid. Small 1.5 cm diameter fibroids do not need electrode array deployment for ablation. For 2- 3.5 cm spherical fibroids the primary needle of the RFA is centrally placed inside the fibroid. For fibroids ≥ 4 cm in diameter, the main aim is to ablate the periphery of the fibroid as compared to the center hence multiple eccentric ablations are performed [72].

The applicator delivers a low-voltage, high-frequency (450–500 kHz) [72] alternating current into the fibroid with a maximum output power of 200 W [20]. The current density is concentrated in the pelvic region with the currents typically ranging ~ 1- 2.5 A [20] and hence do not impact the cardiac activity of the patient. The tissue temperature is maintained at 100 ºC for the ablation duration which is calculated using the treatment algorithm and depends upon the fibroid volume [20].
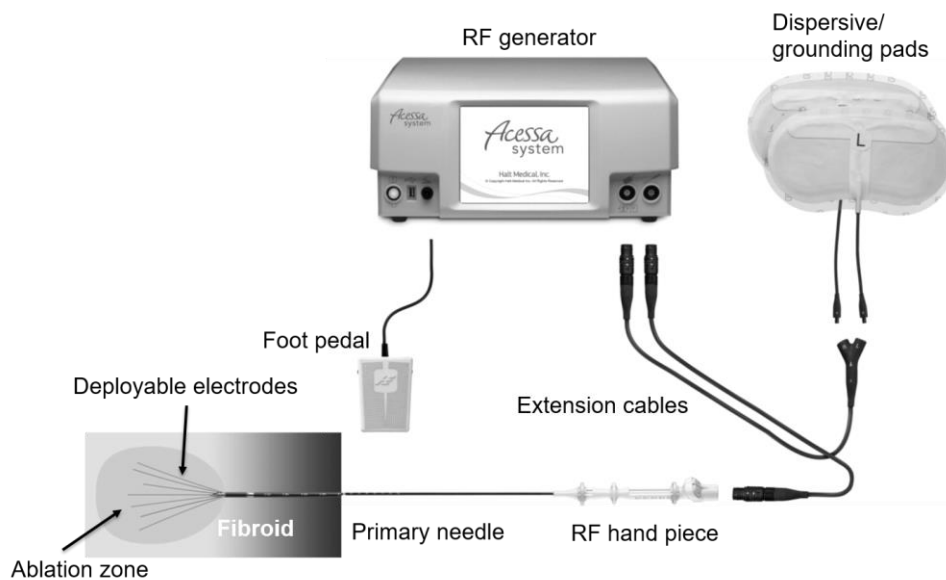
Figure 2.9 Laparoscopic radiofrequency ablation system for fibroid treatment. Image reproduced from [20].

The mean volume reduction achieved as a result of fibroid ablation in this system is ~ 45% [77], [123]. Although there are no uterine incisions and suturing of myometrium, however a 3.4 mm puncture is made in the myometrium for needle placement inside the fibroid and coagulation of needle tract inside the myometrium is performed during withdrawal of the probe by applying intermittent low power (8-15 W) coagulation to the primary needle tip [20].

2.2.4.2 Percutaneous RFA

In a study [86] conducted for percutaneous RFA, the fibroid was punctured under abdominal ultrasound guidance. Before ablation, the same puncture was used to perform a biopsy (for tissue pathology) with 18 G BioPince® needle (Angiotech, Vancouver, British Columbia, Canada) inserted through the RF primary needle. A 35-40 mm long umbrella-shaped needle electrode system (LeVeenCoAccess, RF3000 system, Boston, USA) was used to perform multiple RFA depending on the size of the fibroid. The extent of necrosis was confirmed through an immediate postoperative contrast enhanced ultrasound imaging. To prevent bleeding, ablation tract was coagulated with 10 W power at the end of the procedure. More than 50 % fibroid volume reduction with symptom relief was observed at 6 month post ablation using this procedure [86].

2.2.4.3 Transcervical RFA

The FDA approved transcervical RFA, The SONATA® system (Gynesonics, Redwood City, CA) consists of an intrauterine ultrasound (IUUS) probe and a RFA hand-piece (introducer and needle electrode array) whose combined diameter is 8.3 mm (compatible with 27 French cervical dilation) [40].A single ablation with SONATA system can treat fibroids with a diameter of 1-5 cm (i.e. up to a volume of 42 cm^3). For larger fibroids (> 5 cm), multiple ablations are employed [4]. Maximum ablation sizes of 4 cm width and 5 cm length can be created. Depending on the chosen ablation size, the RF energy with applied powers ≤150 W is delivered for 2–7 min after the tissue temperature reaches 105 ºC [40]. Figure 2.8 explains the procedure of transcervical radiofrequency ablation of fibroids as described in [40].

The studies [4], [40], [100] reported a volume reduction of ~67-68% in fibroids is achieved at 12 months post treatment. With symptom relief and low re-intervention rates (0-3.7% [4]), patients return to normal activities within a median of 4 days (mean 4.4 ± 3.1 days) [40].

Moreover, there are no reported complications (related to pregnancy and childbirth) after the treatment [130]. The clinical studies conducted for RFA ablation for fibroids have been thoroughly reviewed in [72], [122], [123].

2.2.5 Microwave ablation of fibroids

Microwave ablation (MWA) is the most recent technology for the thermal ablation of fibroids. MWA offers several benefits over other needle based ablation technologies for fibroids like larger ablation volumes, shorter treatment durations, are less prone to local blood perfusion and heat sinks and can support multiple applicators and there is no need of grounding pads [131]. MWA ablation can produce temperatures as high as 170 ^{o}C within 5 min of tissue heating [37]. The basic components of MWA are similar to RFA systems i.e. MW generator, power distributor and MW applicator. The most common MWA frequency used for fibroid treatment is 2.45 GHz [46]. The applicators consist of a feedline transmission cable (most commonly coaxial cable) with the distal tip modified to create an antenna that radiates microwave power to the surrounding tissue [132]. Power attenuation along the feedline cable leads to heating of the cable, which may cause heating of adjacent tissues and breakdown in structural integrity of the cable. In most ablation applicators, to enable high power use, these issues are mitigated by employing active cooling strategies (e.g. water or gas cooling) [133].

The MWA works on the principle of dielectric hysteresis. When the MWA applicator is placed inside the fibroid tissue and powered on, the heat is generated due to the rapid oscillations of polar molecules (water) in the tissue. The continuous realignment of the polar molecules in the presence of an applied electromagnetic field with alterations in polarity billions of times/second produces frictional heating and subsequently ablative temperatures in the tissue medium which results in tissue coagulation [131], [134].

The thermal and dielectric properties of the target tissue significantly impact the thermal ablation profile during MWA ablation [134]. The dielectric properties are known to be functions of frequency, temperature, composition of tissues and other biological factors [134] [59], [135] [63]. The transmission of microwaves is governed by the complex permittivity of the tissue, 'ε^{*}' which is given by equation 2.10.

$$\varepsilon^{*} = \varepsilon_{r} - j\,\varepsilon^{"} \qquad (2.10)$$

The relative permittivity, 'ε_r' of the tissue, is responsible for the energy propagation inside the tissue. The effective conductivity, 'σ_{eff}', derived from the imaginary part '$\varepsilon^{"}$' in equation 2.10, is responsible for microwave energy absorption inside the material, and defined in equation 2.11.

$$\sigma_{eff} = \omega\varepsilon_{o}\varepsilon^{"} \qquad (2.11)$$

where $\omega = 2\pi f$, f = frequency and $\varepsilon_o = 8.85 \times 10^{-12}\,F\,m^{-1}$.

The heat distribution inside the fibroid during MWA is explained by the Pennes bioheat equation (equation 1) where the MWA heat source, 'Q_{mw}' (W mm^{-3}), is given by the equation 2.12.

$$Q_{s} = Q_{mw} = \sigma_{eff}E^{2} \qquad (2.12)$$

where 'E' [V m^{-1}] is the electric field strength.

2.2.5.1 Percutaneous MWA

Percutaneous approach is the most widely used microwave ablation treatment of fibroids [41], [46], [53], [91], [93], [136]–[139]. During percutaneous MWA, a microwave antenna and thermocouple needle are inserted into the fibroid under conscious sedation under ultrasound guidance [41]. Majority of the studies conducted for percutaneous MWA [41], [53], [93], [136]–[138] employed KV2000 or KV2100 MWA tumor treatment device (Kangyou Medical instruments Nanjing, China) in continuous or pulsed mode emission with powers ~ 50-100 W for

the treatment of ~3-8 cm diameter fibroids at 2.45 GHz frequency and applicator diameter ~ 13.5-16 G. One study [9] used an 18 cm long MWA applicator with 11 mm long radiating element and 1 mm long emission aperture with internal water cooling to lower the temperature of the applicator shaft. Another study [91] used 28 mm applicator radiating length and to prevent thermal damage to surrounding tissues a room temperature saline was continuously infused at 60 ml/min along the proximal part of the applicator. The ablation duration varied between ~3-10 min depending upon the size of the fibroid [41], [91], [136]. Single MWA applicator was used for treating <5 cm fibroids where as two applicators were used for > 5 cm fibroids [41], [93], [137]. The maximum myoma reduction rate achieved in percutaneous MWA was ~ 90 - 93% at 12 months [41], [53].

2.2.5.2 Transcervical MWA

Transcervical MWA has been used for the treatment of fibroids in combination with the microwave endometrial ablation [54] at 2.45 GHz using microwave generator; Microtaze AZM 550, Alfresa-Pharma, Osaka, Japan. After the endometrial ablation, a 4 mm diameter applicator with a conical tip was inserted into the submucosal fibroid with the help of a straight guiding tube (4.2 mm inner diameter and 5.1 mm outer diameter) which was fixed over the surface of myoma. Single submucosal fibroids of 4–7 cm size (5.5 ± 2.1 cm) were treated in 35 patients with an applied power of 40 W at multiple ablation sites for 150–1300 s and overall surgery time ~ 30-40 min. The volume reduction at 6 months post operation was ~74 % [57].

Recent *ex vivo* tissue studies suggest the feasibility of transcervical MWA for fibroid treatment via hysteroscopy with ablation systems at 2.45 GHz [44] and 5.8 GHz [45]. The system comprised of a microwave generator (GMS200WS, Sairem [44] or HP 83572A synthesized sweeper [45]), Solid state power amplifier [45], coaxial cables, a wideband radiofrequency power meter (Bird Technologies 7022) for monitoring of power, water circulation pump (Masterflex L/S

economy drive model 7015-20) for applicator cooling and water-cooled omnidirectional monopole MWA applicator with an outer diameter = 2.15 mm (conforming to the size of hysteroscope's working channel (~3 mm)). The 5.8 GHz applicator was custom-designed to produce focal ablations for smaller fibroids (~ 1-3 cm) and the use of balun restricted the backward heating along the applicator shaft. The study reveals that the insertion parameters of MWA applicator inside the fibroid impact the ablation outcomes drastically. With insertion angles (30°, 45°, 60°), depth and offset from the fibroid center (±2 mm for 3 cm fibroid and ±1 mm for 1 cm fibroid), the ablation volumes in 3 cm fibroid ranged ~35-84% when heated with 35 W for 140-400 s and in 1 cm fibroid ranged ~34-68% when heated with 15W for 30-50 s and zero damage to the surrounding tissues ($\leq$ 40 CEM43). A maximum ablation volume of ~90 % can be achieved if thermal dose > 40 CEM43 is acceptable in the myometrium [45].

2.3 Discussion

Before selecting the guidance approach for needle based thermal ablation of fibroids, it is important to assess the size, volume, location and number of fibroids in the uterus through imaging prior to the ablation procedure. There are several imaging modalities that may be suitable for this purpose i.e. hysteroscopy (via hysteroscope thin lighted tube inserted transvaginally for direct examination of uterus), ultrasound (transvaginally or transabdominally) and magnetic resonance imaging (MRI) [53], [92], [3], [84].

Laparoscopic guidance provides an easier approach to fibroids as compared to other minimally invasive techniques for fibroid ablation. The level of surgical intervention has been significantly reduced in the laparoscopic ablation as compared to the traditional laparoscopic hysterectomy or laparoscopic myomectomy. Laparoscopic guidance is more invasive than the other guidance techniques used for ablation. General anesthesia is required with multiple incisions in the abdomen i.e. one incision for a 5-mm laparoscope, another 10–12-mm incision for the laparoscopic ultrasound transducer, and 3-4 more incisions (2 mm) for the percutaneous placement of the needle electrode. This guidance approach is prone to adhesions, infections in the peritoneal cavity and damage to the surrounding organs of uterus. In percutaneous approach, the number of incisions has been reduced as compared to laparoscopic approach by incorporating high resolution transabdominal imaging. Moreover, no preconditioning of cervix or abdomen is required in a percutaneous approach as compared to other techniques which prevents issues such as fluid overloading, gas embolism, or local anesthetics reaching systemic circulation [53].However, even in the percutaneous approach there are risks of abdominal perforations and bowel puncture which are managed by adjusting nearby organs to bring the anterior wall of fibroid closer to the abdominal wall to ensure accurate needle position for puncturing inside the fibroid. [53], [140]. The

incisionless transcervical approach for fibroid ablation reduces the chances of many potential complications of other approaches. In transcervical approach, since the fibroid is not approached through the peritoneal cavity, there are no chances of intraperitoneal adhesiogenesis. Moreover, there are minimal chances of uterine rupture since there is no penetration into uterine serosa [95].

The objective of uterine fibroid ablations is to ablate the fibroid as much as possible while protecting the functional layer endometrium and the supporting muscular layer myometrium (as discussed in Chapter 1). In laparoscopic as well as percutaneous approach the applicator is introduced from the outer wall of the uterus (serosa) hence there are limited chances of damaging the endometrium. Therefore, a laparoscopic and percutaneous approach may be considered when the fibroid location closer to the serosal surface as compared to the endometrial cavity. The transcervical approach is the least invasive guidance approach since the body's natural cavity (cervical canal) is used for the introduction of applicator into the uterine cavity. However, since the transcervical applicator is introduced into the uterus from endometrial cavity there are more chances of damaging the endometrium as compared to other approaches. The transcervical ablation may be a viable option for the treatment of submucosal fibroids which are closer to the uterine cavity. However, there are limited approach angles in transcervical approach due to the anatomy of the uterus hence applicator may not be able to reach challenging sites inside the uterus for which laparoscopic or percutaneously techniques may be considered.

Microwave ablations could provide larger ablation zones (up to 6 cm diameter) with a single antenna insertion [46] since microwave ablations are faster and the peak temperatures achieved in microwave ablation are higher (up to 170 $^\circ$C [134]) than the radiofrequency and laser ablations which are prone to tissue charring. Moreover, microwaves have better performance near blood vessels, are less sensitive to tissue types and there is no need of grounding pads as opposed

to RFA [139]. However, microwave ablation is a relatively new technology in fibroid ablation as compared to other ablation technologies. Moreover, microwave antennas have more intricate designs as compared to radiofrequency electrodes. Radiofrequency ablation is the most established and advanced technology for the treatment of fibroids because it is simpler and cheaper than the laser ablation. The laser applicators used so far for fibroid ablation provided smaller ablation zones in a single insertion [113] [114] as compared to other ablation technologies due to carbonization and charring. Use of cylindrical diffuser, cooling and pulsed mode operation in laser ablations [110] [107] could enhance the size of ablation in laser technology used for fibroids.

2.4 Conclusion

Since fibroid is a highly heterogeneous tissue in terms of size, location, composition, shape, symptoms with patient variability factors (e.g. age, race, family history, reproductive state, underlying diseases), there cannot be one to one comparison of different technologies or guidance approaches on the basis of clinical outcomes reported in the studies. The choice of guidance approach depends upon the size, location, number of fibroids and patient condition. Every guidance approach has its own merits and demerits. With regards to the technology, radiofrequency ablation has been the most widely used technology for the fibroid ablation, hence this technology is more advanced as compared to other technologies. The technological advancements in laser ablation for other tumor ablations [107], [120] could be employed for fibroid ablations. Microwave ablation of fibroids shows promising results [46], [141] and it has a potential to improve the size and shape of ablations with larger ablation volumes achieved in shorter duration of time as compared to other needle based ablation technologies.

Chapter 3 - Dielectric Properties of *Ex vivo* Human Uterine Fibroids[1]

3.1 Introduction

Uterine fibroids are the most common benign muscular tumors of the uterus with a lifetime prevalence of ~70-80% in pre-menopausal women [5], [6] [7]. Fibroids can considerably impact the quality of life with symptoms including abnormal uterine bleeding, dysmenorrhea, chronic pains, increased bladder frequency, painful intercourse and causes miscarriages and infertility in severe cases [11] [12]. Around 30% of the patients experience symptomatic fibroids [7] which are the leading indication for hysterectomy. Fibroids are classified based on their location within the uterus, and can range in size from a few millimeters to several centimeters [16], [142], [143]. Thermal ablations of fibroids using non-ionizing electromagnetic energy have the potential to provide a minimally invasive therapeutic option for patients desiring uterus preservation. Thermal ablation modalities such as lasers [113], [144], [145], and more recently, high intensity focused ultrasound (HIFU) [146] and radiofrequency ablation (RFA) [122] (via laparoscopy [20] [75] and transcervical approaches [37] [40]) have been widely explored for fibroid treatment. Microwave ablation (MWA) is another thermal ablation modality which is in clinical use for treatment of tumors in the liver, lung and kidney [47], and offers the potential for ablation of large tissue volumes in relatively short duration. There has been a growing research interest in using MWA via percutaneous [10] [11] and transcervical [49]–[52][44], [45] approaches for the treatment of fibroids.

---

[1] This chapter has been accepted for journal publication as G.Zia, J.Sebek, P. Prakash, "Temperature-dependent dielectric properties of human uterine fibroids over microwave frequencies", Biomedical Physics & Engineering Express, Sep 2021, doi: https://iopscience.iop.org/article/10.1088/2057-1976/ac27c2.

During MWA, an applicator is positioned within or adjacent to the target tissue and radiated microwave power is absorbed within tissue with appreciable attenuation. The goal of thermal ablations of fibroids is to maximally ablate the fibroid volume while protecting the surrounding healthy tissues from thermal damage [45], ultimately resulting in shrinkage of the fibroid providing symptom relief to the patients [43], [147] . Tissue temperatures during microwave ablation typically exceed 100 ºC, and have been reported up to ~170 ºC [37], with temperature in regions at the periphery of the ablation zone typically in the range ~50-60 ºC.

Tissue dielectric properties have a significant impact on the thermal ablation profile during MWA. The complex permittivity, ε^*, of the biological tissue determines the transmission of microwaves inside the tissue medium and is given by equation 3.1.

$$\varepsilon^* = \varepsilon_r - j\,\varepsilon^{''} \qquad (3.1)$$

The real part of ε^* called the relative permittivity, ε_r, determines the propagation of energy through the tissue based on the wavelength of the applied electric field at a specific frequency. The effective conductivity, σ_{eff}, is calculated from the imaginary part of dielectric permittivity, $\varepsilon^{''}$,using equation 3.2. σ_{eff} determines the absorption of microwave energy inside the material. Tissues with high water content have high σ_{eff} values and hence exhibit higher absorption of microwaves with respect to tissues containing low water content and lower σ_{eff} values

$$\sigma_{eff} = \omega\varepsilon_o\varepsilon^{''} \qquad (3.2)$$

where angular frequency, $\omega = 2\pi\,f$, f = frequency

and permittivity of free space, $\varepsilon_o = 8.85 \times 10^{-12}\,F\,m^{-1}$.

Furthermore, the dielectric properties of tissue are known to be functions of frequency, temperature, composition of tissues and other biological factors [134] [59], [135] [63]. Tissue temperatures during microwave ablation typically exceed 100 ºC, and have been reported up to

45

~170 ºC [37], with temperature in regions at the periphery of the ablation zone typically in the range ~50-60 ºC. Fibroid tissues are well known for their heterogeneous tissue structure and composition with different proportions of extra-cellular matrix (i.e. collagen, proteoglycans and fibronectin) [5], [13], [148], [149]. Moreover, the variation in fibroid tissues properties also comes from degenerations (e.g. hyaline, cystic, myxoid or red degeneration [150]) occurring inside the fibroid tissues. For the effective design of therapeutic instrumentation for treatment of uterine fibroids, there is a need to characterize dielectric properties considering the aforementioned factors.

The dielectric properties have been characterized for various normal/pathologic human and animal tissue at various frequencies and temperatures [59]–[61]. Public databases [151] collating the measured dielectric properties of various tissue types are highly informative to engineers developing electromagnetic instrumentation for therapeutic applications. Electrical conductivity at 460 kHz (the frequency typically employed for RF ablation) of uterine fibroids in human patients *in vivo* has previously been at physiologic temperature [152]. However, there are limited published data for dielectric properties of uterine fibroids in the microwave frequency range. Since fibroids are not common in animals, measurement of physical properties of fibroids are often restricted to measurements on samples obtained from hysterectomy procedures in human patients. Bovine muscle is often used as a surrogate tissue for uterine fibroids during the design and evaluation of candidate technologies [44], [65]; temperature dependent dielectric properties of bovine muscle tissue have been reported [40].

Computer models and simulations with biophysical properties mimicking the tissue properties are powerful tools for development, evaluation, and characterization of candidate MWA devices [153]. Measurement of frequency dependent dielectric properties over ablative

temperature ranges is essential for careful design and evaluation of microwave technologies for ablation of uterine fibroids. The aim of this study was to: 1) experimentally measure the changes in broadband (0.5- 6 GHz) dielectric properties of *ex vivo* uterine fibroids excised during hysterectomies in human patients over the ablative temperature range (i.e. 23 ℃ – 150 ℃) and 2) present coefficients for parametric models characterizing the temperature and frequency dependent dielectric properties of fibroids for use in computational models of microwave tissue heating.

3.2 Methods

3.2.1 Collection of tissue samples

Uterine fibroid tissue samples were obtained from West Virginia University tissue bank. The specimens were excised from human patients receiving standard of care hysterectomy treatment, under an approved institutional review board (IRB) protocol for collection of human blood and tissue for research purposes. The indications for hysterectomy in all the patients included enlarged uterus due to multiple fibroids, heavy bleeding and chronic pain.

Samples of the freshly excised fibroids were preserved in RPMI growth medium, stored in sealed biohazard bags and shipped to our laboratory while placed in an insulating container with ice packs. The tissues kept inside the RPMI gauze were taken out of the icepacks to raise the initial temperature to room temperature. To minimize dehydration, tissue samples were maintained within RPMI gauze after sectioning and only removed immediately prior to dielectric property measurements. All measurements were conducted within 24-36 h post excision.

For fibroids with maximum dimensions < 2 cm, a single dielectric property measurement was performed on each sample; for fibroids with a maximum dimension exceeding 2 cm, we took multiple measurements by first sectioning the fibroids into samples approximately ~1.5-2 cm in diameter.

3.2.2 Measurement of dielectric properties

The dielectric measurements were performed in a certified BSL-2 lab environment inside a fume hood using the open ended coaxial probe method [154], [155]. The dielectric properties of the tissue were estimated by a software inversion of broadband reflection coefficients of the open-ended coaxial probe (Keysight 85070 E dielectric probe kit) as measured by Keysight N9923A FieldFox Handheld RF vector network analyser (VNA). The sensing resolution of the dielectric probe is within a 5 mm radius around the probe tip [135]. We compared the dielectric properties of standard liquids (methanol and ethanol) in our measurement setup with the theoretical values presented in [156]. At 20 ℃, the maximum error in real and imaginary parts of complex permittivity for methanol was < 7% and for ethanol was < 10%, respectively. These error levels lie well within the range of the errors recorded in similar studies; for a frequency range of 0.5-20 GHz, the maximum error for methanol ≤ 8 % and for ethanol ~ 12% [157] [158], [159].

The dielectric probe was placed such that its tip was in contact with the tissue sample to capture the dielectric data over 401 linearly spaced points spanning the frequency range of 0.5 GHz to 6 GHz and temperatures from 23 ℃ to 150 ℃. This temperature range was chosen such that it covers the ablative range of temperatures commonly observed in target tissues [160]. Temperature of tissue in contact with the dielectric probe was measured using a Qualitrol OptiLinkTM fiber optic temperature sensor. The overall measurement setup is depicted in Figure 3.1(a). The temperature sensor was placed 2 mm away from the dielectric probe tip to preclude interference with electromagnetic field of the probe [63] as shown in Figure 3.1(b). A polyimide sheath was slid over the fiber optic sensor for its protection and a rubber band was used to fix the sensor at an appropriate position over the dielectric probe.

The fibroid sample was taken out from the RPMI gauze and placed in a custom-designed sample holder shown in Figure 3.1(c). The sample holder was constructed from copper sheets with the objective of minimizing thermal gradients across the sample, similar to prior studies [63], [135]. First, the dielectric properties were recorded at room temperature (23 ℃). Then, to capture the temperature dependency of the dielectric data, the sample was heated using a ThermoScientific
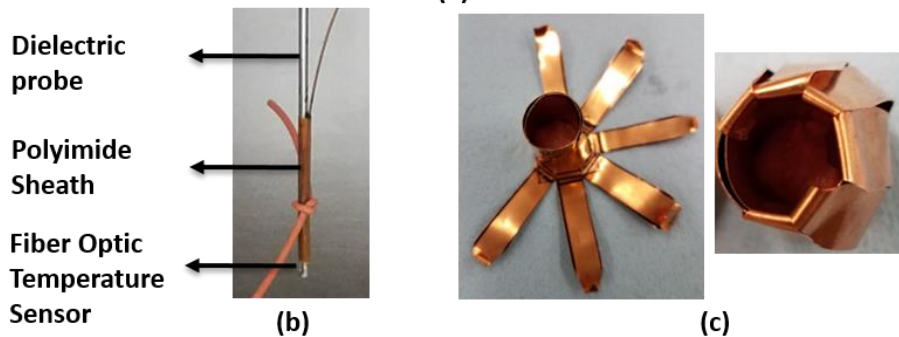
Figure 3.1 a) Experimental setup for dielectric measurements of ex-vivo human fibroid. Tissue sample is placed on the hot plate inside the fume hood and measured with dielectric probe connected to VNA. Tissue temperature is monitored by fiber optic sensor and data collection hub. Both VNA and data hub are connected to laptop b) A method for fixation of temperature sensor 2 mm above the tip of open ended coaxial probe. c) Custom-designed copper template for holding and heating the tissue at elevated temperatures.

hot plate [63]. The initial temperature of hot plate was set at ~150-200 ℃ to achieve similar heating rates as that of water cooled MWA applicators (at a point 10 mm away from the applicator surface) [63]. However, as the sample temperature reached approximately 94 ℃, the hot plate surface temperature was raised to a maximum temperature level of 540 ℃. The change in hot plate settings was done in order to raise the tissue temperature above 100 ℃ overcoming the latent heat of vaporization of water. The dielectric properties were recorded every 12-15 s. The transient temperature profiles of the tissue were independently measured at the site of measurement with the fiber optic temperature sensor at a sampling rate of 1 Hz. The dielectric probe and the temperature sensor were thoroughly cleansed with sterile alcohol swabs between the measurements.

Ex vivo bovine muscle tissue has been employed as a surrogate tissue for evaluation of fibroid ablation technologies [44], [161]. We also conducted dielectric measurements on ex vivo bovine muscle samples for comparative assessment against fibroid measurements.

3.2.3 Data processing and parametrization

The measured dielectric data were interpolated to a uniformly spaced linear grid of 127 temperature points from 23 °C to 150 °C at each of the measured 401 frequencies for each tissue sample. Four non parametric curves i.e. mean, upper and lower envelopes and standard deviation were estimated from the interpolated data at each frequency to describe the range and distribution of observed data values as functions of temperature. The data was compared with the bovine muscle dielectric data.

A parametric model was employed to represent the temperature and frequency dependent dielectric data in a form that can be used in the computational models using a fitting approach presented in [63], [135]. A piecewise linear function was utilized to approximate the linear trends of the dielectric data along the temperature T in three distinct mutually continuous temperature

50

intervals: 1) interval of moderate linear dielectric dependencies at low temperatures from 23 °C to the temperature T_1 (~ 100 °C) , 2) interval of temperatures around water vaporization point from T_1 to T_2 (above 100 °C) where dielectric properties are expected to significantly drop and 3) Interval above water vaporization point from T_2 to 150 °C where dielectric properties are expected to settle to lowest values and become constant. Coefficients of continuous linear functions in the respective interval were further fitted as functions of frequency. The functional form of the fitting equations are listed in Appendix A.

Two-dimensional error surfaces were plotted to present how well our parametric model matched the actual non parametrized data. Absolute difference was calculated (at each point) between the parametric envelopes and their corresponding non parametric envelopes across all measured temperature and frequency values.

Finally, the measured temperature data were also utilized for the calculation of thermal dose to provide a means for evaluating the changes in dielectric properties based on the time-temperature history of fibroid tissue samples during heating using the thermal isoeffective dose formulation. As described in [135], dielectric properties were evaluated as a function of the logarithm of thermal dose (cumulative equivalent minutes at 43 °C, CEM43).

3.3 Results

Table 3.1 lists information about the excised fibroid tissue samples received for dielectric measurements. For samples 1, 2 and 4, only one measurement was taken per fibroid sample. For sample 3, five measurements were recorded, and for samples 5 and 6, two measurements were recorded per fibroid sample. Images of sample fibroids are shown in Figure 3.2.

Table 3.1 Tissue samples description.

Sample	Patient age (Yrs.)	Fibroid size (cm x cm x cm)	Fibroid weight (g)	Number of Measurements
1	42	1.7 x 1.1 x 0.9	1.59	1
2	51	2.0 x 2.0 x 1.5	4.60	1
3	46	5.5 x 4.0 x 4.5	78.01	5
4	51	2.0 x 1.5 x 1.0	1.38	1
5	49	3.5 x 3.0 x 0.9	4.38	2
6	49	2.7 x 2.0 x 0.8	2.47	2
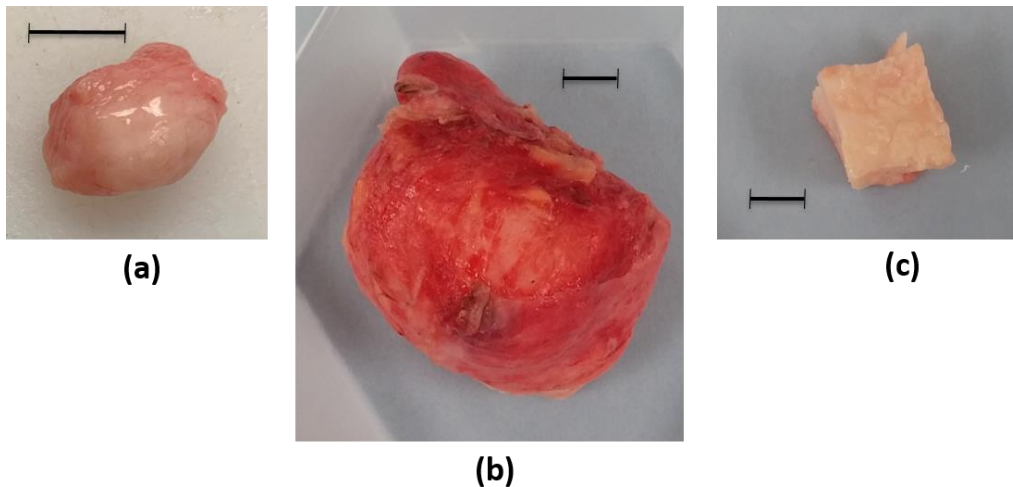
Figure 3.2 Pictures of uterine fibroid samples; a) sample 1, b) sample 3 and c) a section taken from sample 3. The solid bars in each panel provides a scale of 1 cm length.

Figure 3.3 displays the distribution of broadband dielectric properties at room temperature i.e. 23 ℃ over the frequency range of 500 MHz to 6 GHz for all fibroid samples. The standard deviation, mean, upper and lower envelopes are shown in Figure 3.3(a) for relative permittivity, ε_r, and Figure 3.3(b) for effective conductivity, σ_{eff}, for all measured fibroid samples. To study the difference between inter-sample and intra-sample variability at room temperature, we also plotted the distribution measurements taken on sample 3 (with $m = 5$ measurements) against the overall distribution of all fibroid samples (with total 12 measurements).
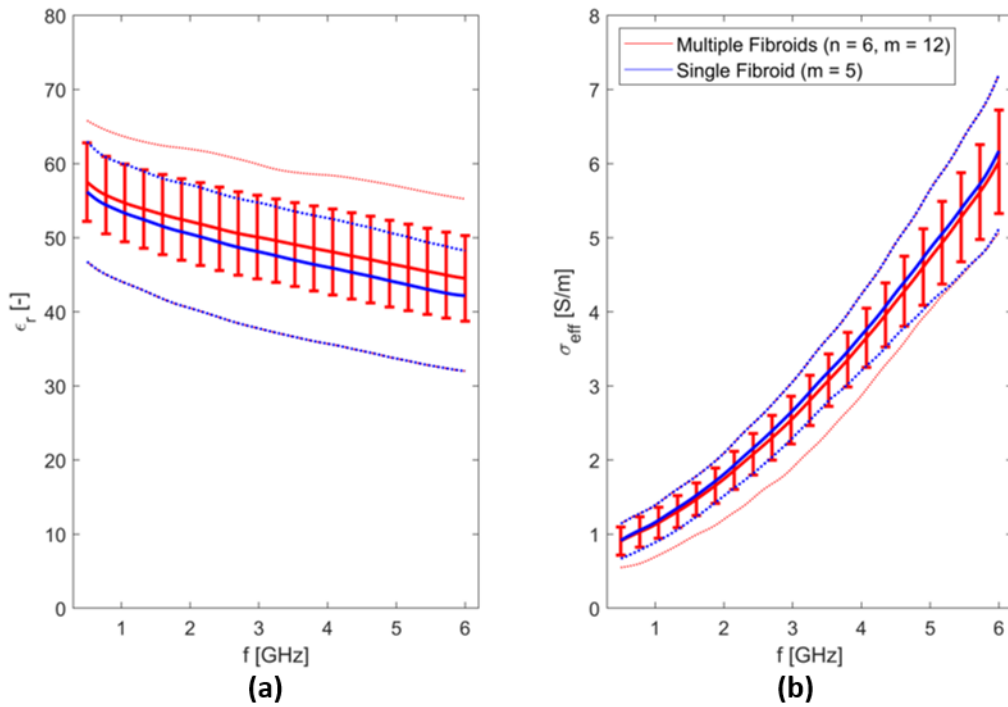
Figure 3.3 Non-parametrized distribution of broadband dielectric properties at room temperature (23 ℃) over a frequency range of 500 MHz to 6 GHz. a) Relative permittivity, ε_r, and b) effective conductivity, σ_{eff} , of excised human uterine fibroids. Inter-sample and intra-sample variability is illustrated using red and blue curves, respectively. The red curve represents data from all fibroid samples ($n = 6$, $m = 12$) and the blue curve represents data from a single fibroid with 5 measurements. Solid lines depict the mean envelope values and dotted lines show the maximum and minimum envelope values for the dielectric measurements. Error bars show the standard deviation of data taken from all samples.

Figure 3.4 compares the non-parametrized distribution of the measured broadband dielectric properties of excised human uterine fibroids (from 23 ℃ to 150 ℃) and *ex vivo* bovine muscle samples (from 31 ℃ to 150 ℃) as a function of temperature at frequencies of 915 MHz, 2.45 GHz and 5.8 GHz, which are frequencies under consideration for fibroid thermal ablation technologies.
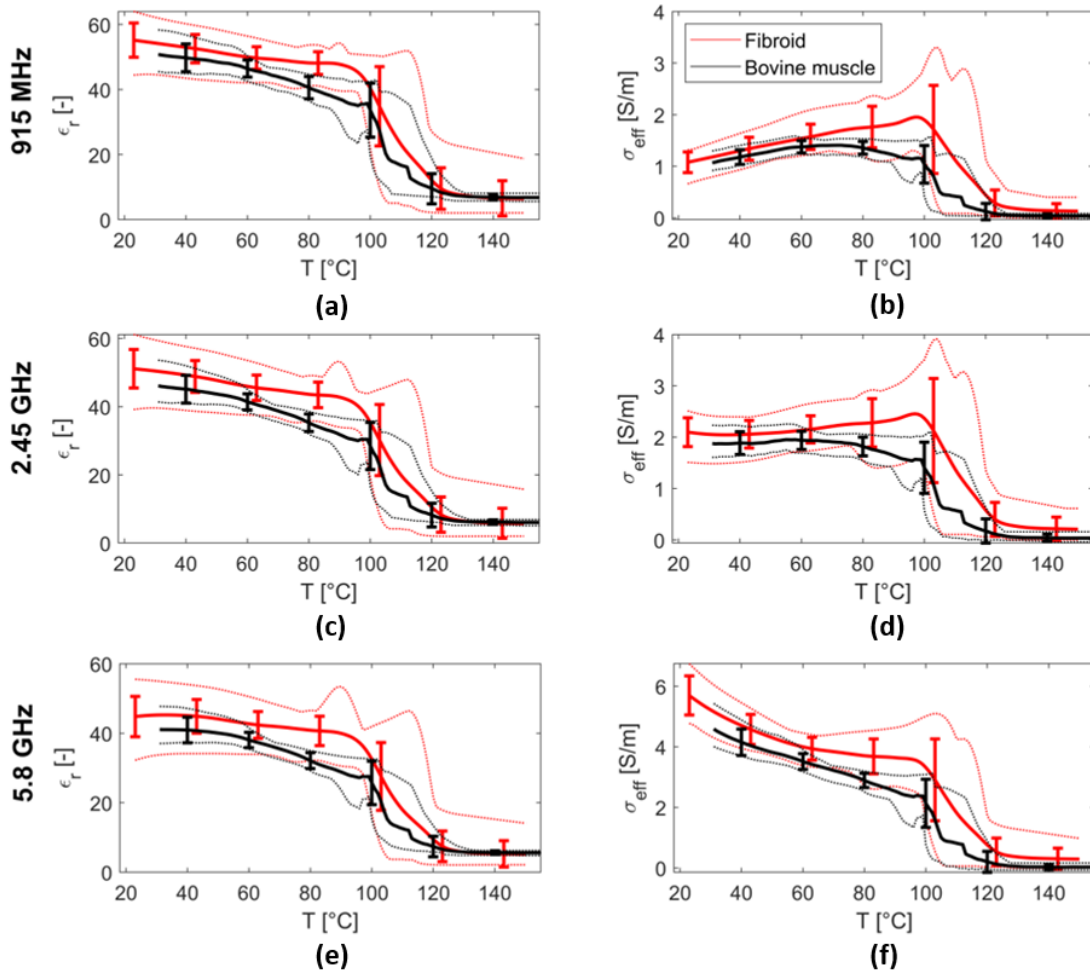
Figure 3.4 Comparison of non-parametrized distribution of broadband dielectric properties of *ex vivo* human uterine fibroids (over the temperature range 23 ℃ – 150 ℃) and bovine muscle (over the temperature range 31 ℃ – 150 ℃) at 915 MHz, 2.45 GHz and 5.8 GHz. Panels a, c and e show the relative permittivity, ε_r, and panels b, d and f show the effective conductivity, σ_{eff} of excised tissues. The red curves represent data from all fibroid samples (n = 6, m = 12) and black curves represent data from bovine muscle samples (6 samples). Solid lines show the mean envelope values and dotted lines show the upper and lower envelope values for the dielectric measurements. Error bars show the standard deviation of data taken from all samples.

Table 3.2 lists the coefficients for the parametric model computed by using linear least squares optimization technique for the mean, upper and lower envelopes of relative permittivity, ε_r and effective conductivity, σ_{eff}.

Table 3.2. Fitting parameters for dielectric properties of fibroids. The fitting co-efficient, $b_{01}, b_{02}, b_{03}, b_{11}, b_{12}, b_{13}, b_{21}, b_{22}, b_{23}$, are defined for the relative permittivity, ε_r and effective conductivity, σ_{eff} for the three envelopes (mean, upper and lower) separately. In addition, corresponding transition temperatures T_1 and T_2 are also presented.

Parameters	Mean Envelope		Upper Envelope		Lower Envelope	
	For ε_r	For σ_{eff}	For ε_r	For σ_{eff}	For ε_r	For σ_{eff}
b_{01}	0.119	0.082	0.093	0.099	0.234	0.083
b_{02}	-2.454	0.291	-1.988	0.248	-3.576	0.221
b_{03}	56.843	0.769	64.518	1.005	47.989	0.553
b_{11}	0.483	0.001	0.490	-0.008	0.440	0.014
b_{12}	-4.638	0.253	-4.168	0.289	-4.440	0.078
b_{13}	50.377	1.748	51.889	2.728	42.525	1.280
b_{21}	0.082	-0.004	0.298	8.8×10^{-4}	0.010	-5.4×10^{-4}
b_{22}	-0.878	0.059	-3.094	0.127	-0.066	-2.3×10^{-5}
b_{23}	8.279	0.103	23.689	0.038	2.361	0.038
T_1 (°C)	95	98	115	114	96	100
T_2 (°C)	121	125	123	124	106	105

Figure 3.5 shows the parametrized distribution for the measured relative permittivity and effective conductivity at 915 MHz, 2.45 GHz, and 5.8 GHz over the temperature range of 23 ℃ to 150 ℃. The mean, upper, and lower envelopes of the measured data are shown in dotted lines with their corresponding parametric fits in solid lines.
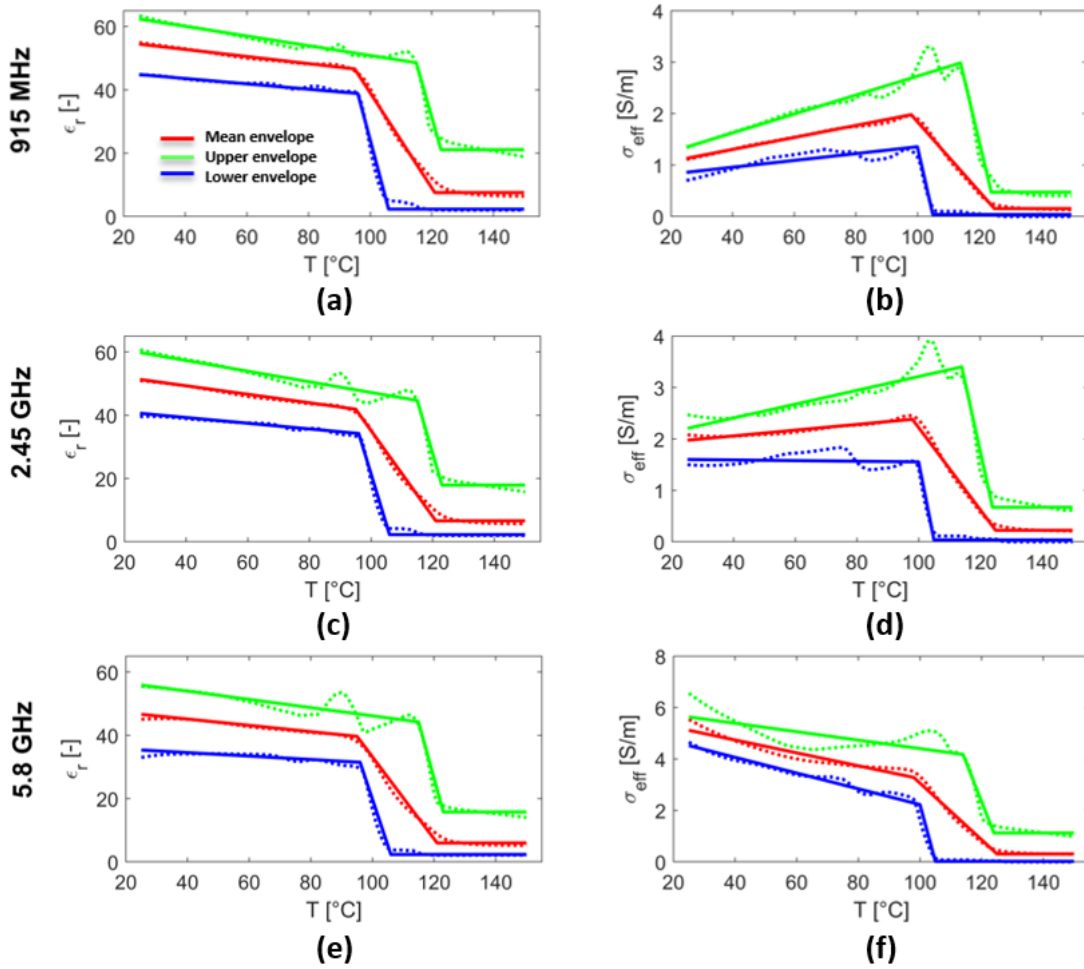
Figure 3.5 Parametrized distribution of broadband dielectric properties at 915 MHz, 2.45 GHz and 5.8 GHz over the temperature range 23 ℃ – 150 ℃. Panels a, c and e show the relative permittivity, ε_r, and panels b, d and f show the effective conductivity, σ_{eff} of excised human uterine fibroids. Solid lines provide parametrized linear piecewise functions for the corresponding non-parametrized data illustrated by the dotted lines of the same color.

Figure 3.6 displays the raw dielectric data measurements from six fibroid samples (shown as a scatter plot, with one color assigned to each sample) overlaid on the parametric linear piecewise functions for mean, upper and lower envelopes.
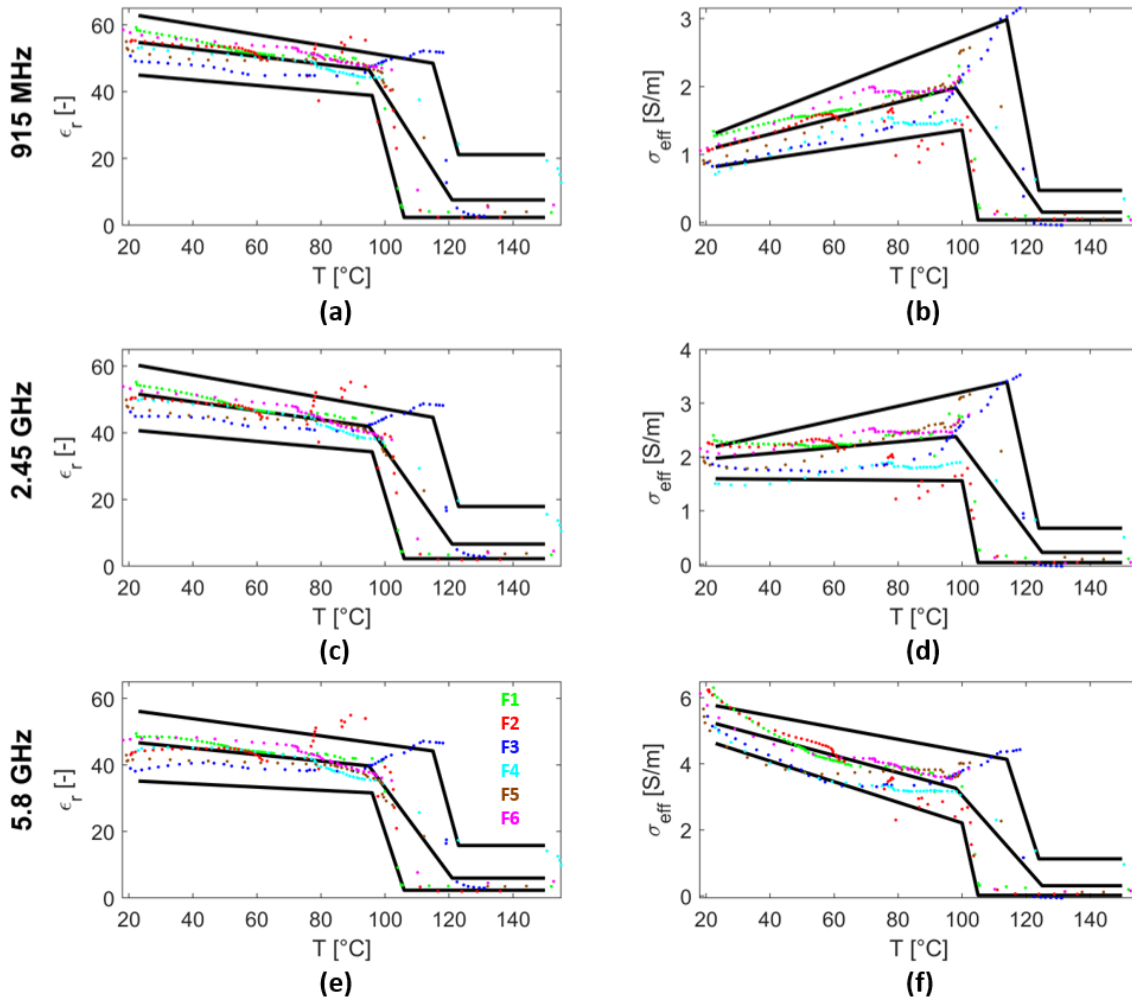
Figure 3.6 Illustration of raw dielectric measurements from six fibroid samples and parametrized distribution of broadband dielectric properties at 915 MHz, 2.45 GHz and 5.8 GHz over the temperature range 23 ℃ – 150 ℃. Panels a, c and e show the relative permittivity, ε_r, and panels b, d and f show the effective conductivity, σ_{eff} of excised human uterine fibroids. Solid black lines provide parametrized linear piecewise functions (mean, upper and lower envelopes) for the corresponding raw data of six fibroid samples illustrated by the colored scatter plots.

Figure 3.7 illustrates the absolute error between measured dielectric data and the parametric

fit for mean, upper and lower envelopes of the dielectric properties as a function of temperature

and frequency, to estimate the goodness of parametric fits.

Figure 3.8 illustrates the parametrized distribution of dielectric properties of fibroid tissue

as a function of the logarithm of thermal dose (CEM43). The fitted piecewise functions of relative
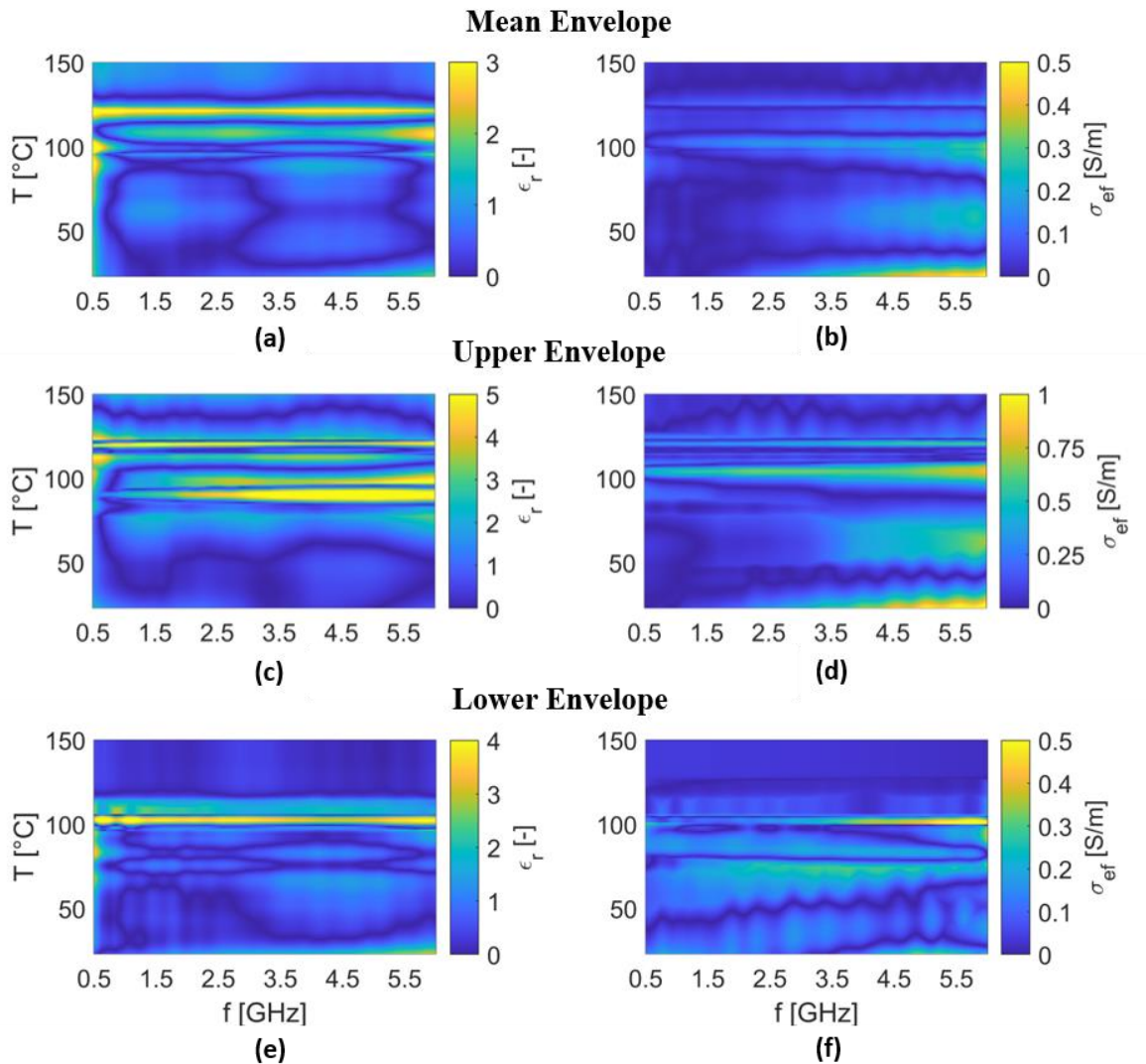
Figure 3.7 Error surfaces for the parametrized models of dielectric properties i.e. mean (panels a and b), upper (panels c and d) and lower (panels e and f) envelopes across all measured frequencies and temperatures.

permittivity and effective conductivity as a function of thermal dose are overlaid on the parametrized data. The corresponding fitting coefficients are provided in Appendix B.
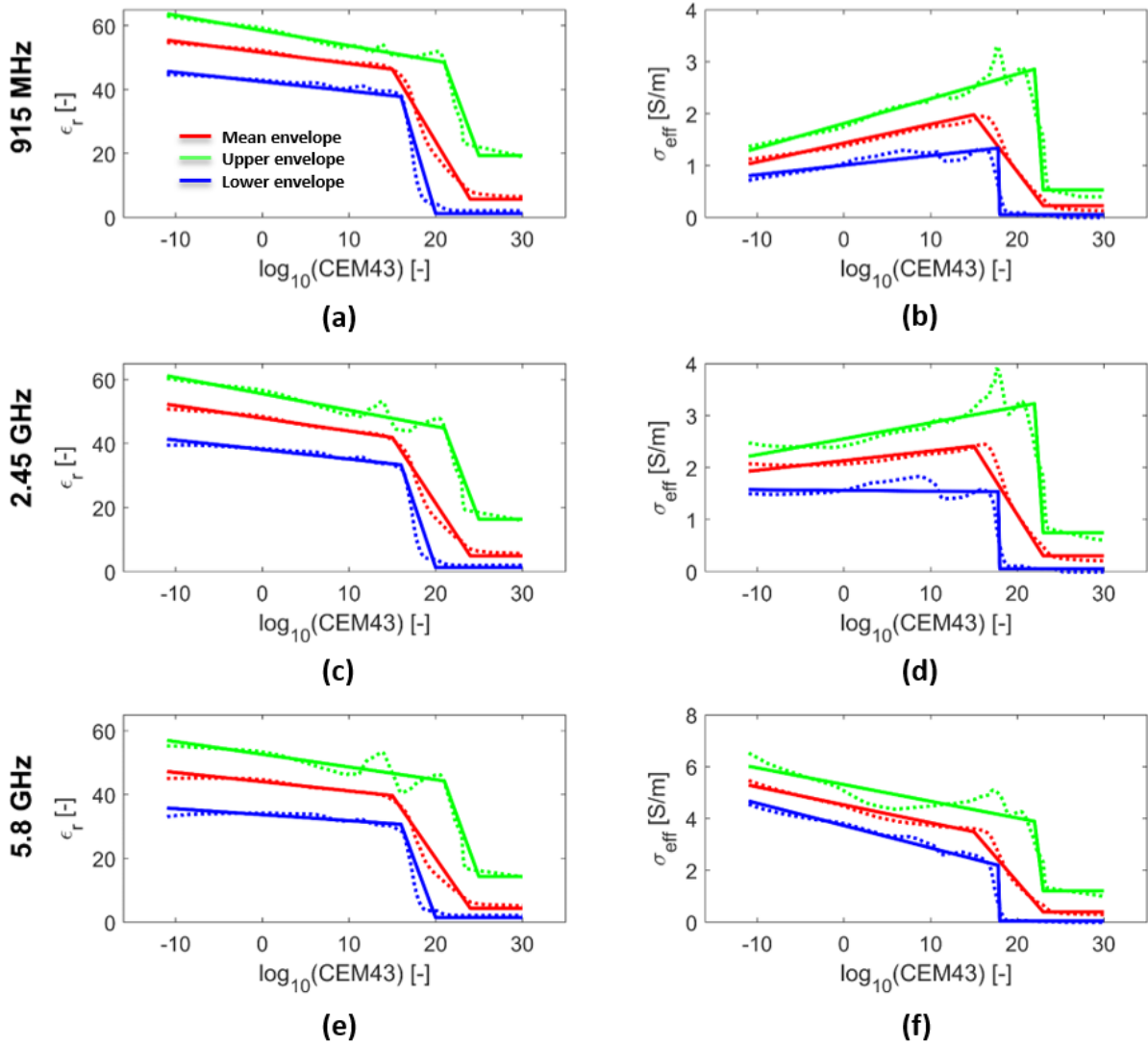
Figure 3.8 Parametrized dielectric data of human uterine fibroids at 915 MHz, 2.45 GHz and 5.8 GHz as a function of thermal isoeffective dose (CEM43). Panels a, c and e show the relative permittivity, ε_r, and panels b, d and f show the effective conductivity, σ_{eff} of excised human uterine fibroids. Solid lines provide parametrized linear piecewise functions for the corresponding non-parametrized data illustrated by the dotted lines of the same color.

3.4 Discussion

The present study was conducted to report on the measurements of the broadband dielectric properties of fibroid tissue at ablative temperatures, due to the lack of such data in the literature. Furthermore, parametric models were derived from the measured data to characterize the dependence of the dielectric properties on the tissue temperature and frequency. The tissue dielectric properties in the form of piecewise linear functions can be used in computational models of microwave tissue heating to predict and estimate 1) the spatial electric field distribution due to the MWA radiation, 2) power absorption and 3) transient temperature profiles within tissue [162]. Moreover, the dielectric properties reported in the present study can guide the design of tissue mimicking phantoms for the MWA of uterine fibroids [66].

To quantify the extent of fibroid tissue dielectric properties variation with respect to different samples and frequency, we plotted the dielectric data for multiple fibroids at room temperature from 500 MHz to 6 GHz in Figure 3.3. The distribution of multiple fibroids shows a decreasing trend for ε_r values with average values starting from 57.5 at 500 MHz and dropping to 77.4% (of its baseline value) at 6 GHz with a decrease rate of ~2.4 units/GHz as shown in Figure 3.3(a). On the other hand, an increasing trend is seen in σ_{eff} with average values starting from 0.92 S/m at 500 MHz and rising to a value of 6.02 S/m at 6 GHz with an increase rate of 0.93 S/m/GHz as illustrated in Figure 3.3(b). Similar trends and variability was observed for the distribution of sample 3 for both ε_r and σ_{eff} with slightly lower average values (~1-2 units lower than the average values for all fibroid samples) for ε_r , with a decrease rate of ~2.5 units/GHz in the measured range (Figure 3.3 (a)) whereas the average σ_{eff} values were almost similar (Figure 3.3 (b)). Hence, from our experimental observations we saw no significant difference in the variability of broadband dielectric values within the same fibroid sample and between different fibroid samples at 23 ℃.

Figure 3.4 displays a comparison between the dielectric properties of excised human uterine fibroids and bovine muscle tissue. The average baseline relative permittivity values at 31 ºC for bovine muscle tissue are ~4 units lower than the fibroid values and the effective conductivity values are ~0.18-0.5 S/m lower than the corresponding fibroid properties. However, at elevated temperatures, the difference between the dielectric properties increases at all measured frequencies with mean bovine muscle properties lower than the fibroid properties. The maximum difference in relative permittivity values can be observed around 92 ºC i.e. ~ 10-12 units. For effective conductivity values, the maximum deviation of ~0.8-1.1 S/m can be seen around 98 ºC in the fibroid and bovine tissue. It should be noted here that the bovine muscle samples were taken from a local meat supplier; storage conditions and time between excision and sample acquisition, and their impact on the measured properties, are thus unknown. A comparison of simulated ablation zones when using dielectric properties of uterine fibroids and bovine muscle is provided in Chapter 5. Further research is required to compare not only the dielectric properties but also the thermal, mechanical and structural properties of freshly excised bovine muscle samples, to better assess the suitability of bovine muscle as a surrogate tissue for evaluating fibroid ablation technologies.

The analysis of the parametrized model of relative permittivity, ε_r, in Figure 3.5(a, c and e) reveals that the baseline values at 23 ºC are relatively high at lower frequency as compared to the higher frequencies. The baseline of mean envelope yields value 54.7 at 915 MHz which reduces to 85.2% at 5.8 GHz. It was observed that the average values of ε_r drop gradually by ~ 0.1 units/ºC from their baseline values for all the frequencies 915 MHz, 2.45 GHz, and 5.8 GHz in the temperature interval of 23 ºC < T < 95 ºC. Whereas in the temperature interval of 95 ºC < T< 121 ºC, a sharp drop with a slope of ~ -1.3-1.5 units/ºC was seen for the mean envelope values. At 121 ºC, an overall drop of ~ 86 - 87 % from the average baseline value of ε_r was observed for 915

MHz, 2.45 GHz and 5.8 GHz. This drop is generally attributed to tissue desiccation and water vaporization. For the interval, 121 ℃ < T <150 ℃, the ε_r values remain fairly constant at values < 10 units. The upper and the lower envelopes were plotted to provide a detailed account on the inter-sample variability of relative permittivity of measured fibroid tissues. A few perturbations were seen in the upper envelope values around 100 ℃ due to water vaporization and potential displacements caused by bubbles [163]. In this temperature range, the tissues beneath the top surface heat quicker than the top surface tissues and explosive ejection of surface tissue happens [164] which could be heard in the form of a "pop" sound during the experiment. The probe may not have remained in direct contact with the tissue if the tissue in contact with the probe tip was popping which could have led to measurement inaccuracies.

The examination of parameterized models for effective conductivity values shows a contrast in trend as compared to relative permittivity values which is evident from Figure 3.5(b, d, and f). The baseline conductivity values are low at lower frequencies as compared to the higher frequencies. The baseline mean envelope value at 915 MHz is 1.1 S/m rising by ~ 4.1 S/m at 5.8 GHz. It can be seen in the Figure 3.5(b and d) that the mean envelope values for σ_{eff} rise by ~ 0.02 S/m/℃ from the baseline value at 915 MHz and slowly rise (~0.005 S/m/℃) at 2.45 GHz in the temperature interval of 23 ℃ < T < 98 ℃. However, at 98 ℃ for 5.8 GHz, the σ_{eff} drops to 63.5% of its value at 23 ℃. In the temperature interval of 98 ℃ < T< 125 ℃, a decrease rate of ~ 0.07-0.11 units/℃ was seen for mean envelope values. At 125 ℃, the mean envelope reduced to ~ 86 - 89% for 915 MHz and 2.45 GHz from their corresponding baseline values at 23 ℃ whereas a 94 % drop is observed in the case of 5.8 GHz. This drop is again attributed to tissue desiccation and water vaporization. For the interval, 125 ℃ < T <150 ℃, the ε_r values remain constant (close to zero). The upper and the lower envelope provides a detailed account on the inter-sample variability

of measured fibroid tissues effective conductivity values. While the trends observed in this study are consistent to prior studies of dielectric properties of liver [59], [135], [154], [165], [166] and lung [63] tissues, however the absolute values are different in the case of fibroids.

It can be seen from the scatter plots in Figure 3.6 that the measured dielectric data of individual fibroid samples has a sharp transition at temperatures close to 100 ℃. Moreover, for frequencies less than 2.45 GHz, the effective conductivity increases with temperature till ~98 ℃ and then decreases sharply. The piecewise linear function was used for the parametric fitting of the fibroid dielectric data since it allows a way to capture the rise and fall of dielectric data with respect to frequency and temperature, which could not be captured otherwise with a sigmoid function.

Figure 3.7 presents a quantitative analysis of the errors in our parametric fittings (shown in Figure 3.5) as compared to the non-parametric values at each point across all measured temperature and frequency for all three envelopes. The maximum error in ε_r values is observed around 100 ℃ at all frequencies for all three envelopes as shown in Figure 3.7(a, c and d). The maximum error in σ_{eff} values is generally observed around higher frequencies at baseline temperature and around 100 ℃ as illustrated in Figure 3.7(b, e and f). It is apparent from Figure 3.7 that the maximum deviation of the parametric fitting was observed in the case of upper envelope and the mean envelope has the highest match with the non-parametric data.

Tissue dielectric properties are susceptible to variations which can be broadly classified into: 1) variations due to measurement setup errors and 2) tissue sample variations. Moreover, the rapid changes in the tissue's physical state due to water vaporization at higher temperatures (i.e. > 100 ℃) add considerable variability to measurements. We have tried to capture the range of data variations observed in our experiments at these elevated temperatures (in terms of upper, lower

and mean values). In comparison to other tumor tissues, the variations seen in fibroid dielectric properties at baseline room temperature are relatively higher than liver and colon tumors and are in the similar ranges as that of the variations in excised breast tumors [167]. In fibroids, the standard deviation of ε_r ranges from ±5.21-5.62 and σ_{eff} ranges from ± 0.2-0.28 S/m for 915 MHz and 2.45 GHz respectively. While in an *ex vivo* malignant liver tissue [168] and colon tissue [169], the standard deviation of ε_r is ±3.0-3.1 units and σ_{eff} ranges from ± 0.08-0.11 S/m at 915 MHz and 2.45 GHz respectively. Due to the heterogeneity of fibroid tissues, it was anticipated that there will be substantial variation in the dielectric properties of fibroid tissue taken from several samples and also at different locations of the same tissue sample.

Figure 3.8 provides parametric models of dielectric properties with respect to the logarithm of thermal dose, which allows for changes in dielectric properties to evaluate as a function of time-temperature history, rather than temperature alone.

In the present study, we employed an established high-temperature dielectric probe kit for measuring dielectric properties of tissue at elevated temperatures, similar to other studies ([63], [64], [170]–[172]). A challenge with dielectric property measurement techniques that require contact with the sample is that heating of the probe may lead to additional uncertainties in measurements. Non-contact dielectric probe methods, such as transmission-based antenna or waveguide techniques, may provide a means to reduce potential uncertainties due to measurement probe heating.

One of the limitations of this study is that the dielectric characterization of fibroids was done *ex vivo*. While it is appealing to measure the dielectric properties of tissue in their native *in vivo* state, the presence of blood near the dielectric probe when inserted into perfused tissue can cause additional uncertainties [135], [168]. Tissue extraction has minimal effects on dielectric

properties if the measurements are performed within few minutes of excision [173] [174], however in our study due to the technical limitations of transporting the tissue to the experimental setup, the measurements were performed 24-36 h post-surgery. Secondly, tissue sample availability was limited as hysterectomy is predominantly an elective procedure and retrieval of a whole fibroid from the extirpated uteri is difficult. Thirdly, the variability analysis with respect to tissue composition is limited by the fact that pathology reports of the tissue samples were not available.

3.5 Conclusion

The temperature-dependent dielectric properties of uterine fibroid over a broadband frequency (0.5-6 GHz) and temperature range (23-150 ºC) have been reported for the first time in this study. We have developed parametric models for the dielectric properties of fibroids which can be used in computational models and tissue mimicking phantoms for design, optimization and testing of therapeutic devices for microwave frequencies.

Chapter 4 - Design and Evaluation of Microwave Ablation Applicators for Transcervical Fibroid Ablation

4.1 Introduction

Microwave ablation (MWA) is under investigation as a minimally-invasive thermal ablative approach for treatment of uterine fibroids. MWA has the potential of producing consistently higher tissue temperatures (for larger ablation volumes) in relatively short period of time in highly perfused tissues. MWA has already been employed for the treatment of tumors in the liver, lung and kidney [47] in clinical settings. Recently, there has been a growing research interest in using MWA for the treatment of fibroids (via percutaneous [10] [11] and transcervical [49]–[52][44], [45] approaches). The basic components of MWA are high power- microwave generator, and a microwave applicator for power delivery from the generator to the target tissue. The applicator consists of a feedline transmission cable (most commonly coaxial cable) with the distal tip modified to create an antenna that radiates microwave power to the surrounding tissue [132]. The most commonly used MWA applicators employ needle-based antennas (monopole [175], dipole [176] and slot antennas[177]) which yield a nearly spherical ablation pattern. Antenna designs for microwave tissue ablation have recently been reviewed in [132]. The design of a microwave antenna is the most integral part in the development of a microwave ablation technology since the ablation patterns rely on the antenna design.

During fibroid ablation, thermal sparing of adjacent tissues to the fibroid is of high priority in order to preserve the woman's ability to bear children. Hence, the objective of fibroid ablation treatment is to maximize the non-perfused volume of fibroid for symptom relief [43] by inducing cytotoxic temperatures (>55-60°C [37]) in the fibroid tissue, while strictly minimizing the collateral damage to the surrounding healthy tissues of uterus [44], [45] and the organs around

66

uterus [46] (e.g. bowel, bladder) by ideally maintaining sub-ablative temperatures in the adjacent non target tissues. Transcervical microwave ablation of fibroids offers the opportunity for a minimally invasive [53] access through a body cavity (cervical canal), thus minimizing the risk of damaging the organs adjacent to uterus (such as, rectum, bladder, and the intestinal tract). Technologies for hysteroscopy-guided ablation of fibroids via a transcervical approach (illustrated in Figure 4.1.) are attractive for submucosal fibroids because of their reduced invasiveness compared to other approaches [53]. Existing MWA applicators are not compatible with the hysteroscopy guided ablation of uterine fibroids in terms of the dimensions of the applicator and the shape and size of the ablation patterns. Hence, there is a need for site-specific design of MWA applicators transcervical treatment of fibroids.
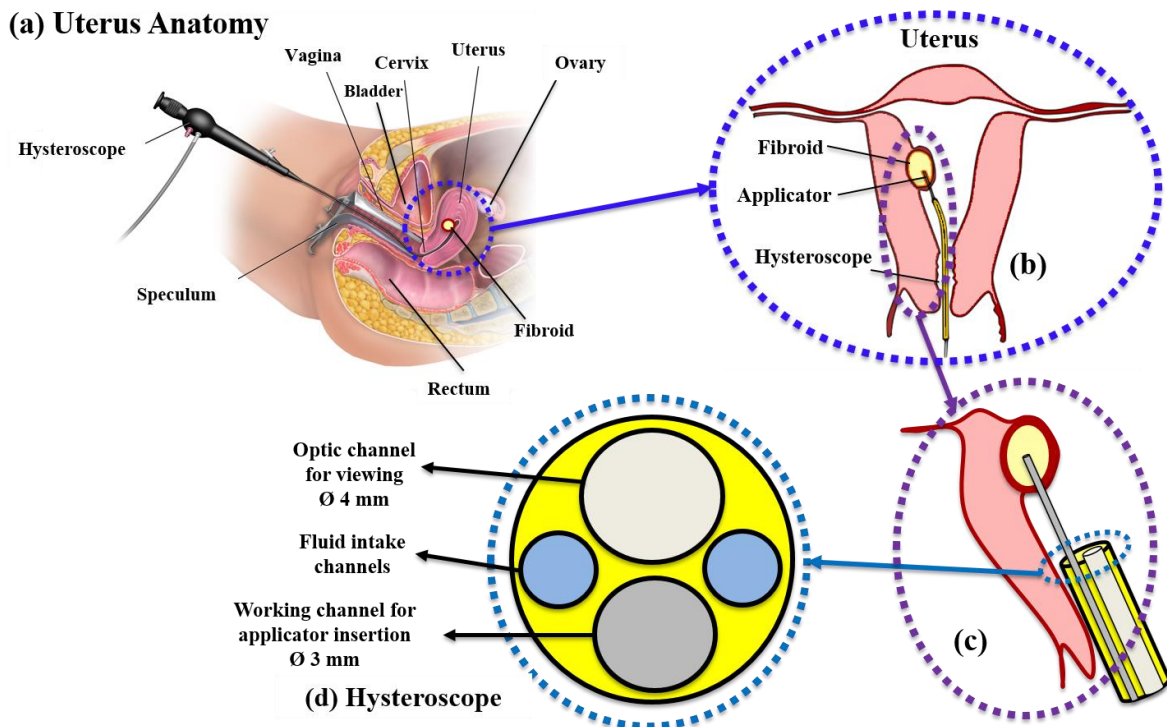
Figure 4.1 Transcervical hysteroscope microwave ablation of fibroids; (a) anatomy of uterus ([58]; https://commons.wikimedia.org/wiki/File:Hysteroscopy.png), (b) insertion of transcervical microwave applicator into the fibroid through the cervix via hysteroscope, c) a closer view of applicator insertion inside the fibroid (d) Terminal portion of hysteroscope with channels with different channels for optics, fluids and working channel for applicator insertion.

The most common frequency used for MWA is 2.45 GHz [46]. The electric field radiated by an MWA applicator placed inside the fibroid tissue is absorbed in the target tissue producing frictional heat and ablative temperatures and subsequently resulting in tissue coagulation [131], [132], [134]. The spatial profile of the electric field radiated into the target tissue is determined by the geometry of the antenna, operating frequency, electromagnetic properties of the tissue [134] [59], [135] [63] and the power transfer efficiency of the applicator from the feedline transmission line to the radiating part of the antenna. Several antenna designs have been developed for MWA of other site-specific treatments and the goals of antenna design such as 1) an efficient power transfer from MW generator to tissue and 2) a radiation pattern comparable to the shape and size of the target tissue, are applicable in fibroid MWA applicator design. However, unlike the treatment of malignant tumors, it is not essential to ablate the entire fibroid tissue volume, which comes with a high likelihood of damaging the surrounding tissue, since the aim of fibroid ablation is symptom alleviation for which 100% ablation of the fibroid tissue may not be needed [40] [41]. A technical challenge which remains unresolved in the previous applicator designs due to which they could not be employed for site specific fibroid ablation is the sphericity of ablation zones (see Figure 1.2). There exists a tradeoff between the fractional volume of the fibroid that is ablated and the safety of the adjacent non-target tissues due to the gradual temperature roll off from ablative to sub-ablative temperatures. Another challenge is the power attenuation along the feedline cable of the microwave antenna which leads to heating of the cable and may cause heating of adjacent tissues and breakdown in structural integrity of the cable. In most ablation applicators, to enable high power use, these issues are mitigated by employing active cooling strategies (e.g. water or gas cooling) [133].

Apart from the design challenges of a MWA applicator there are some added constraints in a hysteroscopy guided transcervical MWA of fibroid. The applicator diameter should be less than the working channel of the hysteroscope (typically, 3 mm), the length of the applicator should be more than the length of the hysteroscope (i.e. more than 32 cm), and the applicator should provide a sharp radial transition from ablated to non-ablated region with a spherical ablation profile for small submucosal target fibroids (1-3 cm diameter) to maximize ablation outcome and simultaneously minimize the risk of damaging the surrounding tissues.

During the design and evaluation, and manufacturing validation, of microwave ablation devices, tissue mimicking phantoms [178]–[186] serve as powerful tools for comparative assessment of candidate technologies. While experiments in *ex vivo* and *in vivo* tissue may be more representative of the intended clinical use, tissue mimicking phantoms can be constructed in a repeatable and reliable manner. Tissue mimicking phantoms with material properties tailored to match the target tissue properties are helpful for assessing thermal profiles of prototype ablation devices in a benchtop experimental setup [181], [183]. However, majority of the tissue mimicking phantoms for thermal ablations require use of invasive temperature sensors for monitoring ablations which are prone to placement inaccuracies. Thermo-chromic gel phantoms provide a means for spatial assessment of thermal profiles as there is a gradual and permanent change in the color of the gel when exposed to specific ablative temperatures (~60 ^{o}C) [179], [182], [184].

The objectives of this study were 1) to design an MWA applicator to create spherical ablation zones inside 1-3 cm diameter uterine fibroids suitable for use under hysteroscopic guidance, 2) to evaluate the antenna performance in a benchtop experimental setup and 3) to design a tissue mimicking phantom for the assessment of ablation profiles created by the MWA applicators.

4.2 Methods

4.2.1 Applicator design

An applicator for transcervical hysteroscopic microwave ablation of fibroids was designed with the following goals: 1) diameter of applicator less than 3 mm (i.e. inner diameter of the working channel of hysteroscope), 2) length of the radiating element of antenna less than 5 mm suitable for central placement inside a 1 cm diameter fibroid, 3) shape of the radiation pattern should be aligned with the shape of the fibroids which are near-spherical, and 4) the transition zone between the ablated and thermally unaffected zone should be as small as possible for maximal fibroid ablation volume and minimal damage to surrounding tissues.

It was hypothesized that a water-cooled monopole microwave antenna design operating at a frequency higher than conventionally employed 2.45 GHz MWA applicator i.e. 5.8 GHz applicator due its shorter wavelength would provide shorter, spherical ablation zones in 1-3 cm diameter target tissue to maximize fibroid ablation volumes while thermally protecting the surrounding tissues. Water cooling has been employed for several reasons in the design: 1) to prevent overheating of the cable 2) to provide a suitably-matched impedance for the radiator, 3) to limit backward heating along the shaft, and 4) high electrical permittivity of water reduces the electromagnetic wavelength and consequently decreases the antenna radiating length [132].

4.2.1.1 Applicator diameter

Since the applicator diameter needs to be less than 3 mm, a UT-34 feedline coaxial cable (from Microstock Inc.) was centrally placed inside two concentric semi-rigid polyimide tubes (American Durafilm). Water cooling was incorporated in a monopole antenna through the shaft of the applicator via these polyimide tubes. The outer tube (outer diameter = 2.146 mm and inner diameter = 1.892 mm) was used as the water outflow and the inner tube (inner diameter = 1.422

mm and wall thickness = 0.038 mm) served as an inflow tube. Since the outflow tube serves as a catheter enclosing the applicator elements, it was extended beyond the monopole tip whereas the inflow tube was cut 0.5 mm above the monopole junction. This assembly of the selected components provides a continuous flow of water inside the applicator and back to the reservoir with an applicator diameter which is compatible to the size of the hysteroscope working channel (i.e. outer catheter diameter ~2.15 mm < 3 mm).

4.2.1.2 Antenna length

The length of the applicator's radiating element depends upon the electromagnetic wavelength, λ, inside the tissue. Usually, the antennas performs efficiently if the λ is of the order of the length of the radiating element of antenna which can be calculated using the following equation:

$$\lambda = \frac{c_o}{f\sqrt{\varepsilon_r}}$$

where c_o = speed of light = 3 x 10^{-8}, f = frequency, and ε_r = relative permittivity which is a function of the diameter of coaxial cable, insulating catheter's thickness and dielectric properties of the catheter and surrounding tissue. In biological tissues, λ is in the order of a few cm which places a limit on the minimum length of the antenna radiating element for ablation applications [187].

For achieving maximum ablation volumes inside the target fibroid, the monopole junction (maximum temperature point) has to be placed at the center of the fibroid. Since we wanted an applicator for 1-3 cm diameter target fibroids, one of the major challenges we faced in the 2.45 GHz MWA applicators was that the monopole length is greater than the diameter of 1 cm fibroid [188]. In our application, the antenna length is limited by the 1 cm fibroid case since the distance from the monopole junction to the tip of the applicator must be $\leq$ 5 mm (radius of 1 cm fibroid). We chose a higher frequency of operation for our applicator design as it has a shorter wavelength

71

and was expected to reduce the length of the monopole. Once the frequency of operation of applicator was chosen, we designed an appropriate length of the antenna for our application.

A clearance of at least 1 mm is needed between the monopole tip and the antenna end for the water flow and an allowance of ~1.5 mm has to be kept for sealing the distal end of the applicator. Hence, the antenna monopole length has to be ≤ 2.5 mm to avoid applicator insertion beyond the fibroid diameter into the non-target tissues. We fixed the length of the monopole at 2.5 mm and tried to adjust the shape of the radiation pattern and reflected power with other antenna design elements in the computer simulations.

4.2.1.3 Radiation pattern

One of the design requirements for the MWA applicator was to create nearly spherical ablation zone to match the shape of 1-3 cm target fibroids for achieving maximum ablation volumes. The challenge in a monopole applicator design is undesirable heat along the antenna length due to the propagation electromagnetic wave along the outside of the antenna's outer conductor which leads to non-spherical ablation patterns [189]. In order to shape the radiation pattern, the electromagnetic heating loss along the applicator shaft needs to be restricted.

To resolve the aforementioned issue, two design elements: balun and dielectric loading were utilized as illustrated in Figure 4.2. A balun/choke [190], [191] consists of a conductor surrounding the outer conductor of antenna feedline with a dielectric separation in between and electrical shorting at the pend of the feedline cable (i.e. the monopole junction). According to the transmission line theory, a shorted quarter wavelength balun inhibits the wave propagation and current flow outside the outer conductor of the feedline cable due to its infinite input impedance which thereby leads to spherical ablation zones. The performance of a balun in shaping the antenna radiation pattern depends on length, width and axial position of the balun [189]. Moreover, a

balun's geometric specifications are adjusted at a specific applied power and treatment duration to achieve desired ablation patterns. In a practical design, the water inflow was maintained below the balun by creating electrical connection of the balun conductor at the junction point while mechanically leaving some space for the water inflow which can be seen in the cross-sectional view in Figure 4.2 to employ cooling below the balun in the applicator.

To further improve the sphericity of the ablation pattern, loading [187], [190], [192]–[194] of the radiating monopole was employed with the dielectric material of UT-34 coaxial cable (ε_r ~ 2.1).

Parametric length sweep optimization was employed in computational simulations for finding optimal dimensions of balun ('A' [mm]) and dielectric loading ('B' [mm]) while restricting the dimensions within the catheter and antenna dimensions
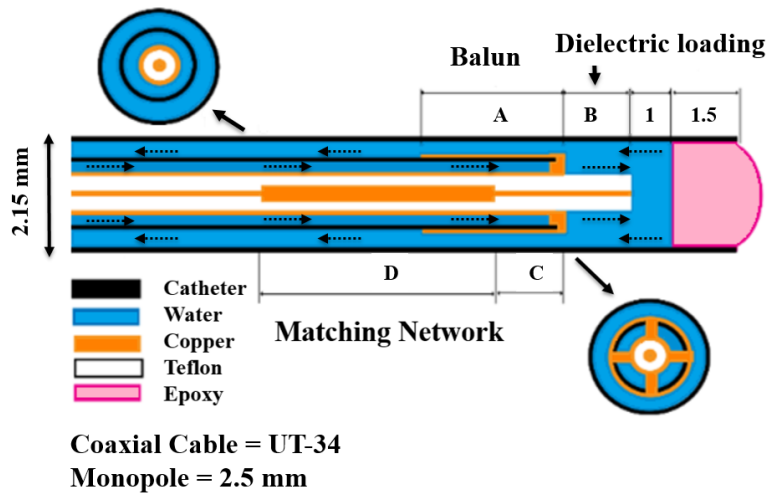
Figure 4.2 Schematic for applicator design. 'A' denotes the length of balun, 'B' denotes the length required for dielectric loading of the monopole, 'C' denotes the distance of the matching element from the monopole junction, and 'D' denotes the length of the matching element in the longitudinal section view of the applicator. The cross sectional view from the feedline cable and the tip of the applicator illustrates water channels and conductors.

4.2.1.4 Reflected power

Although a high feed impedance is desirable for suppressing the currents along the outside of the outer conductor (for spherical radiation patterns), it may lead to a large impedance mismatch between the feedline and the antenna and an inefficient transmission of power. The ratio of power delivered to the antenna to the power reflected back to the source due to impedance mismatch between the transmission line and antenna is represented by antenna return loss [187]. For maximum power transfer from the feedline to the antenna with negligible reflected power it is required to match the input impedance of the monopole radiator part (Z_L) to the feedline coaxial cable ($Z_O = 50\ \Omega$). If there is a mismatch between the feedline and the antenna, then the source experiences complex impedance which is a function of the line length. To resolve this issue, a matching network was designed inside the coaxial cable to increase the capacitance of the antenna. The inner conductor of the coaxial cable was widened (~0.2 mm) to reduce the distance between outer and inner conductor. This would provide a larger capacitance which would shift the phase of reflection coefficient along the coaxial cable for better impedance matching between the feedline and the antenna.

Following steps were taken for designing the matching network using admittance Smith chart:

1. First, the distance of the capacitive element from the monopole junction (denoted as 'C' in Figure 4.2) was calculated.

    a. The computer simulations of applicator were done in the tissue medium (as explained in computer modeling section) without the matching network. The reflection coefficient ($|S_{11}|$) was obtained at the port. Assuming a lossless coaxial cable, it was considered as $|S_{11}|$ at the monopole junction.

b. Next, the distance from the monopole junction was calculated such that the reflection coefficient shifts to a point in the left quadrant of the capacitive admittance in the admittance Smith chart.

- For this purpose, the wavelength,λ, was calculated inside the coaxial cable and traced back to the monopole junction as follows.

$$\lambda = c/(f\sqrt{\varepsilon_r})$$

Where c = speed of light = 3 x 10^8 [ms^{-1}], f = frequency of applicator = 5.8 GHz,

ε_r = dielectric constant of coaxial cable = 2.1.

Distance to junction = Modulo (length, $\lambda/2$)

$$\phi = 2\ \pi(\frac{\text{Distance to junction}}{\frac{\lambda}{2}})$$

Hence, the starting point at Smith chart = $|S_{11}|e^{j\phi}$.

- Then the angle 'θ' from the starting point to the horizontal line in the admittance Smith chart is calculated.

$$\theta = \pi + \phi$$

- The distance from the junction to capacitive element for the matching network is calculated from θ as follows:

$$C = \left(\frac{\theta}{2\pi}\right) * \left(\frac{\lambda}{2}\right)$$

2. Finally, the length of the capacitive element (denoted as 'D' in Figure 4.2) was calculated as follows:

a. Initial estimate of D was $\frac{\lambda}{4}$.

b. To move the reflection coefficient to the center of the Smith chart, optimal length of capacitive element, D is found by parameter sweep simulation (between 0 and $\frac{\lambda}{4}$) for given inner wire thickness to obtain the lowest reflection coefficient value i.e. smallest amplitude.

4.2.2 Computer Modeling

A two dimensional axis-symmetric finite element model was employed in COMSOL Multiphysics (v5.6, COMSOL Inc., Burlington, MA) due to the cylindrically symmetric geometry of applicator. While designing different antenna elements, we simulated the electromagnetic field and temperature distribution of the applicator within the target tissue to predict the ablation performance of the applicator *[195][196]*. Due to the lack of dielectric property data on uterine fibroids in the literature, we used the dielectric properties of ex vivo liver tissue for this analysis. Liver tissue is the most established and widely used tissue for testing ablation applicator designs *[188], [197]*.

4.2.2.1 Equations

The following governing equations were discretized with the finite element method (FEM).

1. The time-harmonic Helmholtz electromagnetic wave equation was solved for estimating the spatial distribution of the electric field in tissue as given in equation (4.1).

$$\nabla^2 \mathbf{E} + \beta_0^2 \left(\varepsilon_r - \frac{j\sigma}{\omega \varepsilon_0} \right) \mathbf{E} = 0, \tag{4.1}$$

In the equation 4.1, $\mathbf{E}$ is electric field [V m^{-1}], β_0 is the wavenumber in free space [m^{-1}], ε_r is relative permittivity, σ is effective electric conductivity [S m^{-1}], ω is angular frequency [rad s^{-1}] and ε_0 is the permittivity of free space [F m^{-1}].

2. The time-averaged electromagnetic losses Q_{mw} were calculated using equation 4.2.

$$Q_{mw} = \frac{1}{2}\sigma\|\mathbf{E}\|^2 \tag{4.2}$$

3. The Pennes' bioheat equation was used to compute the temperatures in the simulated space as given in equation 4.3.

$$\rho c \frac{\partial T}{\partial t} = \nabla \cdot k \nabla T + Q_{mw} - m_{bl}c_{bl}(T - T_{bl}) \tag{4.3}$$

In the equation 4.3, ρc is the volumetric heat capacity [J m^{-3} °C^{-1}], T is the temperature [°C], k is the thermal conductivity [W m^{-1} °C^{-1}], m$_{bl}$ is the temperature dependent blood perfusion in the liver tissue and c$_{bl}$ is the specific heat capacity of blood. T_{bl} is the physiologic temperature of the blood. The initial temperature in all tissue regions was set to 37 °C in the whole simulation domain.

4. The Arrhenius model [12] was utilized to estimate the ablation coverage in the tissue following MWA. The Arrhenius model computes the thermal damage as function of time and temperature as shown in equation 4.4.

$$\Omega\ (\tau) = \int_0^\tau A \exp\left(-\frac{E_a}{RT(t)}\right) dt \tag{4.4}$$

In the equation 4.4, $\Omega\ (\tau)$ is the Arrhenius damage parameter, A is the frequency factor $= 5.51$ x 10^{41} [s^{-1}], E_a is the energy barrier $= 2.769$ x 10^5 [J mol^{-1}], R is the gas constant $= 8.3143$ [J mol^{-1} °C^{-1}], $T(t)$ is the spatial temperature profile as a function of time and $\tau =$ total time of the accumulation of thermal damage in the tissue. The values of A and E_a were incorporated to model tissue discoloration following heating and allow a comparison with the experimental ablation zones [199]. For assessing the extent of ablation coverage a damage contour ($\Omega = 1$)

which corresponds to 63% of the completion of thermal damage process, was overlaid on the temperature maps obtained from the simulations.

5. To monitor the safety of the surrounding tissues (i.e. outside 1-3 cm target zone), safety contour was determined using Cumulative Equivalent Minutes at 43°C (CEM43) thermal dose [68]:

$$CEM43 = \int_0^t R^{(43-T)} \, dt \; [\text{min}] \tag{4.5}$$

In the equation 4.5, t is the time for which the tissue was kept at temperature T, R is a compensation factor for 1°C change in temperature which equals 0.5 for $T > 43$ °C and 0.25 for $T \leq 43$ °C. In this study, the extent of the tissue volume where thermal dose exceeded 10 CEM43, was considered as a threshold between reversible and irreversible thermal effects to the tissue.

4.2.2.2 Geometry

The geometry of the model is shown in the Figure 4.3 which includes a MWA applicator and liver tissue. The applicator schematics included only the monopole initially. The balun, dielectric loading and matching network were incorporated sequentially based on the parametric optimization for the required lengths.
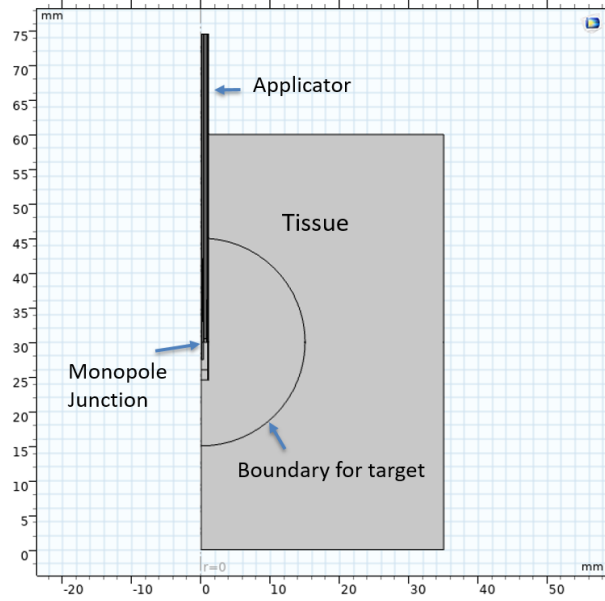
Figure 4.3 Geometry of the model in COMSOL Multiphysics software.

4.2.2.3 Materials

For equations (4.1) and (4.2), tissue dielectric property values within liver tissue were taken from [135] at the applicator's operating frequency 5.8 GHz. For equation (4.3), the thermal tissue properties in tissue domain, and the thermal and dielectric properties of water were taken from [200].

4.2.2.4 Boundary conditions

At the outer boundaries of simulated space, the Sommerfeld radiation condition was applied using the approximations given in equation 4.6:

$$\mathbf{n} \times (\nabla \times \mathbf{E}) - jk\mathbf{n} \times (\mathbf{E} \times \mathbf{n}) = 0, \qquad (4.6)$$

where n is a unit vector perpendicular to the specific boundary.

Furthermore, outer boundaries of the simulated space were subjected to a thermal insulation boundary condition:

$$\mathbf{n} \cdot (k\nabla T) = 0, \qquad\qquad\qquad\qquad (4.7)$$

A convective heat flux boundary condition was applied on the shaft of the applicator to mimic the internal cooling of applicator.

$$q_o = h.\,(T_{ext} - T), \qquad\qquad\qquad\qquad (4.8)$$

where q_o is the modelled heat sink, heat flux coefficient, 'h', was 1000 [W m^{-2} °C^{-1}] and cooling water temperature T_{ext} was 15 °C.

4.2.2.5 Meshing

The overall size of the simulation space was 7 cm × 3.5 cm. The size of mesh elements was optimized by gradually decreasing the mesh size in each domain and monitoring the changes of model output (as defined by maximum temperature around the applicator and ablation size and shape). The largest mesh element sizes (where model output deviations were insignificant with respect to the model with the highest density mesh elements), were chosen to provide a reasonable balance between computational complexity and spatial resolution.

The triangular mesh density was kept highest at the input port, balun and matching network (0.01 mm). The spacing of mesh elements was coarser in other elements of the applicator (0.05 mm). In the tissue, the largest distance between two elements was 3 mm. The total number of mesh elements in the model was around 210,947, the maximum number of degrees of freedom was ~ 1,489,213. The average time to complete one simulation was approximately 45-60 min. The models were run on a system with an Intel(R) Core(TM) i5-4590 CPU operating at 3.3 GHz with a 32 GB RAM.

4.2.2.6 Optimization for radiation pattern and impedance matching

The length of the balun and dielectric loading over the monopole were selected using parametric sweep optimization and monitored for the specific absorption rate pattern in the electromagnetic model at time t = 0 s. The radiation pattern or the specific absorption rate (SAR) were monitored by plotting the electromagnetic heating profile after the first few seconds of heating. The most optimum SAR shapes were obtained for a balun length of 'A' = 6 mm, and dielectric loading of 'B' = 2.5 mm as can be seen in Figure 4.4.
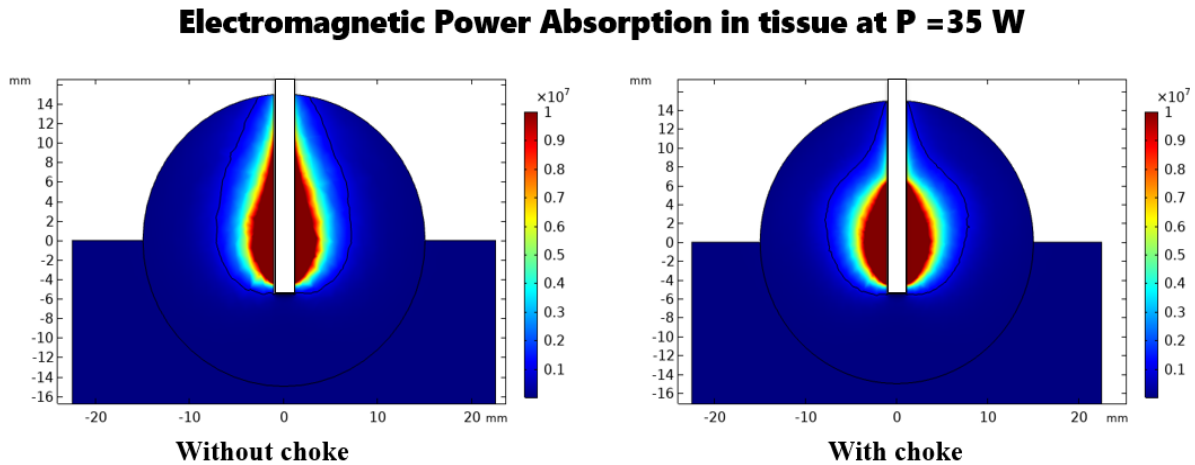
Figure 4.4 Demonstration of optimization of antenna radiation pattern in a 3 cm target.

The length and distance of matching element from monopole were optimized in the simulations using parametric sweep. A matching element length of 'D' = 9 mm at a distance 'C' = 3 mm from the monopole junction improved the matching for the antenna as displayed in Figure 4.5. |S11| before matching was -5.53 dB and |S11| after matching was < -10 dB which provided good antenna return loss (i.e. greater than 90% power transmission to the antenna).
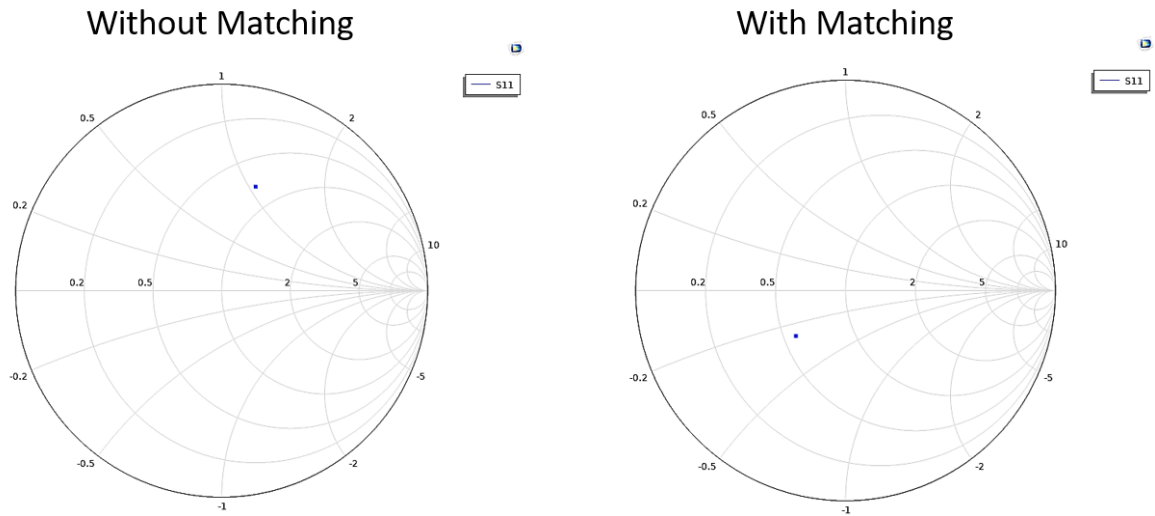
Figure 4.5 Illustration of optimization for impedance matching.

4.2.3 Applicator fabrication

After determining the optimal lengths of balun, dielectric loading of the monopole antenna and matching network using iterative adjustments in simulations, the antenna was fabricated in the lab as described in Appendix C. For an initial prototype, the total length of the UT-34 cable was kept to a few mm more than the length of the applicator in the computer model to allow some margin of fabrication error. The first step was to make the connector over the proximal end of the UT-34 coaxial cable for transmission of microwaves from the feedline cable to the applicator. A hemostasis valve was fixed with epoxy over the proximal end of the applicator shaft (for water flow). After that the dielectric and the outer conductor from the distal end of the UT-34 applicator were taken off according to the dimensions of matching network and monopole length. The matching network was built at a distance from the monopole junction (calculated from the simulations) and was covered with the dielectric and outer conductor. Then the dielectric was placed over the monopole. Next, the balun was created by placing a conductor over the outer

conductor of coaxial cable while leaving an allowance of the inflow of water (described in detail in Appendix C). The antenna was immersed in a beaker filled wither water to measure the broadband reflection coefficients of the antenna with the vector network analyzer (HP 8753D). After confirming adequate impedance matching at 5.8 GHz i.e. |S11| < -10 dB, the water channels were created with outflow and inflow polyimide tubes, valves, and epoxy. Extra care was taken while sealing the applicator at the distal end so that the epoxy stays at least 1-1.5 mm away from the monopole tip. After drying of epoxy, the antenna was tested for water flow and leaks.

Once the applicator performance was tested in ex vivo tissue, another applicator was fabricated with the applicator lengths (at the proximal end) increased to more than 32 cm to fit the hysteroscope working channel. It should be noted that there was no need to change the distal (monopole) end dimensions.

4.2.4 Evaluation of applicator performance in *ex vivo* tissue

Freshly excised bovine liver was obtained from a local slaughterhouse, transported in plastic bags placed over ice packs, for the experimental evaluation of the applicator. 7 cm x 7 cm x 7 cm samples of liver tissue were prepared in the lab, were sealed in a plastic bag and were preheated to physiologic temperatures (~35-37 °C) in a water bath. After warming samples to physiologic temperatures, they were taken out from the plastic bags and placed on a benchtop tray. The applicator was introduced into the sample such that the insertion depth of the applicator (tip of the monopole to the surface of the liver) is at least 6 cm inside the liver sample. A microwave signal generator (HP 83752B) was used to provide a continuous wave sinusoidal signal at the 5.8 GHz frequency. To amplify the signal to desired power (15 W to 35 W) solid-state microwave amplifiers were used. A microwave power meter (Bird 7022, statistical power sensor) was
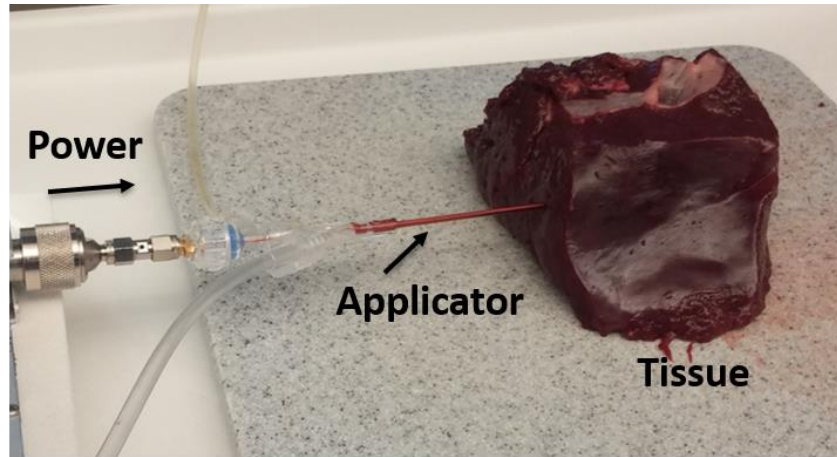
Figure 4.6 Setup for applicator evaluation in *ex vivo* bovine liver tissue sample

employed to monitor forward and reflected power during ablations. Cooled water (~15 °C) was

circulated through the applicator through a peristaltic pump (Cole Parmer 7554–90, Vernon Hills,

IL, USA) at a rate of 80 [ml min^{-1}]. A total of 9 experiments were performed with 3 sets of

experiments for each target zone (i.e. to create ablations in 1 cm, 2 cm and 3 cm target zone). The

experimental setup is shown in Figure 4.6.

4.2.5 Evaluation of applicator performance in tissue mimicking gel phantom

4.2.5.1 Preparation of thermo-chromic tissue mimicking gel phantom

Thermo-chromic phantoms provide a facile means for visualizing spatial heating patterns

from candidate ablation technologies under test. Polyacrylamide based thermo-chromic tissue

mimicking gel phantoms have been previously employed for several HIFU, RFA and MWA

applications [182], [184] [179]. To prepare thermo-chromic tissue mimicking gel phantom in this

study, the formulation was taken from [184]. Briefly, the phantom was prepared using

polyacrylamide gel and thermo-chromic ink which gradually and permanently changes its color at

ablative temperatures (~ 60 ºC). The ingredients of the gel phantom and their respective

proportions are enlisted in Table 4.1. First, a mixture of aqueous solution of 40% (w/v)

acrylamide/bis-acrylamide (with feed ratio of 19:1), deionized water, sodium chloride and thermo-chromic ink (Kromagen WB flexo ink magenta K60, LCR Hallcrest, LLC, Glenview) was formed in a glass beaker at room temperature (~23 ℃) using magnetic stirrer. After thorough mixing of the aforementioned ingredients, Ammonium persulfate (APS) was added to initiate polymerization and N, N, N′, N′-tetramethylethylenediamine (TEMED) was added as a catalyst for polymerization of the gel. Acrylamide/Bis-acrylamide, APS and TEMED were purchased from Sigma Aldrich, Milwaukee, WI.

The final solution was instantaneously transferred to the 4 mL glass vials and plastic containers of required gel dimensions, sealed and placed in a refrigerator (at 4 ℃) to allow slow polymerization. Otherwise, if the polymerization happens at room temperature, the temperature of phantom material rises due to the heat generated in the polymerization process [201] which will result in undesired and confounding color changes. The phantom was kept in the refrigerator until use. Figure 4.7 displays a block of gel phantom at room temperature (~ 23 ℃) which was prepared for testing the MWA applicator.

Table 4.1 Formulation of thermo-chromic tissue mimicking gel phantom

Sr. No	Ingredients	Proportions (%)
1.	40% (w/v) acrylamide/bis-acrylamide (19:1)	17.5 (v/v)
2.	Kromagen WB flexo ink magenta K60	5 (v/v)
3.	APS	0.14 (w/v)
4.	TEMED	0.14 (v/v)
5.	Sodium chloride (NaCl)	0.9 (w/v)
6.	Deionized water	76.1 (v/v)

Figure 4.7 A block of thermochromic tissue mimicking gel phantom at room temperature.

4.2.5.2 Assessment of gel discoloration with temperature

The gel samples were heated at specific temperatures in a water bath for different time durations from 5-30 min. The thermo-chromic gel permanently changes its color according to the maximum heating temperature it has been exposed and is not sensitive to the duration of heating, in agreement with previous studies [184].

Figure 4.8 An example set of gel phantom illustrating gel discoloration from its room temperature value (25 ºC) at different peak temperature values.

Next the gel samples which were heated to specific temperatures, were placed in a portable Mini Photo Studio Box (SANOTO, Whittier, CA). A 12 megapixel Samsung Galaxy S7 camera was used to capture the images in consistent background lighting conditions. Figure 4.8 displays the gel discoloration at respective maximum temperature values. It can be seen in the figure that noticeable color changes occur after 50 ℃. Moreover, the gel samples were heated beyond 75 ℃ but the color remains the same as that of 75 ℃.

4.2.5.3 Determination of RGB values and thresholds

To determine the RGB value evolution with the rising temperature, following procedure was employed. A custom made tool in MATLAB was utilized to perform color correction (based on white background color correction algorithm) and to collect the RGB values at the specific chosen points, selected to avoid the lighting artifacts due to reflection from the surface of glass vials, as illustrated in Figure 4.9. This procedure was repeated for each temperature set point (i.e. 6 temperatures and 7 sets, a total of 42 samples). The RGB value at each point was noted as the average over 3x3 pixels in region of interest.

Figure 4.9 Sample sets displayed as an example to demonstrate the color change as a function of temperature from 50-75 ℃ after white correction. Each set was comprised of 6 samples of phantom which were heated at constant temperatures of 50 ℃, 55 ℃, 60 ℃, 65 ℃, 70 ℃ and 75 ℃. The red circles show the points taken for extracting the RGB values.
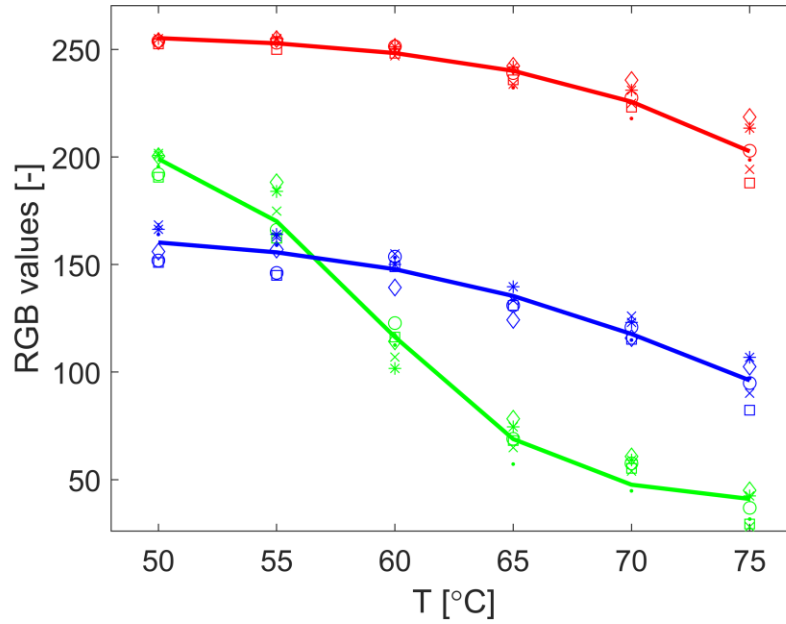
Figure 4.10 RGB values as a function of temperature obtained from 7 experimental sets. Sigmoid function was used for parametric fitting of values of each color channel at temperatures ranging from 50-75 ℃.

RGB values at temperatures ranging from 50-75 ℃ were consequently fitted with a sigmoid function at each of the color channels independently by nonlinear least squares iterative method as shown in Figure 4.10.

The sigmoid function for each channel was calculated using equation 4.9.

$$\text{Thr\_channel (T)} = \frac{a_1}{1 + \exp((T - a_2)/a_3)} + a_4 \tag{4.9}$$

Where Thr_channel is the threshold for each channel at a specific temperature value 'T'. T ranges from 50-75 ℃. a_1, a_2, a_3 and a_4 are the fitting coefficients which are provided in Table 4.2.

Table 4.2 Fitting coefficients for sigmoid functions of RGB channels from 50-75 ℃.

Channels	Fitting coefficients			
	a_1	a_2	a_3	a_4
R channel	110.8139	76.1119	5.7726	145.5464
G channel	167.5746	59.2952	3.4657	41.1028
B channel	81.5766	69.0852	5.4209	76.9208

4.2.5.4 Measurement of dielectric properties

The properties of the tissue mimicking gel phantom were required for the computer simulations to compare with the experiments. The dielectric properties of the gel phantom were measured using the open-ended coaxial probe method (similar to measurements reported in Chapter 3) [202]. KeySight 85070E probe was utilized to measure broadband complex reflection coefficient with the use of Vector Network Analyzer (VNA) (HP8753D). For minimizing the measurement error, the gel sample has to be greater than 1 cm in diameter. We also utilized the hot plate and custom copper template to heat the tissue sample up to ablative temperatures. Finally, fiber optic sensor (Neoptix™ Inc., Quebec CA) was used to monitor and save the temperature concurrently with dielectric measurements as shown in Figure 4.11.
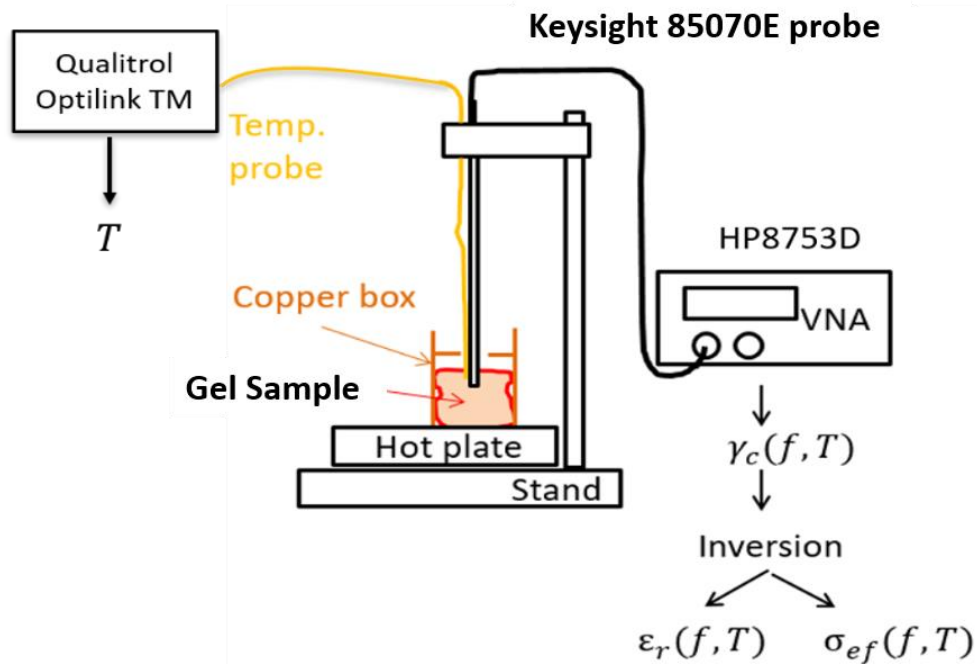
Figure 4.11 Schematics illustrating the measurement setup of gel dielectric properties.

The dielectric properties were measured on 8 gel samples with multiple measurements on each sample (total 38 readings on room temperature and 1 reading on elevated temperature 'T' ranging from 22 ℃ to 100 ℃). The temperature dependent dielectric data collected from these experiments (shown in Figure 4.12) was used in computer models. The fitting coefficients for the dielectric properties of gel phantom are given in Appendix D.
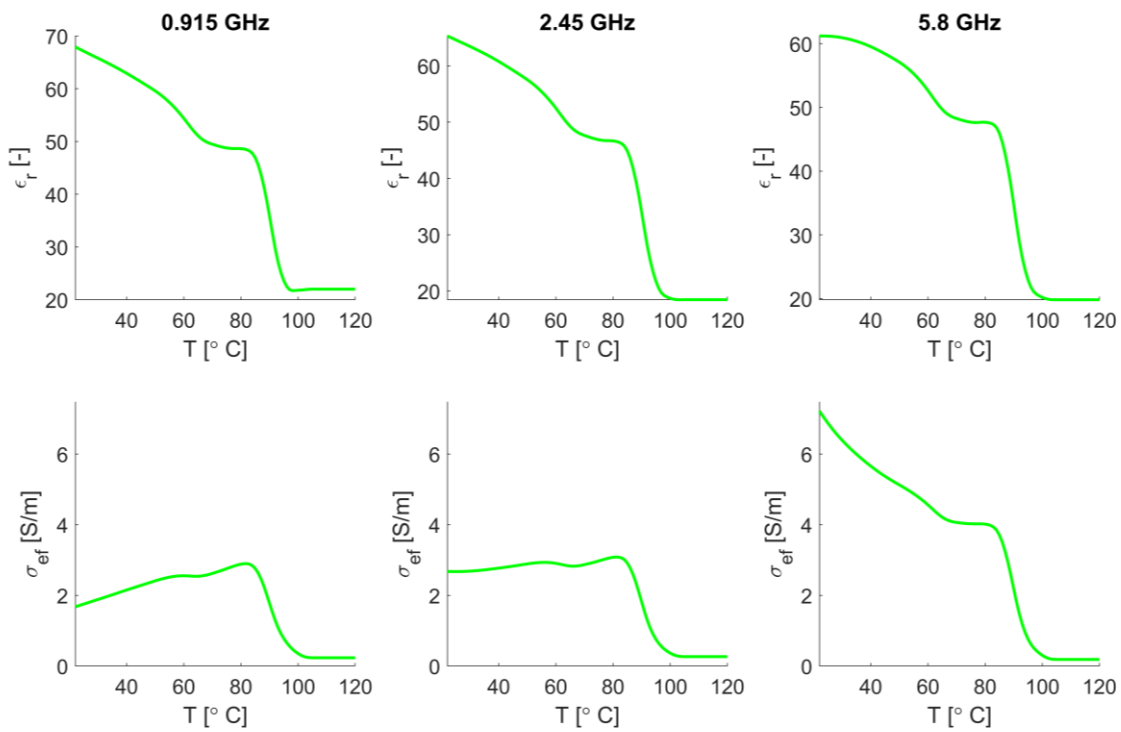
Figure 4.12 Temperature dependent dielectric properties (relative permittivity, ε_r, and effective conductivity, σ_{eff}) of gel phantom at 915 MHz, 2.45 GHz and 5.8 GHz.

4.2.5.5 Measurement of thermal properties

Thermal properties of the tissue mimicking gel phantom were measured with thermal measurement equipment (SH3 Thermal Probe, Tempos Data hub) employing Dual Needle Algorithm [203]. One needle is used for heating the tissue while the other one serves for temperature gradient measurement. The instrument reports volumetric heat capacity (c [MJ m^{-3} K^{-1}]), thermal conductivity (k [W m^{-1} K^{-1}]), thermal diffusivity (d [mm^2 s^{-1}]) and thermal resistivity (r [°C cm W^{-1}]) from the measured data. Measured data are acquired during the heating as well as cooling phase of reading. Figure 4.13 shows the experimental setup for measuring the thermal
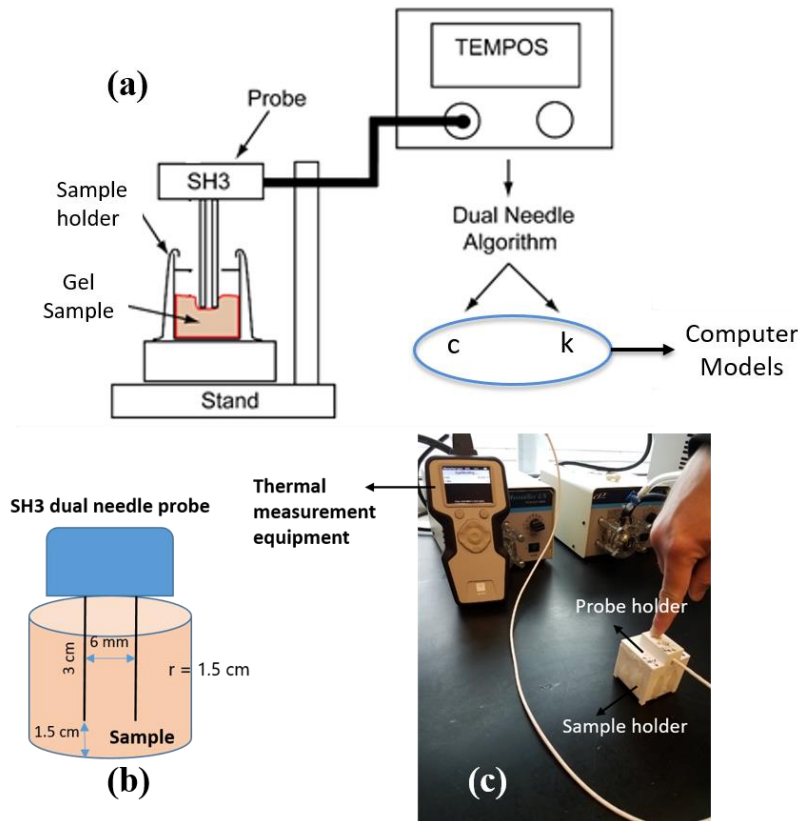
Figure 4.13 Measurement setup for thermal properties of gel phantom. (a) Schematics of the measuring setup, (b) The required sample dimensions for SH3 dual needle probe, and (c) Actual measurement setup with thermal measuring equipment with gel sample inside the custom designed sample holder based on the measuring equipment datasheet requirements.

properties of the gel samples. Gel samples of dimensions 3 x 3 x 4 cm are required to minimize the measurement error as mentioned in the datasheet of the measuring equipment.

Thermal properties of 7 samples were measured (total 16 measurements) at room temperature ~22-23 ºC. The thermal properties of the phantom compare well with the values reported in previous studies [182] and are summarized in

Table 4.3.

Table 4.3 Thermal properties of tissue mimicking gel phantoms.

Properties	Measured values at room temperature			
	Mean	Std	Min	Max
k [W m^{-1} K^{-1}]	0.51	0.07	0.48	0.61
r [°C cm W^{-1}]	197.56	24.6	165.1	230.5
c [MJ m^{-3} K^{-1}]	3.31	0.41	2.62	3.81
d [mm² s^{-1}]	0.15	5 x 10^{-3}	0.15	0.17

4.2.5.6 Experimental assessment of applicator in gel phantom

6 cm x 6 cm x 6 cm samples of gel phantom were prepared in the lab and refrigerated. For ablation experiments, the phantoms were taken out of the refrigerator and was left on the benchtop to stabilize the temperature of the gel to room temperature (23 °C). The gel was transferred to a custom designed template box which has slots for proper insertion of applicator as well as a matrix of holes for the placement of fiber optic sensors. The applicator was introduced into the sample such that the insertion depth of the applicator (tip of the monopole to the surface of the phantom) is atleast 4 cm inside the gel sample. The fiber optic sensors (Neoptix™ Inc., Quebec CA) were placed inside the gel from the opposite end of the applicator at 5 mm, 5 mm and 10 mm (radial distance from the applicator shaft) using 14 G MILA needle catheters to ensure a straight trajectory at the target location i.e. in line with the monopole junction. Microwave signal generator (HP 83752B) was used to provide a continuous wave sinusoidal signal at the 5.8 GHz frequency. To

amplify the signal to desired power (25 W) solid-state microwave amplifiers were used. A microwave power meter (Bird 7022, statistical power sensor) was employed to monitor forward and reflected power during ablations. Room temperature water (~23 °C) was circulated through the applicator through a peristaltic pump (Cole Parmer 7554–90, Vernon Hills, IL, USA) at a rate of 80 [ml min^{-1}]. A total of 2 experiments were performed with 3 temperature sensors in each experiment for measuring the temperatures in the expected heating zones to compare the temperatures predicted in the simulations each target zone. The duration of first heating experiment was 3 min and for second heating experiment was 8 min. Since the gel material easily disintegrates with the use of knife while slicing, the gel phantom was carefully sliced using copper sheet post ablation. The experimental setup is shown in Figure 4.14.
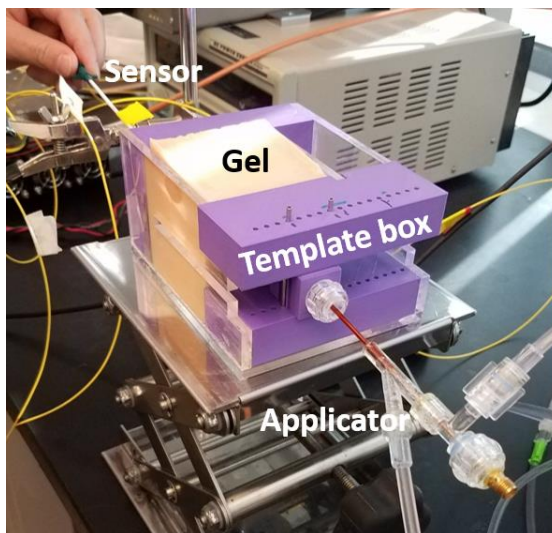
(a)　　　　　　　　　　　　　　　　　(b)

Figure 4.14 (a) Setup for applicator evaluation in tissue mimicking gel phantom, (b) post ablation slicing of the gel.

The images of the gel post microwave heating were taken using the same procedure as discussed in previous sections and the white correction was applied. Using the RGB thresholds from the sigmoid function, the segmentation of the images obtained from ablation was performed at specific temperature values i.e. 55 ℃, 60 ℃ and 70 ℃. The following expression was used for image segmentation.

$$(\text{Image R channel } (x, y) < \text{Thr \_ R } (T))$$

$$\&$$

$$(\text{Image G channel } (x, y) < \text{Thr \_ G } (T))$$

$$\&$$

$$(\text{Image B channel } (x, y) < \text{Thr \_ B } (T))$$

where Thr _ R = threshold of R channel,

Thr _ G = threshold of G channel and

Thr _ B = threshold of B channel at a specific temperature, T.

Moreover, the measured temperature at the fiber optic sensor location was compared with the temperature contours obtained in the images for that specific temperature value to verify the agreement of the gel discoloration due to microwave heating with gel discoloration-temperature mapping obtained from water bath heating.

4.2.5.7 Computer simulations of applicator in gel phantom

Similar models were used for the computer simulations of applicator in gel phantom as were used for the simulations in ex vivo tissue except the tissue medium was replaced by the gel material. The measured temperature dependent dielectric properties and thermal properties of the gel phantom were incorporated in the models. The models were simulated with room temperature values of thermal properties of gel and temperature dependence of thermal properties of *ex vivo* tissues since it was hypothesized that the gel's thermal properties would be similar to the *ex vivo* tissues. The models were simulated according to the power and time used in the gel experiments i.e. 25 W, 3 min and 8 min respectively. The ablation profiles and the temperatures recorded at the actual sensor location (verified after slicing) were compared with the simulation results. Three values of rate of change of thermal conductivity (dk) were simulated (0.024, 0.0031 and 0.038 [W m^{-1} K^{-1}]) to predict the simulation results which would provide the best match with the experimental results.

4.3 Results

4.3.1 Applicator fabrication

Figure 4.15 displays the fabricated 5.8 GHz water-cooled monopole applicators with water channels, coaxial cable connector for power input from the microwave generator and heating tip for creating ablations in 1-3 cm target zones.
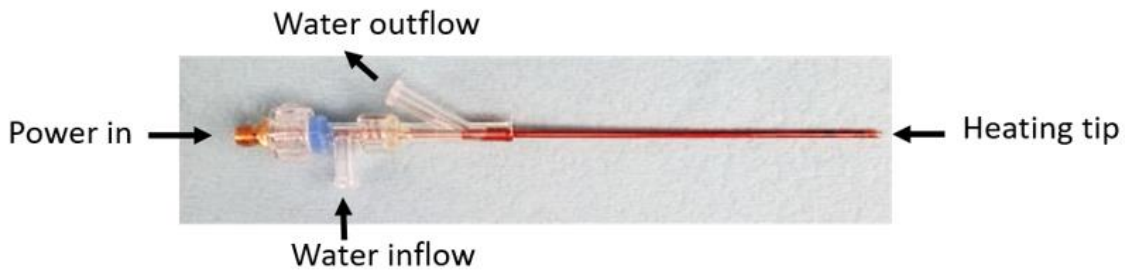
(a)

(b)
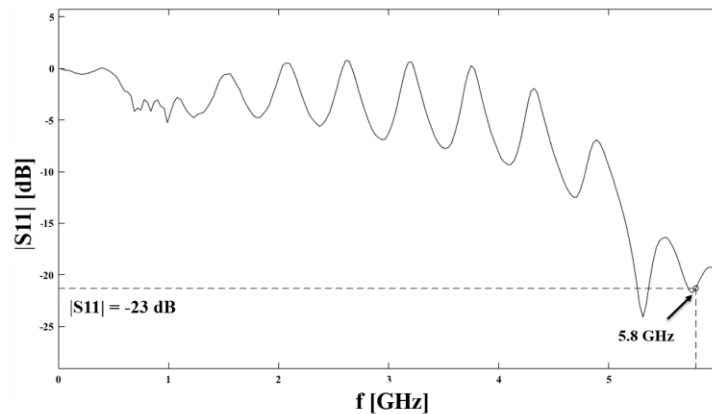
Figure 4.15 Fabricated 5.8 GHz water-cooled monopole applicators (a) prototype design, (b) design compatible with hysteroscope length, and c) Measured |S11| of fabricated antenna in water.

4.3.2 Evaluation of applicator performance in *ex vivo* tissue

Figure 4.16 displays the ablation zones created in 1-3 cm diameter targets. It can be seen in the figure that the applicator is able to create almost spherical ablation zones within 1-3 cm diameter targets.

15 W, 3 min	30 W, 5 min	35 W, 10 min
0.9 cm x 1.0 cm x 1.0 cm	1.8 cm x 2.0 cm x 2.0 cm	2.5 cm x 2.7 cm x 2.7 cm
1 cm target	**2 cm target**	**3 cm target**
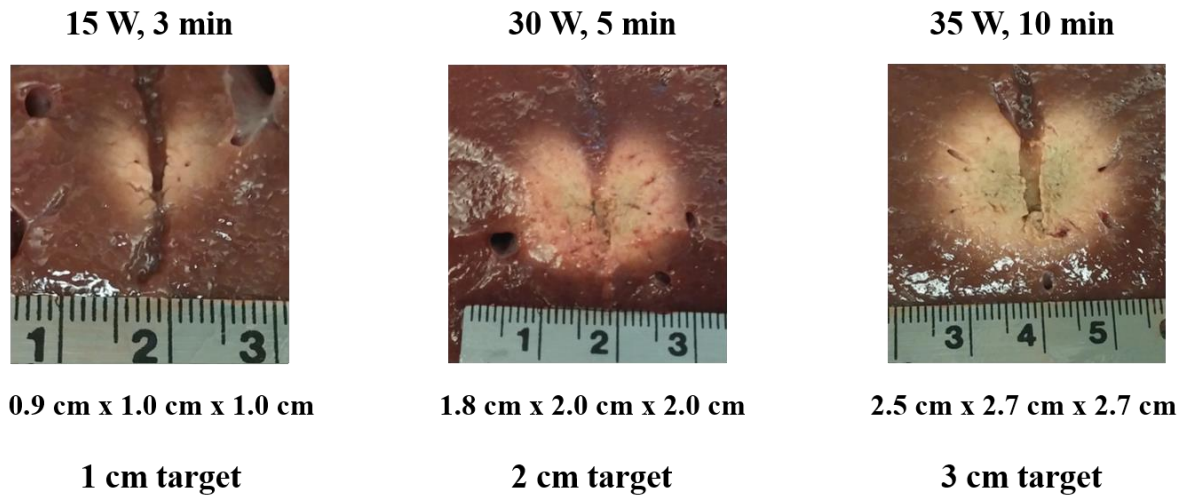
Figure 4.16 Example images from the experimental evaluation of 5.8 GHz applicator in *ex vivo* tissue for creating ablations in 1-3 cm target zones with their respective power and time combinations.

Figure 4.17 shows comparison of the computer model simulations and the ablation zones obtained from the experiments.

Table 4.4 provides a detailed analysis to quantify the differences between the experimental results and the simulations. It can be seen that the ablation boundaries from experiments lie within ±1.5 mm of simulation predictions.
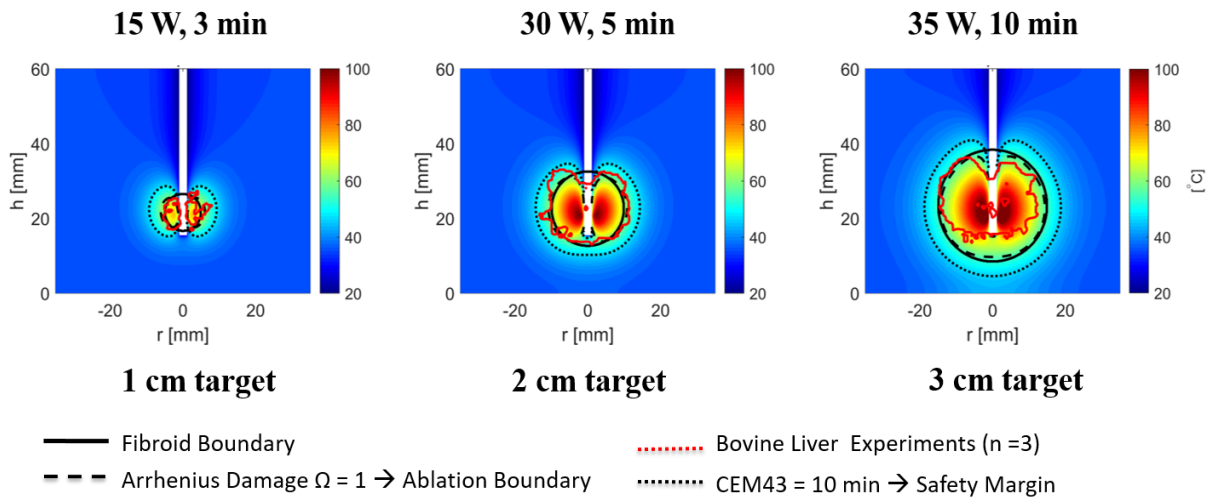
Figure 4.17 Comparison of ablation profiles from experiments and simulations. For each fibroid size, mean values of the ablation contour obtained from the experimental results (n = 3 experiments) is overlaid on the temperature maps from simulations.

Table 4.4 Comparison of ablation sizes achieved in simulation and experiments.

Desired Ablation Size (cm)	Power (W)	Time (min)	Ablation						
			Height (cm)			Width (cm)			
			Simulation	Experiments	Diff.	Simulation	Experiments		Diff.
					μ±σ				μ±σ	
1 cm	15	3	0.80	0.9	0.86	0.06	1.20	1.0	1.0	0.20
				0.8	±	±		1.0	±	±
				0.9	0.06	0.06		1.0	0.0	0.0
2 cm	30	5	1.70	1.8	1.80	0.10	2.20	2.0	1.96	0.24
				1.9	±	±		2.0	±	±
				1.7	0.10	0.10		1.9	0.06	0.06
3 cm	35	10	2.40	2.5	2.46	0.06	2.70	2.7	2.67	0.03
				2.5	±	±		2.7	±	±
				2.4	0.06	0.06		2.6	0.06	0.06

Figure 4.18 shows the radial fall-off of temperature profile while using 5.8 GHz applicator from 55 ℃ (ablated zone) to 43 ℃ (thermally affected zone).
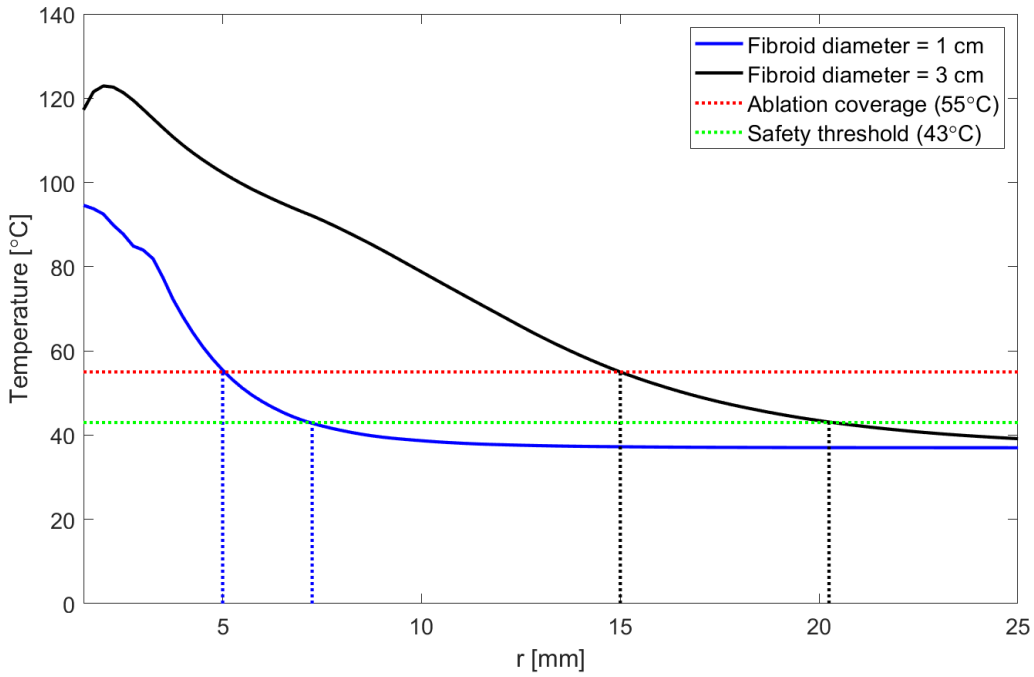
Figure 4.18 The radial temperature profile of 5.8 GHz MWA applicator (from the applicator surface) with 60 W applied power for 1-3 cm target zones at (10 s and 564 s) of ablation in an *ex vivo* tissue illustrating a gradual decay from 55 ℃ (ablated zone) to 43 ℃ (thermally affected zone) i.e. 2 mm for 1 cm fibroid and 5 mm for 3 cm fibroid.

4.3.3 Evaluation of applicator performance in tissue mimicking gel phantom

Figure 4.19 shows achieved discoloration profiles in gel phantom after heating at 25 W for 3 and 8 min and illustrates the thermal spread by three contours of areas with temperatures which is higher than the given thresholds (i.e. 55 ^{o}C, 60 ^{o}C and 70 ^{o}C).
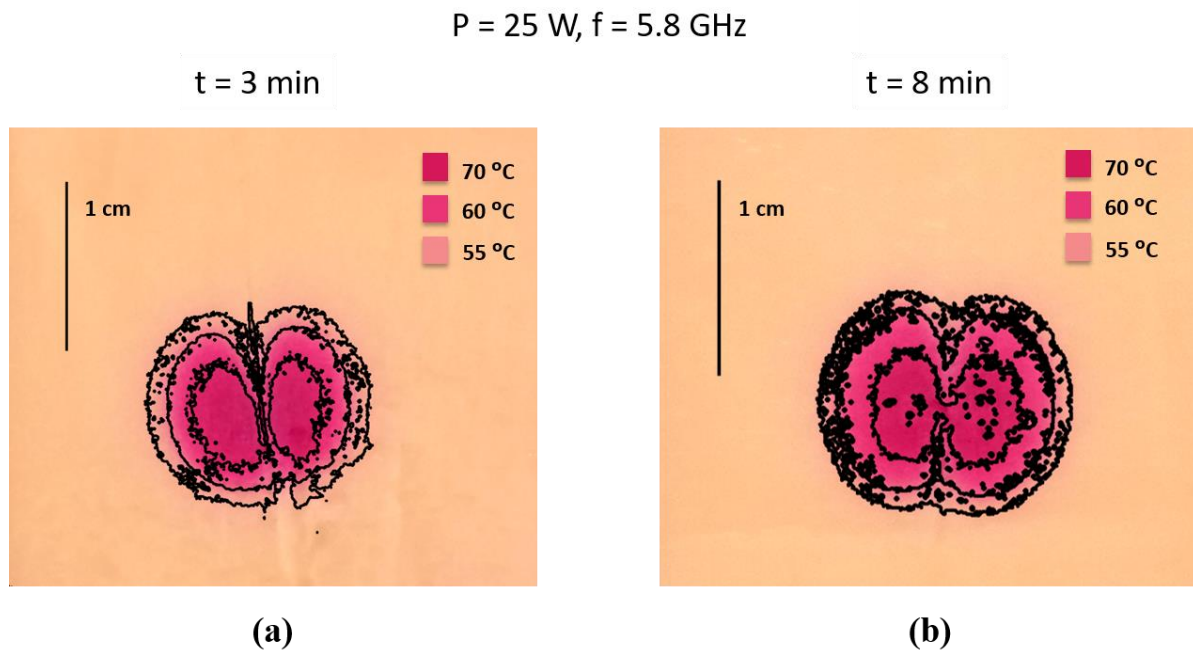
Figure 4.19 Ablation profile of 5.8 GHz MWA applicator obtained from experiments in tissue mimicking thermo-chromic gel phantom with overlaid temperature contours calculated from the sigmoid function of RGB values of gel discoloration experiment. (a) 1.3 cm ablation obtained with applied power 25 W for 3 min duration and (b) 1.3 cm ablation obtained with applied power 25 W for 8 min duration where 55 ^{o}C contour is considered ablation boundary.

The 55 °C contour obtained from experiments is furthermore compared with the extent of

55 °C from simulation in Figure 4.20.
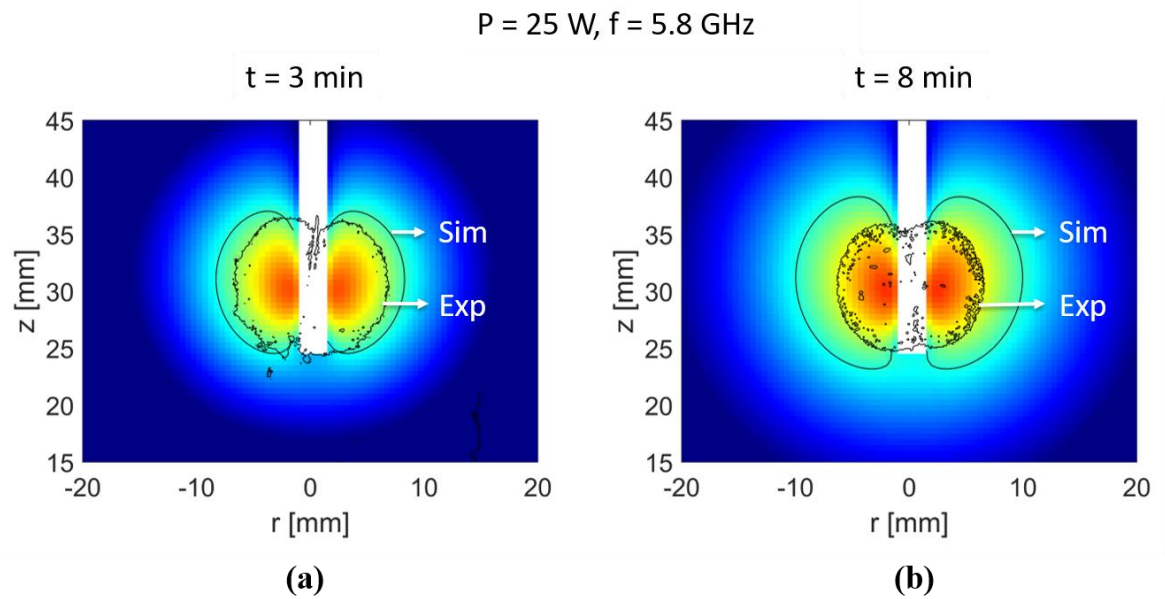
Figure 4.20 Ablation profile of 5.8 GHz MWA applicator obtained from simulations in tissue mimicking thermo-chromic gel phantom properties after optimization of thermal properties (a) 1.3 cm ablation in experiments vs 1.6 cm ablation in simulations with 25 W for 3 min heating and (b) 1.3 cm ablation in experiments vs 1.9 cm ablation in simulations with 25 W for 8 min heating where 55 ºC contour is considered ablation boundary.

Furthermore, to verify the extent of color change with respect to maximum achieved measured temperature obtained after microwave heating and its comparison to colors achieved in water bath heating as mentioned in section 4.2.5.3, the set of experiments with fiber optic sensors which were placed in known locations was conducted.

Table 4.5 shows the intended and actual locations of fiber optic sensor tip as measured after the heating experiments.

Table 4.5 shows the fiber optic temperature sensor intended and measured locations in space (x, y, z) and the maximum temperatures recorded at each sensor at the specific sensor position.

Sensor	Fiber optic sensor location in gel from the applicator shaft		Maximum temperature recorded (°C)
	While setting up in template box (x, y, z) (mm)	After slicing (x, y, z) (mm)	
S1	(10, 0, 0)	(8, ±1 , 0)	38.8
S2	(5, 0, 0)	(8, ±1, 0)	42.3
S3	(5, 0, 0)	(2, ±1, 0)	88.5
S4	(10, 0, 0)	(11, ±1, 3)	37.9
S5	(5, 0, 0)	(5, ±1 , 4)	52.0
S6	(5, 0, 0)	(4, ±1 , 3)	64.0

The sensitivity of agreement between measured temperatures from S3 and temperatures from simulations with regards to sensor displacement (from measured position) is illustrated in Figure 4.21 where root mean square error (RMSE) for each displacement is provided.
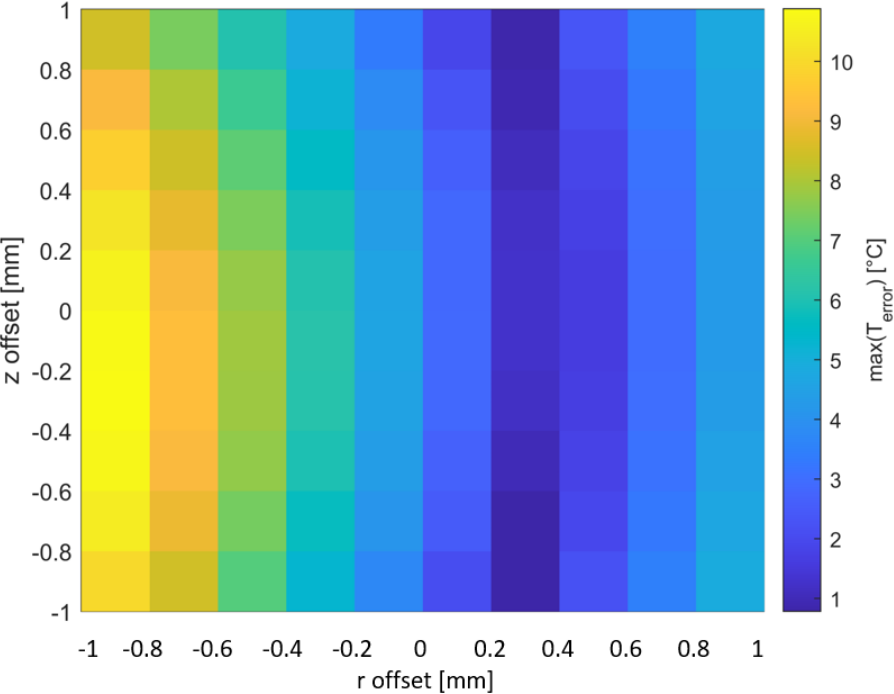
Figure 4.21 Sensitivity of agreement between simulated temperature and temperature from S3 (as assessed by RMSE) with respect to sensor displacement.

Figure 4.22 demonstrates the agreement between measured maximum temperatures from fiber optic sensors and corresponding color thresholds as predicted by the RGB sigmoid functions for given maximum temperatures.
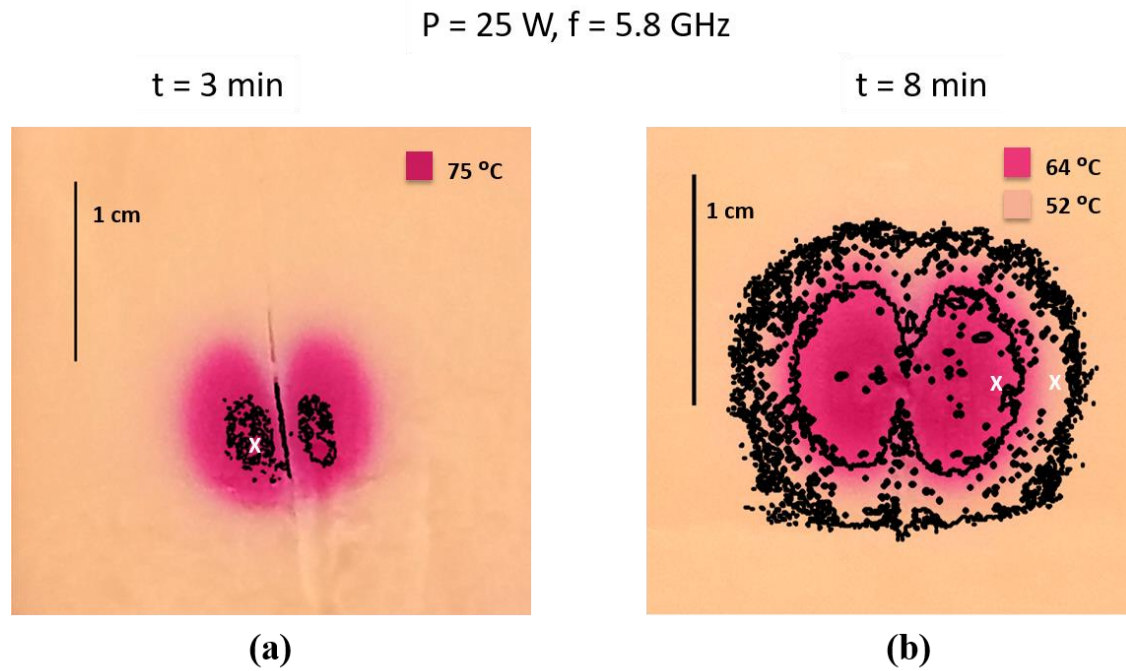
Figure 4.22 Validation of maximum temperature as predicted by achieved discoloration and as measured from the fiber optic sensors (a) Contour of maximum temperature recorded at S3 overlaid on the discoloration profile (obtained from P= 25 W and 3 min heating experiment) and (b) Contours of maximum temperature recorded at S5 and S6 overlaid on the discoloration profile (obtained from P = 25 W and 8 min heating experiment). The 'X' marks show the location of sensor tip.

Figure 4.23 shows temperature profiles achieved at respective fiber optic sensing points in comparison with the predicted temperatures from simulations at measured locations as well as temperatures at locations with lowest RMSE during the first 30 s of simulations.
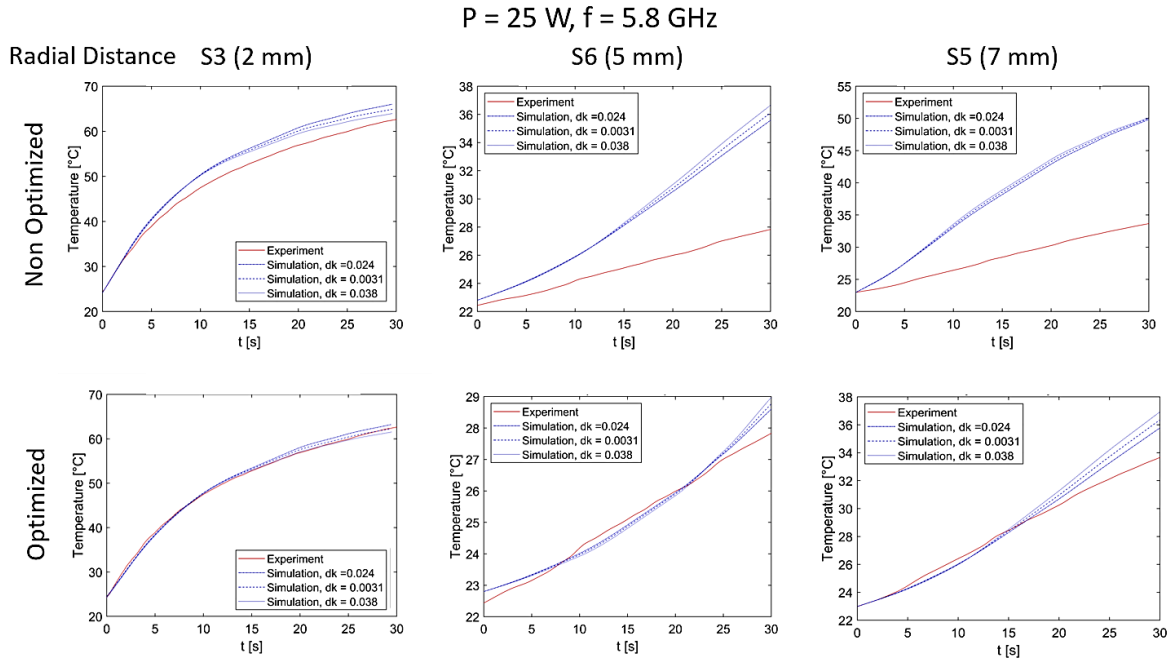
Figure 4.23 Temperatures around applicator shaft in the gel in first 30 s of heating for SAR prediction. Temperatures from simulations are plotted vs temperatures at measured sensor locations (2 mm, 5 mm and 7 mm) from the applicator shaft and at optimized locations (within ± 1 mm of measured location) with lowest RMSE value.

4.4 Discussion

In this study, the design of 5.8 GHz water-cooled monopole MWA applicators suitable for ablation of 1-3 cm uterine fibroids was reported. The presented applicator designs were evaluated in thermo-chromic tissue-mimicking phantoms and ex vivo tissue.

Figure 4.16, Figure 4.17 and Table 4.4 confirm that the experimental results of 1 cm, 2 cm and 3 cm ablations in ex vivo tissue samples are in good agreement with the predicted results of simulation. Since the thermal dose safety margins cannot be assessed in experiments (without temperature sensors), validated computer simulations can be used to predict the thermal safety margins as 10 CEM43 has been plotted as an example of thermal safety contour in Figure 4.17.

Before designing the 5.8 GHz MWA applicator, it was hypothesized that a spherical ablation zone can be achieved as compared to the previous applicator designs at 2.45 GHz which provided elliptical ablation zones. Figure 4.18 shows the radial margin from ablated to non-ablated region using 5.8 GHz applicator to be ~2-5 mm for 1 cm and 3 cm target zones. To achieve spherical ablation profiles while using 2.45 GHz, we applied the same applicator design concepts as presented in this dissertation for 2.45 GHz monopole applicator. For a required length of monopole i.e. 2.5 mm for 1 cm fibroid ablation, at best we could achieve $|S11| = -4.72$ dB. For an efficient power transfer from antenna to the target tissue $|S11| < -10$ dB is desirable. Hence, the use of a 2.45 GHz applicator is ill-suited to achieve ablation volumes with minimal damage to surrounding tissues in small sized fibroids (i.e. 1- 3 cm).

Figure 4.19 illustrates that the extent of ablation contour (55 ºC) obtained in gel experiments for applied power of 25 W is unaffected by the increase in the heating duration. For both 3 min and 8 min ablation, the extent of ablation remains constant (i.e. 1.3 cm). Since the same applicator was used in the *ex vivo* tissue experiments which provided promising results for

106

ablations in 1-3 cm target zones hence this observation is most likely to the discrepancy between physical properties of the gel phantoms and the properties used within simulations. While temperature-dependent dielectric properties of the phantoms were measured and used within simulations, thermal properties were only measured at room temperature. Further studies are needed to evaluate the temperature dependent thermal properties of the phantoms.

To validate the simulation with the experiments, 55 ℃ ablation contours from experiments were overlaid on the temperature maps obtained from simulations in Figure 4.20. It can be seen that the ablation contours in experiments are consistently smaller than the simulation predicted contours in both experiments conducted on 3 min and 8 min with 25 W applied power.

To validate the ability of simulation to predict SAR around the applicator shaft in the gel, the temperature profiles in first 30 s from sensors as well as simulations were compared in Figure 4.23. There are two known sources of variability between experiments and simulations. 1) The accuracy of fiber optic sensor tip location is within ±1 mm and 2) The temperature dependence of the gel's thermal properties is unknown and the temperature dependence of *ex vivo* tissue thermal conductivity was utilized in the gel models. Sensitivity analysis with ±1 mm sensor position offsets from the measured sensor location in experiments for sensor S3. The simulation temperatures were fitted to the experimental temperatures with the sensitivity to measured sensor locations (2 mm, 5 mm and 7 mm from the applicator shaft) and rate of change of thermal conductivity, dk. It was observed that the simulations with the highest dk, i.e. 0.038 [W m^{-1} K^{-1}] has a better match with the experimental results as compared to lower values of dk. The first 30 s of experiments were fitted with the simulation temperatures, the temperature profiles observed in experiments are consistently lower than the simulations after 30 s suggesting that the temperature dependence functions of thermal properties of the gel are considerably different from the *ex vivo* tissue.

Figure 4.24 confirms a good agreement between measured maximum temperatures from fiber optic sensors; S3, S5 and S6 (in microwave heating experiments) and corresponding color thresholds (predicted by sigmoid functions obtained from water bath heating experiments) by aligning contour boundary location with the distance of the fiber optic sensor from applicator shaft. The maximum measured temperature value at temperature sensor S3 (located at 2 mm radial distance from the applicator shaft) was 88.5 ºC. However, it was observed in the water bath gel heating experiments that the gel color remains the same at temperatures > 75 ºC, therefore 75 ºC contour was plotted and the location of S3 lies well within the contour.

Thermo-chromic tissue mimicking gel phantom experiments reveals some interesting observations about the gels. Firstly, the changes in gel color are independent of the cumulative thermal dose accumulated as a result of different heating durations from 5-30 min at temperatures ranging from 50 -75 ºC as described in earlier studies [184]. However, the thermal therapies in biological tissues are dependent on the cumulative thermal dose of heating (i.e. time-temperature history) [204]. Secondly, it was concluded the temperature dependence of the thermal properties of the gel phantom is not similar to the biological tissues. Further studies are needed to investigate the thermal properties of the gel phantom at elevated temperatures which may explain the differences seen in the experimental and simulated results.

4.4 Conclusion

5.8 GHz water cooled monopole MWA applicators designed for transcervical microwave ablation of fibroids via hysteroscopy yields more than 90% ablation volumes inside the target zones (1-3 cm) with minimal damage to the non-target tissue. Thermo-chromic tissue mimicking gel phantoms can be used for the quantitative assessment of different microwave applicators i.e. the shape of the SAR. However, for the quantitative assessments the computer simulations should match with the experimental results. More studies are needed to characterize the thermal properties of the gel phantom at elevated temperatures.

Chapter 5 - Assessment of device positioning and tissue dielectric properties on ablation outcome in Transcervical Microwave Ablation of Fibroids[2]

5.1 Introduction

Uterine leiomyoma (fibroids) are a common benign tumor which significantly decrease the quality of a woman's life, and are estimated to affect 77% of all women by menopause [2]. In the United States alone, it is estimated that 11 million women have fibroids [205]. Symptoms include heavy menstrual bleeding, increased pelvic pressure, chronic pain, infertility, and miscarriages. Fibroids are classified based on the anatomical location of the fibroid within the uterus wall (myometrium), and range between Types 1 – 8. [15].

The type, size and location of fibroid inside the uterine cavity affects the treatment modalities offered to the patient [15] [16] [75]. Hysterectomy, surgical removal of the entire uterus, is an established treatment for fibroids. However, this is a highly invasive procedure, is associated with long recovery times, and precludes child-bearing. Uterine artery embolization [206] and myomectomy [25] are minimally-invasive treatments that offer the potential to preserve fertility. *In situ* thermal ablation techniques for the treatment of fibroids – such as high intensity focused ultrasound (HIFU) [207], radiofrequency ablation (RFA) [98] [208] and microwave ablation (MWA) [41], [48] – are desirable due to their low invasiveness and associated fast recovery rates. Regardless of the modality of ablation utilized, the clinical goal is to maximize the volume of

---

fibroid, which is heated to ablative temperatures ($> 55 – 60°C$ [37]), while limiting thermal spread to the surrounding uterine tissue. The volume of ablated tissue can be assessed post-ablation (e.g. on magnetic resonance imaging) with the non-perfused volume (NPV) [147], which has been shown to be an indicator for symptom relief [43].

Hysteroscopic myomectomy offers a safe and effective treatment for submucosal fibroids (Type 0 and 1) [209] where the fraction of the fibroid protruding into the uterine cavity exceeds 60%. However, hysteroscopic myomectomy becomes challenging for the complete resection of Type 2 ($\geq 50\%$ intramural component) fibroids [33] [34] [35] [36]. Multiple procedures can cause perforations, collateral damage to healthy myometrium tissue [25][99] or intrauterine adhesions [210][31], which can adversely affect the reproductive health of the patient. For the treatment of small fibroids (≤ 3 cm diameter), non-surgical or minimally invasive procedures are often preferred [209]. While HIFU can be delivered noninvasively, it imposes requirements of additional imaging to verify accurate localization of the ablative energy during the procedure, and additional hardware and control algorithms for steering the focal point such that a sufficiently large ablation volume is achieved, which can be time consuming and expensive.

RFA and MWA procedures are delivered with an applicator that is positioned within the fibroid. RFA systems designed specifically for ablation of fibroids are in clinical use employing laparoscopic [20] [75] and ultrasound guided (US) transcervical approaches [37] [40]. RFA systems have been applied towards treating all types of fibroids except Type 0, for which hysterscopic myomectomy is preferred. US guided percutaneous MWA using a 2.45 GHz system has also been reported in the clinical setting [10] [11]. While the volume of fibroids following ablation was significantly smaller, no complications and reduced procedure-related pain compared to other modalities were reported. The use of a transcervical microwave myolysis technique

combined with endometrial ablation under ultrasound guidance has been described previously in [49]–[52].

We are exploring the technical feasibility of minimally invasive transcervical microwave ablation of fibroids under hysteroscopic guidance for treating 1-3 cm Type 2 fibroids. Thermal sparing of the myometrium adjacent to the fibroid is of high priority in order to preserve the woman's ability to bear children. To achieve this goal, we have developed a 5.8 GHz MWA device that can be delivered via the instrument channel of a hysteroscope (~3 mm) with a steep transition from ablated tissue to thermally unaffected tissue, thereby restricting sub-ablative thermal exposure to surrounding myometrium. Due to the anatomy of the uterus, accurately positioning the applicator inside the fibroid when introduced via a transcervical approach may be challenging. Ablative approaches are usually designed for a wide range of fibroid sizes however, little attention has been placed on applicator insertion inaccuracies for small fibroids.

The objective of this study is to analyze the sensitivity of the ablation outcome to applicator position within the fibroid, as assessed by coverage (fraction of fibroid heated to ablative levels) vs. safety (volume of non-fibroid heated above a safe thermal dose threshold) as shown in Figure 5.1. To achieve this objective, we developed computational models of microwave ablation of uterine fibroids and validated the modeling results with experiments in *ex vivo* tissue. In addition, we evaluated the differences in the ablation outcomes based on the dissimilarities in the dielectric properties of the *ex vivo* human uterine fibroid tissue and bovine muscle which is commonly used as a surrogate tissue for fibroid ablation.
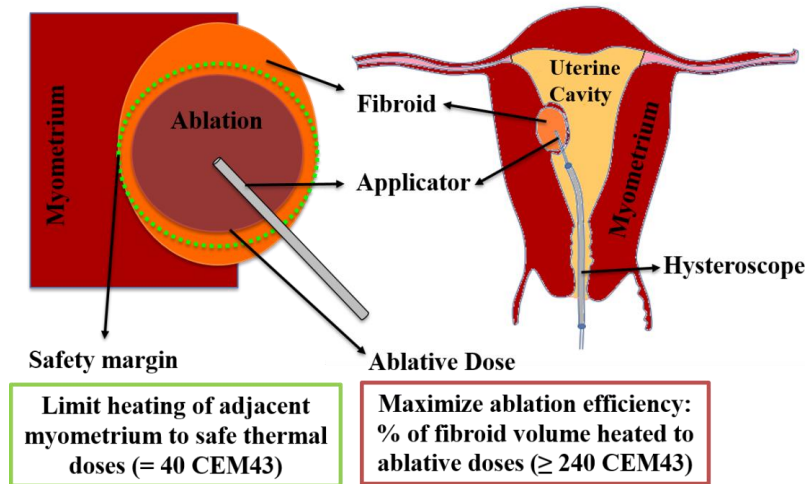
Figure 5.1 Uterus anatomy and treatment objectives of proposed Transcervical microwave ablation technology for Type 2 fibroids.

5.2 Methods

5.2.1 System Overview

The ablation system comprises of 1) a broadband microwave synthesizer (HP 83572A synthesized sweeper), 2) a 5.8 GHz frequency solid-state amplifier, 3) coaxial cables for transmission of power from the amplifier to the applicator 4) a wideband radiofrequency power meter (Bird Technologies 7022) for monitoring of forward and reflected power, 5) a custom designed 5.8 GHz water-cooled MWA applicator (discussed in Chapter 4) suitable for insertion into fibroid via the working channel of a hysteroscope, and 6) a peristaltic pump (Masterflex L/S economy drive model 7015-20) for circulating cooling water through the applicator.

The experimental evaluation was carried out in ex vivo bovine muscle similar to prior studies evaluating technologies developed for ablation of uterine fibroids [65] [44]. Fresh ex vivo bovine muscle was purchased from a local slaughterhouse and was carried to the lab in sealed plastic bags surrounded with ice packs. To raise the tissue temperature to approximately 37 ℃, tissue samples were sectioned, placed within thin sealed plastic bags which were then placed in a

temperature-controlled water bath. We considered the scenario where saline was continuously circulated through the uterine cavity for providing an unobstructed field of view [211],[212]. Briefly, the experimental setup consists of 1) a tissue holder template, 2) fiber optic temperature sensors (Reflex 4 channel, Optilink) interfaced with MATLAB® (Natick, MA) to control the heating duration and 3) a second water circulation circuit for maintaining the physiologic conditions of uterus [44].

5.2.2 Computational modeling

We employed a multi-physics computational model in COMSOL Multiphysics (v5.4, COMSOL Inc., Burlington, MA) to simulate the electromagnetic field and temperature distribution within and around the target area and predict the ablation performance *[195][196]*.

5.2.2.1 Equations

The following governing equations were discretized with the finite element method (FEM). The spatial distribution of the electric field in tissue was estimated by solving the time-harmonic Helmholtz electromagnetic wave equation:

$$\nabla^2 \mathbf{E} + \beta_0^2 \left(\varepsilon_r - \frac{j\sigma}{\omega\varepsilon_0} \right) \mathbf{E} = 0, \tag{5.1}$$

where $\mathbf{E}$ is electric field [V m^{-1}], β_0 is the wavenumber in free space [m^{-1}], ε_r is relative permittivity, σ is effective electric conductivity [S m^{-1}], ω is angular frequency [rad s^{-1}] and ε_0 is the permittivity of free space [F m^{-1}]. The time-averaged electromagnetic losses Q_{mw} were calculated using:

$$Q_{mw} = \frac{1}{2}\sigma\|\mathbf{E}\|^2 \tag{5.2}$$

Finally, temperatures in the simulated space were computed using the Pennes' bioheat equation.

$$\rho c \frac{\partial T}{\partial t} = \nabla \cdot k \nabla T + Q_{mw} - m_{bl} c_{bl} (T - T_{bl}) \qquad (5.3)$$

where ρc is the volumetric heat capacity [J m^{-3} °C^{-1}], T is the temperature [°C], k is the thermal conductivity [W m^{-1} °C^{-1}], m$_{bl}$ is the temperature dependent blood perfusion in fibroid and surrounding myometrium and c$_{bl}$ is the specific heat capacity of blood. T_{bl} is the physiologic temperature of the blood. The initial temperature in all tissue regions was set to 37 °C in the whole simulation domain.

Ablation outcome was estimated using the Cumulative Equivalent Minutes at 43°C (CEM43) thermal dose [68]:

$$CEM43 = \int_0^t R^{(43-T)} \, dt \ [\text{min}] \qquad (5.4)$$

where t is the time for which the tissue was kept at temperature T, R is a compensation factor for 1°C change in temperature which equals 0.5 for T > 43 °C and 0.25 for T ≤ 43 °C. The fraction of the fibroid volume where thermal dose defined by (5.4) exceeded 240 CEM43, as suggested for estimation of ablation boundary in [69], is referred to as ablation coverage. The extent of the tissue volume where thermal dose exceeded 40 CEM43, as suggested in [70] as a threshold between reversible and irreversible thermal effects to the muscle tissue, is monitored for the safety of the myometrium.

5.2.2.2 Geometry

The geometry of the model is shown in Figure 5.2 (a), and includes three regions, namely: fibroid, myometrium and uterine cavity. Moreover, geometric parameters describing applicator position with respect to fibroid central axis are defined in Figure 5.2 (b).
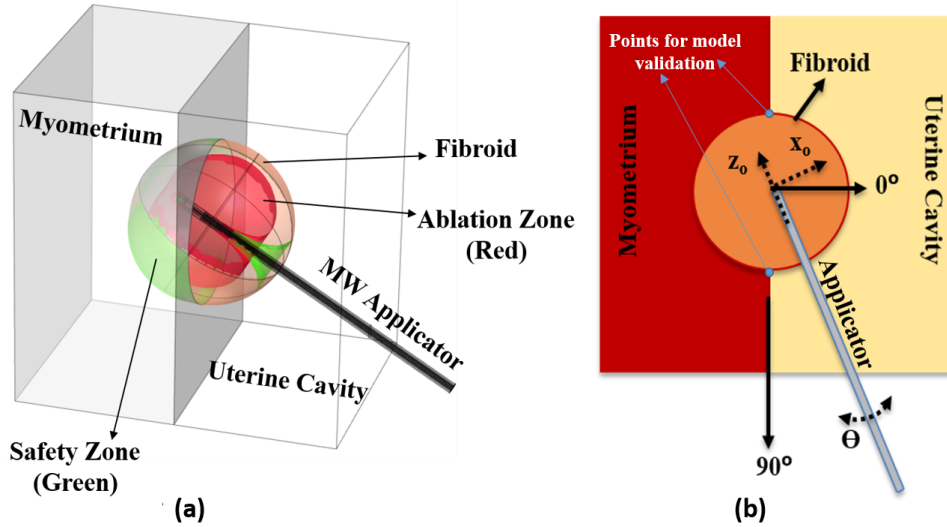
Figure 5.2 (a) Computational model geometry (b) Definition of geometry parameters for sensitivity analysis; insertion angle Θ, displacement in x-direction, x_o and displacement in z-direction, z_o. The blue dots in the figure depict the points used for validation of temperature in models with the experiments.

5.2.2.3 Material assignment

For equations (5.1) and (5.2), tissue dielectric property values within each domain [60], [63], [151], [202], [213] at the applicator's operating frequency 5.8 GHz are summarized in Table 5.1 (for details see Appendix E). Due to the lack of dielectric property data on uterine fibroids in the literature, we used the dielectric properties of *ex vivo* bovine muscle in the fibroid regions. Bovine muscle is often used as a surrogate for uterine fibroids [65] for preclinical evaluations, and was also used in our experiments.

For equation (5.3), the thermal tissue properties in simulation domains [126], [151], [214], [215] are given in Table 5.1 (for details see supplementary materials). Please note that heat transfer was not evaluated in uterine cavity since periodically flushed saline water is expected in that space during hysteroscopy. The thermal properties of the myometrium were approximated as being constant across temperature. Since the ablation treatment investigated in the present study is

terminated when the myometrium is exposed to a thermal dose greater than 40 CEM 43, peak tissue temperatures in the myometrium will not exceed ~55 ℃. Over the temperature range, 37 ℃ – 60 ℃, previous studies [126], [216] indicate minor changes in tissue thermal properties.

Table 5.1 Values of tissue properties used in simulations. For each tissue property we have provided the value at physiologic temperature and type of temperature dependency function with respective references.

Domain	Uterus	*Fibroid	Uterine Cavity
ε_r [-]	52.4 (constant) [151], [60]	43.33 (piecewise linear) [202], [202]	69.92 (constant) [213]
σ [S m^{-1}]	6.05 (constant) [151], [60]	4.23 (piecewise linear) [202]	7.84 (constant) [213]
ρc [MJ m^{-3} ℃$^{-1}$]	4 (constant) [151]	4 (piecewise constant) [151], [126]	-
k [W m^{-1} ℃$^{-1}$]	0.53 (constant) [151]	0.5 (piecewise linear) [151], [126]	-
m_{bl} [kg m^{-3} s^{-1}]	1.89 (reduced to zero at 60 ℃) [214], [215]	1.89 (reduced to zero at 60 ℃) [214], [215]	-
c_{bl} [J kg^{-1} ℃$^{-1}$]	3617 [151]	3617 [151]	-

5.2.2.4 *Boundary conditions*

The following boundary conditions were applied. The Sommerfeld radiation condition was applied at all outer boundaries of simulated space using the following approximation:

$$\mathbf{n} \times (\nabla \times \mathbf{E}) - jk\mathbf{n} \times (\mathbf{E} \times \mathbf{n}) = 0, \qquad (5.5)$$

where n is a unit vector perpendicular to the specific boundary. Furthermore, outer boundaries of the simulated space were subjected to a thermal insulation boundary condition:

$$\mathbf{n} \cdot (k\nabla T) = 0, \qquad\qquad (5.6)$$

A convective heat flux boundary condition was applied on the boundary between uterine cavity and uterine wall as well as fibroid to model saline water flushed during hysteroscopy procedures:

$$q_o = h.\,(T_{ext} - T), \qquad\qquad (5.7)$$

where q_o is the modelled heat sink, h stands for heat flux coefficient of value 30 [W m^{-2} °C^{-1}], and T_{ext} stands for room temperature of the saline water which was 20 °C. Another heat flux boundary condition was applied on the shaft of the applicator to mimic the internal cooling of applicator. In this case, the heat flux coefficient h was 1000 [W m^{-2} °C^{-1}] and external temperature T_{ext} was 15 °C.

5.2.2.5 *Meshing*

The overall size of the simulation space for 3 cm diameter fibroid simulations was 6 cm × 4.5 cm × 10 cm and for 1 cm diameter fibroid simulations simulation space was 3.5 cm x 3.6 cm x 10 cm respectively. While selecting appropriate meshes for the domains, the size of mesh elements was gradually decreased in each domain and the changes of model output (as defined by maximum temperature around the applicator and ablation size and shape) were monitored. The largest mesh element sizes, which yielded insignificant model output deviations with respect to model with the highest density mesh elements, were chosen to provide a reasonable balance between spatial resolution and computational complexity.

The tetrahedral mesh density was kept highest at the input port (0.1 mm), spacing of mesh elements was coarser around the antenna (0.25 mm), and the largest distance between two elements was 1.8 mm in the fibroid and 2.7 mm in myometrium and uterine cavity. For 3 cm fibroid simulations, the total number of mesh elements in the model was around 547,046, the maximum

number of degrees of freedom was 3,672,192 and the average time to complete one simulation was approximately 10-11 hrs. For 1 cm fibroid simulations, the total number of mesh elements in the model was around 408376, the maximum number of degrees of freedom was around 2672436 and the average time to complete one simulation was approximately 8 hrs. Models were run on a computer with an Intel(R) Core(TM) i7-8700 CPU running at 3.2 GHz and 64 GB RAM.

5.2.3 Experimental assessment of model predictions

In the present study, computational models were applied to assess the impact of applicator position within a uterine fibroid on thermal ablation profiles in the fibroid and the thermal dose accrued in adjacent myometrium. Experiments were conducted in ex vivo tissue to comparatively assess model predictions of ablation zone extents and transient temperature at the fibroid – myometrium against experimental observations. Experimental results were compared with model predictions from *ex vivo* simulations i.e. no perfusion was applied. The initial temperature of the ex vivo tissue in simulations was 37 °C, and in experiments was approximately 37 °C. The experimental setup is similar to a previous study [44], and is shown in Figure 5.3.
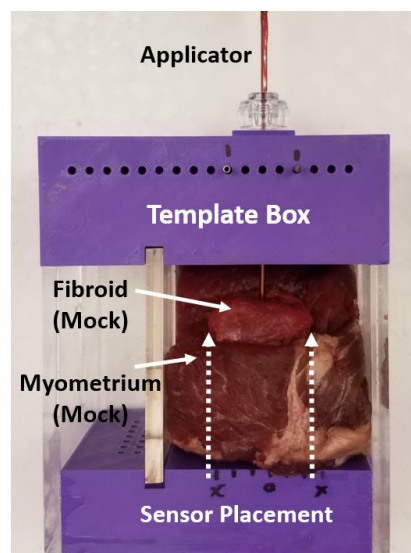
Figure 5.3 Experimental setup for model validation.

Briefly, the experimental setup consists of a plastic fixture template to hold the tissue and fix the applicator and temperature sensors at specified positions within the tissue. To mimic a type 2 fibroid protruding into the uterine cavity, we first used a block of bovine muscle to represent the uterine wall (myometrium). A 3 cm diameter cavity was created in the wall, within which a ~3 cm near-spherical piece of bovine muscle was inserted to represent a mock fibroid. The applicator was inserted into the center of the mock fibroid and two fiber optic sensors were placed at different locations along the boundary between the mock fibroid and myometrium. The template was immersed in a bath of 0.9% isotonic saline to emulate the uterine cavity at physiologic temperature. Ablations were performed in three different tissue samples with 30 W at applicator input and 10 min treatment duration. Fiber optic temperature sensors were used to provide real-time monitoring of the thermal dose within the mock myometrium and power was turned off whenever the measured thermal dose at either point reached the safety threshold of 40 CEM43.

Measured transient temperature profiles were compared with the profiles from the simulations using Root Mean Square Error (RMSE). Positions of the fiber optic sensors were manually registered for comparison against simulated temperatures at the corresponding locations (shown in Figure 5.2).

After ablations were completed, mock fibroids were extracted, cut along the applicator axis and photos of the visibly discoloured tissue representing the ablation zone were taken. Ablation extents were automatically segmented from photos with a custom image processing algorithm, which is based on k-means algorithm and subsequent significant area selection for de-noising purpose. The contours of the segmented ablation zones were overlaid on simulated temperature maps. The extent of simulated and experimentally measured thermal ablation zone contours were

compared by evaluating differences in surface areas and calculating dice similarity coefficients (DSC).

5.2.4 Scenarios for evaluation of sensitivity with respect to position

To simplify treatment planning, it is desirable to place the applicator through the central axis of the fibroid. Accurate placement of the ablation applicator into the center of the fibroid under hysteroscopic guidance may be challenging due to limited field of view, mechanical properties of the fibroid, and lack of imaging feedback regarding the applicator position once it penetrates the fibroid capsule. Therefore, it is important to estimate how the ablation outcome may change as a function of the displacement of applicator from the central axis inside the fibroid.

Table 5.2 Geometric parameters considered for sensitivity analysis.

Fibroid Diameter	3 cm	1 cm
Insertion angle Θ [º]	30, 45, 60	30, 45, 60
Displacement in X-direction x_o [mm]	-2 ,0 ,2	-1, 0, 1
Displacement in Z-direction z_o [mm]	-2 ,0 ,2	-2, 0

To evaluate the sensitivity of ablation outcome while satisfying safety constraints during experiments and simulations, we assumed a set of geometrical relations between the applicator and fibroid which are provided in Table 5.2 for the case of 3 cm and 1 cm diameter fibroids with *in vivo* settings (blood perfusion effects incorporated). The ablation coverage for input power 35 W and maximum treatment duration of 10 min for 3 cm fibroid and 15 W with duration of 5 min for 1 cm fibroid was evaluated while keeping safety constraint i.e. whenever thermal dose higher than 40 CEM43 was detected in myometrium, the ablation was stopped. A total of 27 simulations for the 3 cm fibroid case and 18 simulations for the 1 cm fibroid case were performed in such a way that all geometry parameter combinations listed in Table 5.2 were covered. Sensitivity of

ablation outcome was then studied by identifying the effect of one geometry parameter when all others remained fixed. For certain geometry parameter combinations of interest, ablation coverage was also assessed for maximum treatment time (600 s for 3 cm fibroids, 300 s for 1 cm fibroids). The maximum attainable ablation coverage in fibroid as well as extent of potential collateral damage in myometrium (thermal dose > 40 CEM43) was measured in cm^3.The sensitivity analysis was repeated for both 3 cm and 1 cm fibroids, for cases where 50% and 65% of the fibroid volume was within the myometrium. Post processing of data acquired from COMSOL models and the sensitivity analysis was implemented in MATLAB.

5.2.5 Scenarios for evaluation of sensitivity with respect to tissue dielectric properties

To quantify the differences in the ablation outcomes based on the dissimilarities in the dielectric properties of the human uterine fibroid tissue and the surrogate tissue used for fibroid ablation (bovine muscle), the parametric models of fibroid dielectric properties (presented in Chapter 3) were used in computer models. The ablation outcomes of the mean, upper and lower envelope of the fibroid dielectric properties were compared with the ablation outcomes of bovine muscle models for 1 cm and 3 cm diameter fibroids. The ablation outcomes were computed in terms of temperature and thermal dose thresholds.

5.3 Results

5.3.1 Experimental assessment of model predictions

Figure 5.4 shows the simulated and experimentally measured transient temperature profiles at the periphery of the mock fibroid during ablation. The points at which the temperatures were evaluated within the model were carefully registered with the actual placement of sensors in the experiments. There were two fiber optic sensors in each experiment; in one experiment, one of the sensors failed and thus Figure 5.4 includes five rather than the anticipated six temperature profiles.
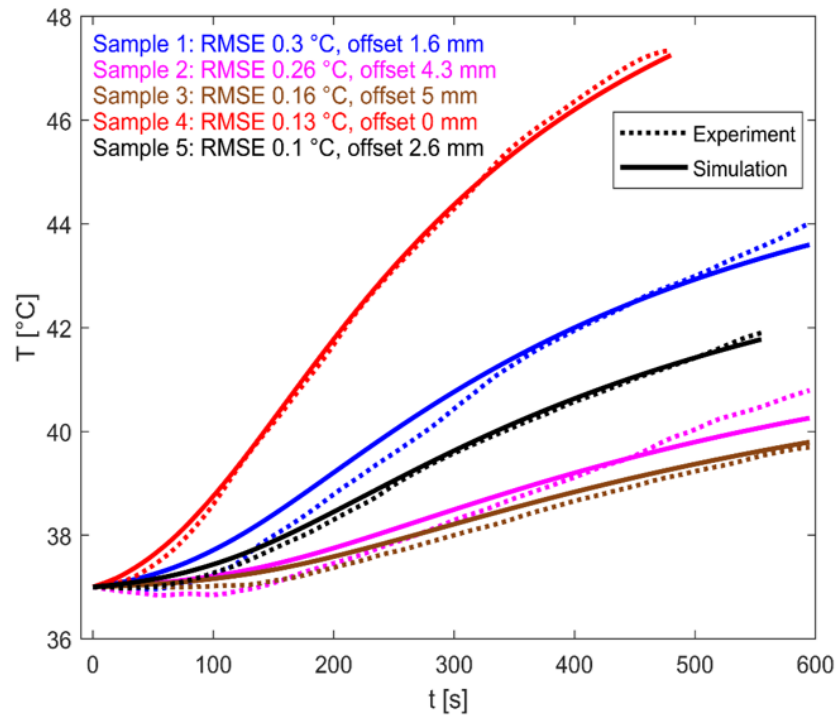
Figure 5.4 Experimentally measured and simulated transient temperature profiles at the fibroid-myometrium boundary for 30 W ablation in a 3 cm fibroid. Also shown are the RMSE between measured and simulated temperatures. Adjustments to temperature sensor position in simulation so as to mimic experimental positions are also displayed.

Figure 5.5(a) illustrates contours of the ablation zone extent observed experimentally as well as those predicted by simulation. Also shown is the simulated 40 CEM43 contour.

Figure 5.5(b) shows an example photo of discolored tissue representing the experimentally observed ablation zone.

(a)

(b)
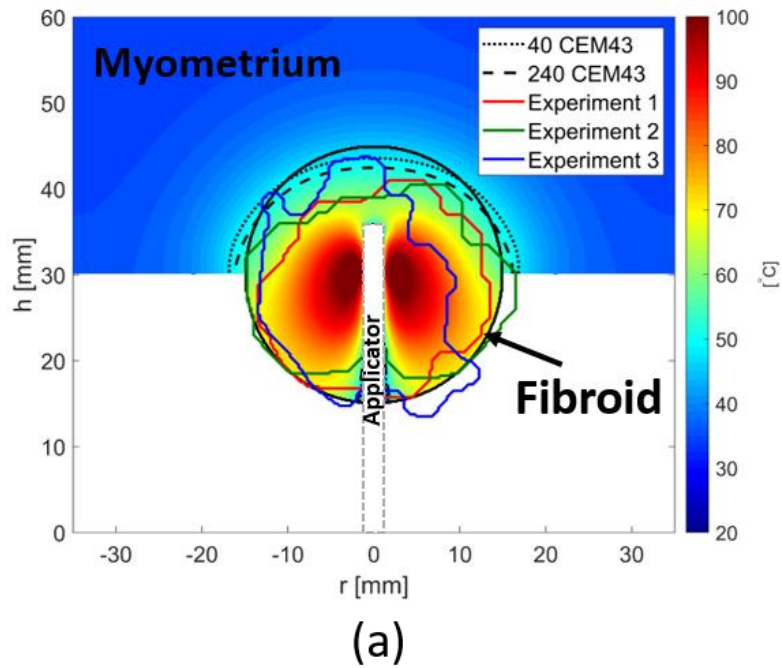
Figure 5.5 Comparison of ablations from experiments and simulation. (a) Simulated temperature map after 30 W, 10 min ablations (b) Photo of experimental ablation zone in a 3 cm mock fibroid.

Table 5.3 lists the DSC and surface areas of experimentally observed and simulated ablation zones.

Table 5.3. Comparison of experimental and simulated ablation zone dimensions following 30 W, 10 min ablation.

Margins	Surface area [mm^2]	DSC [-]
40 CEM43	667.1	-
240 CEM43	617.2	-
Experiment 1	508.2	0.83
Experiment 2	536.5	0.86
Experiment 3	479.8	0.75

5.3.2 Sensitivity to applicator positioning

Figure 5.6 and Figure 5.7 show the overall sensitivity data for 3 cm fibroid and 1 cm fibroid cases respectively, when the ablation procedure satisfied the constraint of no significant thermal effect in the surrounding myometrium i.e. when all points in the myometrium received a thermal dose less than 40 CEM43. In Figure 5.6(a) and Figure 5.7(a), each point labelled with an asterisk represents the percentage of fibroid volume ablated for a specific applicator insertion parameter (x offset x_o, z offset z_o and insertion angle Θ). Figure 5.6(b) and Figure 5.7(b) depicts the ablation durations for corresponding points in Figure 5.6(a) and Figure 5.7(a), respectively; if the ablations were continued beyond these durations, the thermal dose accrued in the myometrium would exceed 40 CEM43.
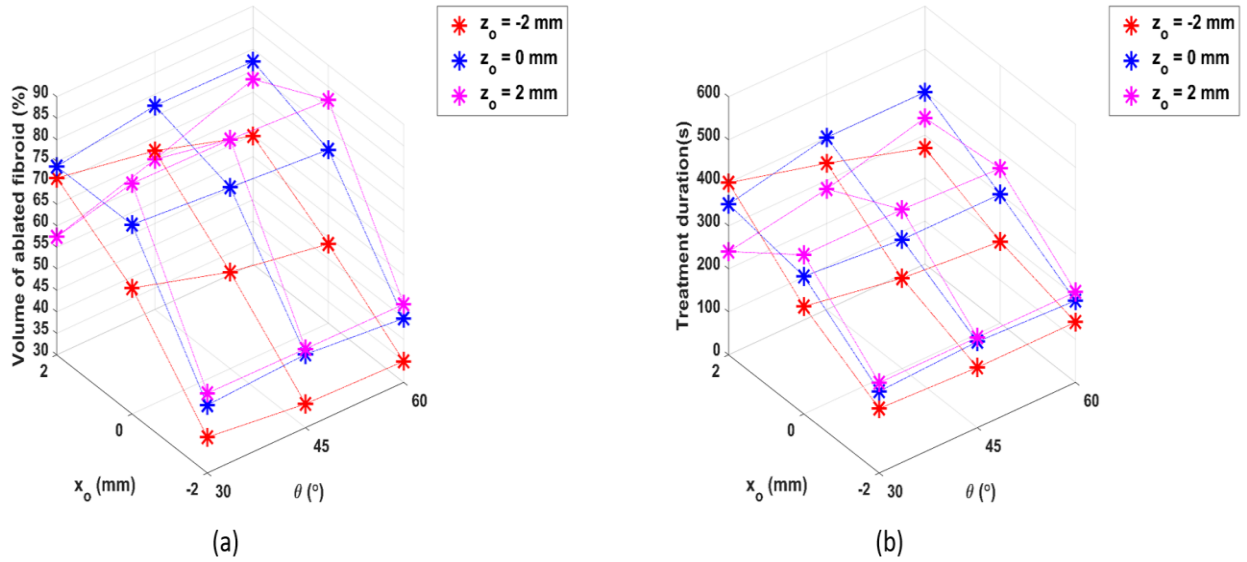
Figure 5.6 Graphical illustration of the variation in (a) ablation coverage and (b) treatment duration with respect to insertion angle, 'Θ', displacement in x-direction, 'x_o' and displacement in z-direction 'z_o' for 3 cm diameter fibroid when using 35 W input power and restricting the myometrium to 40 CEM43. Each asterisk on the plot depicts an output from 1 out of 27 simulation cases in sensitivity analysis. The dashed interconnection of points show the trends in the ablation outcome and treatment duration with respect to the three input parameters in a 3D space.
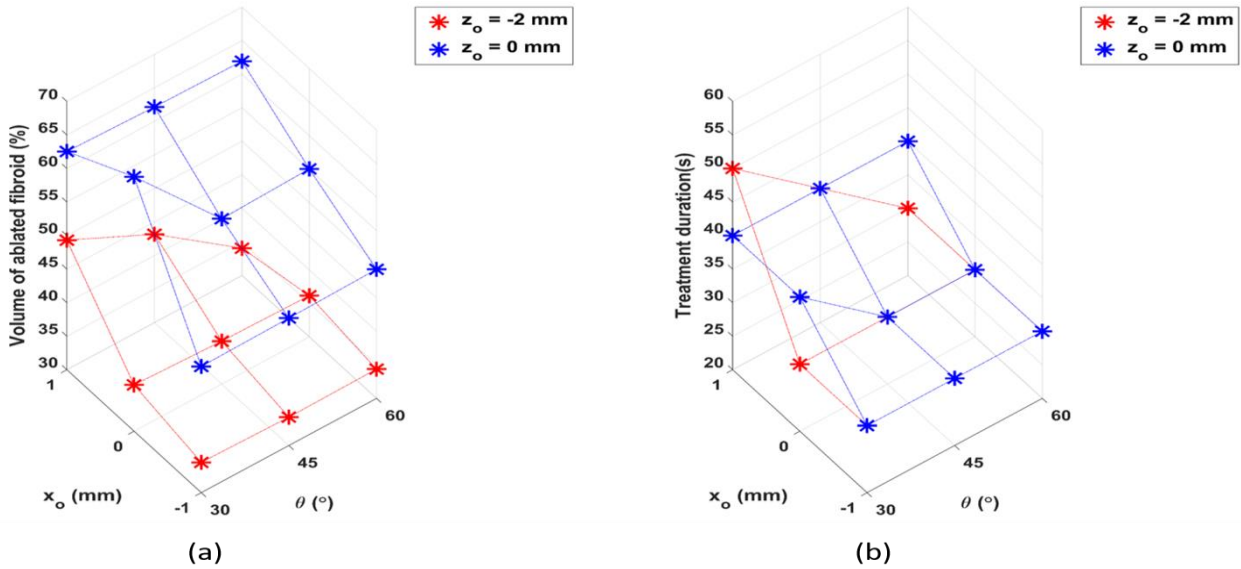
Figure 5.7 Graphical illustration of variation in (a) ablation coverage and (b) treatment duration with respect to insertion angle, 'Θ', displacement in x-direction, 'x_o' and displacement in z-direction, 'z_o' for 1 cm diameter fibroid when using 15 W input power and restricting the myometrium to 40 CEM43. Each asterisk on the plot depicts an output from 1 out of 18 simulation cases in sensitivity analysis. The interconnection of points show the trends in the ablation outcome and treatment duration with respect to the three input parameters in a 3D space.

Figure 5.8 illustrates ablation coverage sensitivity in a 3 cm fibroid target with insertion angle and lateral displacement with respect to the central axis of fibroid. Figure 5.8(a, b, c) demonstrates the variation in % of fibroid ablated if the applicator insertion angle 'Θ' changes from 30º-60º. Figure 5.8(d, e, f) displays the variation in the ablation outcome when the applicator is displaced (i.e. from $x_o = 0$ to ±2 mm) keeping other two geometric parameters constant.
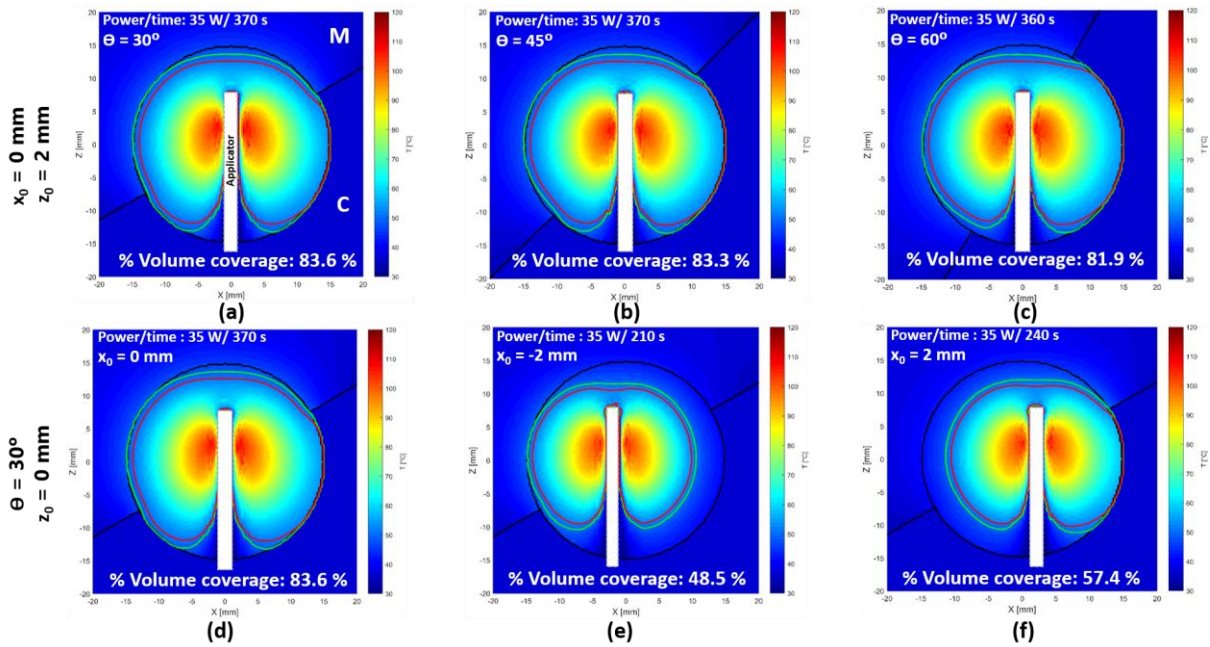
Figure 5.8 Illustration of thermal profiles following 35 W ablation in 3 cm fibroid for varying insertion angles, Θ (a, b, c) and lateral offsets, x_o (d, e, f). Thermal profiles are illustrated with red contour (ablation threshold = 240 CEM43) and green contour (safety threshold = 40 CEM43) inside the fibroid (shown in black contour), myometrium, 'M' and the uterine cavity, 'C'.

Figure 5.9 gives a similar analysis for 1 cm fibroid cases as shown in Figure 5.8.
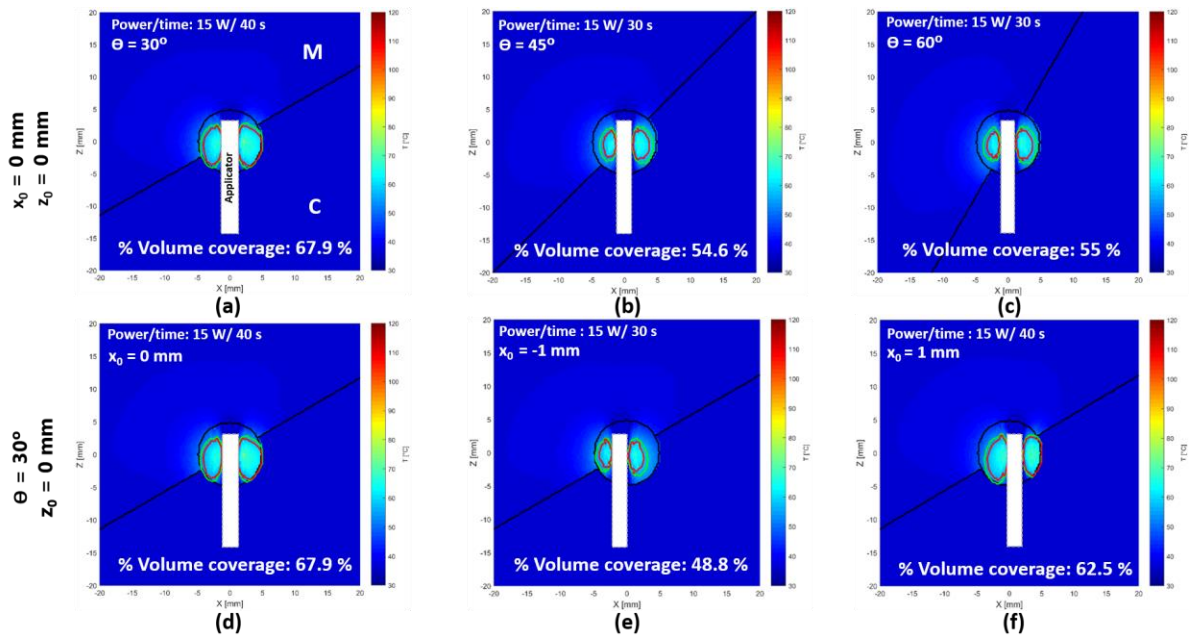
Figure 5.9 Illustration of thermal profiles following 15 W ablation in 1 cm fibroid for varying insertion angles, Θ (a, b, c) and lateral offsets, x_o (d, e, f). Thermal profiles are illustrated with red contour (ablation threshold = 240 CEM43) and green contour (safety threshold = 40 CEM43) inside the fibroid (shown in black contour), myometrium, 'M' and the uterine cavity, 'C'.

Figure 5.10 illustrates variation in ablation zones when the applicator displaces slightly (in x_o), for 3 cm fibroid case (a, b, c) and 1 cm fibroid case (d, e, f), and when the safety constraints were ignored (i.e. if there was no limitation on thermal dose accrued within the myometrium). For the simulations shown in Figure 5.10, ablation duration was held to 600 s for the 3 cm fibroid, and to 300 s for the 1 cm fibroid.
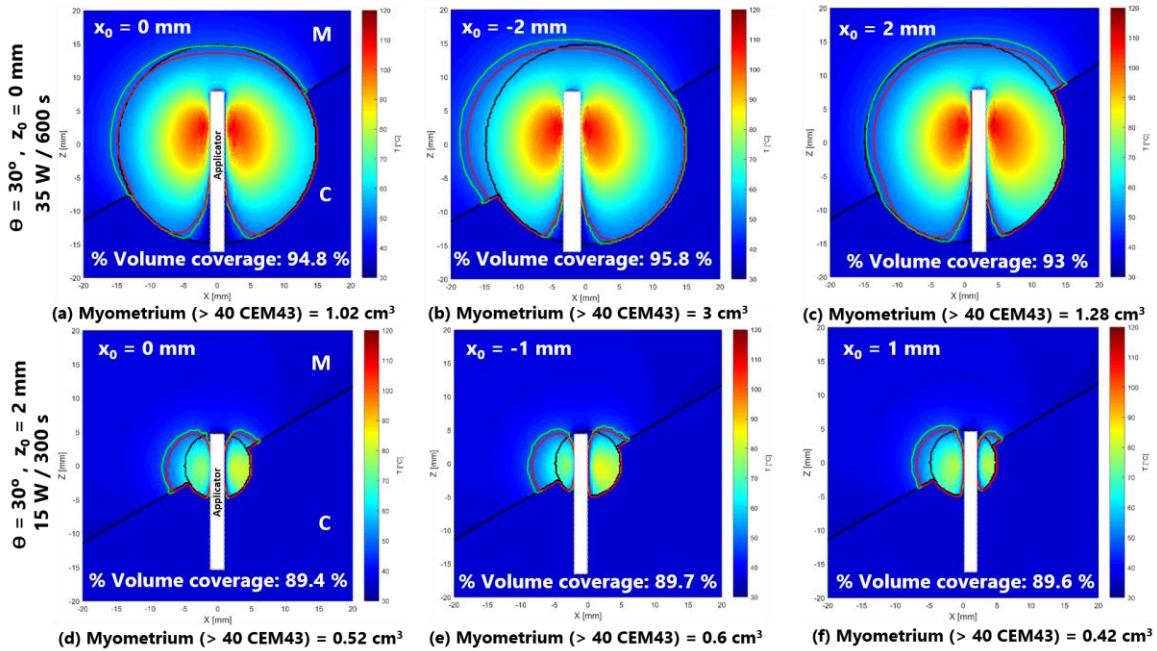
Figure 5.10 Examples of thermal profiles following ablations where there are no constraints on myometrium temperature. 35 W, 600 s ablation in 3 cm fibroid with (a) $x_o = 0$ mm, (b) $x_o = -2$ mm, (c) $x_o = 2$ mm and 15 W, 300 s in 1 cm fibroid with (d) $x_o = 0$ mm, (e) $x_o = -1$ mm, (f) $x_o = 1$ mm. Thermal profiles are illustrated with red contour (ablation threshold = 240 CEM43) and green contour (safety threshold = 40 CEM43) inside the fibroid (shown in black contour), myometrium, 'M' and the uterine cavity, 'C'. Also shown are the volumes of myometrium heated above 40 CEM43.

5.3.3 Sensitivity to tissue dielectric properties

Figure 5.11 displays the ablation profiles when fibroid dielectric properties are used in the computational models in comparison to bovine muscle dielectric properties for 1 cm fibroids.

Figure 5.11 Illustration of sensitivity of ablation profiles with respect to changes in dielectric properties in 1 cm fibroid with applied power P = 15 W for t = 30 s. The difference in a) ablation outcome, b) safety contours, c) radial temperature roll off at h = 0 mm cut-plane, d) radial isoeffective thermal dose roll off at h = 0 mm cut-plane, e) radial temperature roll off at h = 2 mm cut-plane, and f) radial isoeffective thermal dose roll off at h = 2 mm cut-plane.

Figure 5.12 displays the ablation profiles when fibroid dielectric properties are used in the

computational models in comparison to bovine muscle dielectric properties for 3 cm fibroids.
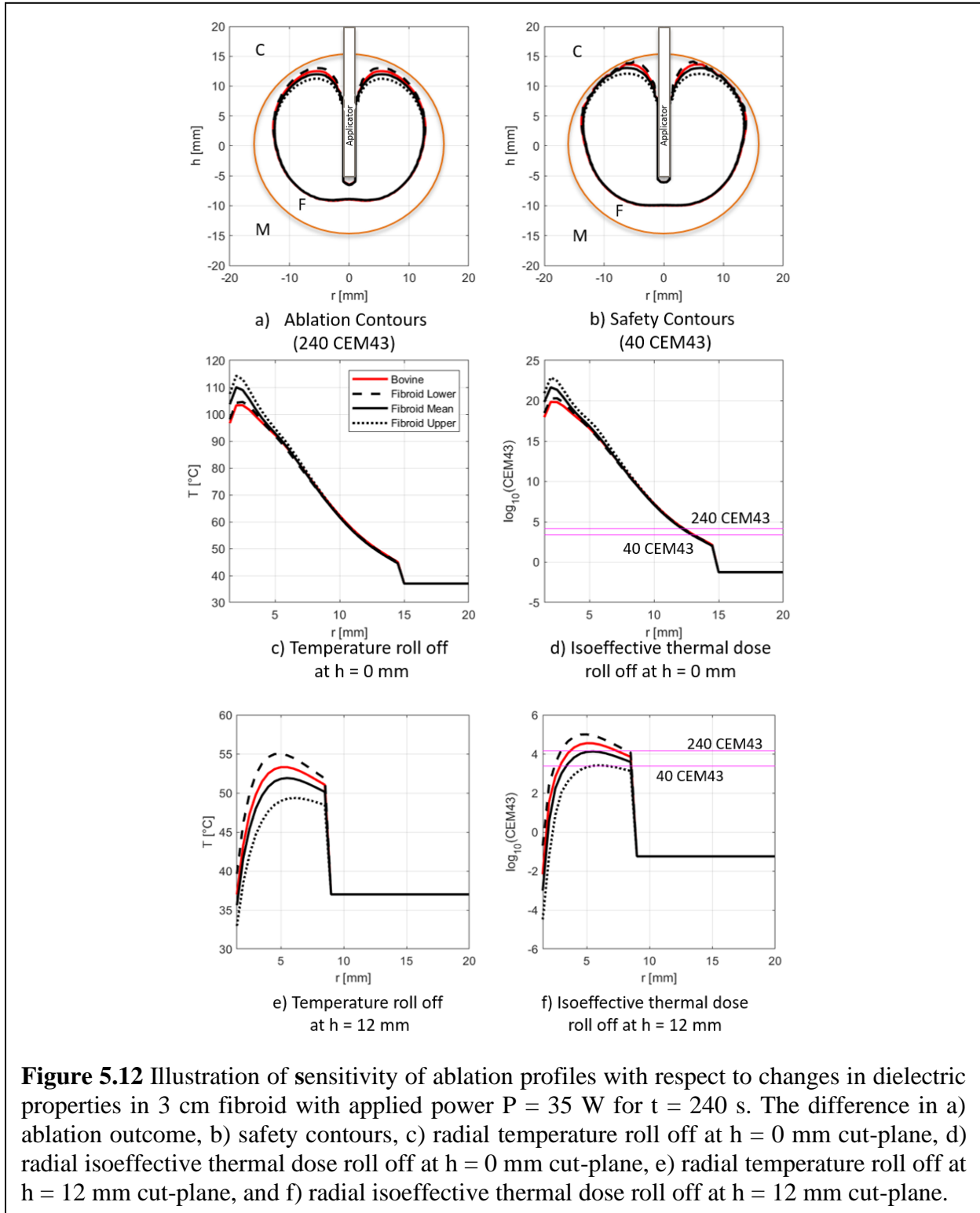
Figure 5.12 Illustration of sensitivity of ablation profiles with respect to changes in dielectric properties in 3 cm fibroid with applied power P = 35 W for t = 240 s. The difference in a) ablation outcome, b) safety contours, c) radial temperature roll off at h = 0 mm cut-plane, d) radial isoeffective thermal dose roll off at h = 0 mm cut-plane, e) radial temperature roll off at h = 12 mm cut-plane, and f) radial isoeffective thermal dose roll off at h = 12 mm cut-plane.

Table 5.4 enumerates the differences in the ablation outcomes when fibroid dielectric properties (lower, mean and upper envelopes) and bovine dielectric properties are employed in the computational models.

Table 5.4 Variations in ablation outcomes as a function of tissue dielectric properties.

Tissue Properties		Fibroid diameter = 1 cm (P = 15 W, t = 30 s)		Fibroid diameter = 3 cm (P = 35 W, t = 240 s)	
		% Volume coverage for ablation	Transition zone (240 CEM43 → 40 CEM43) (cm^3)	% Volume coverage for ablation	Transition zone (240 CEM43 → 40 CEM43) (cm^3)
Bovine		27.1 %	0.10	56 %	1.91
Fibroid	Lower Envelope	28.8 %	0.96	57.2 %	1.77
	Mean Envelope	36.8%	0.86	53 %	1.94
	Upper Envelope	44.1%	0.71	51.6 %	1.79

5.4 Discussion

In this study, we investigated the relationship between microwave ablation applicator position and ablation outcome, considering 1 – 3 cm uterine fibroids, where outcome was assessed based on volume of the fibroid heated to ablative temperatures (coverage) while limiting the maximum thermal dose accrued in surrounding myometrium to 40 CEM43. The highest coverage of 83.6% was achieved when the applicator was inserted at an angle of $\theta = 30^{\circ}$, $x_o = 0$ mm and $z_o = +2$ mm in a 3 cm fibroid while the lowest coverage of 34.9% was recorded when the applicator was placed at an $\theta = 60^{\circ}$ and linear displacement of $x_o = -2$ mm and $z_o = -2$ mm. For 1 cm fibroids, the maximum ablation coverage of 67.9% was observed with applicator inserted at $\theta = 30^{\circ}$ at the center point of the fibroid with no displacement in x and z directions. Displacing the applicator by $x_o = +1$ mm and $z_o = -2$ mm with an insertion $\theta = 60^{\circ}$ yielded lowest ablation coverage of 34.1%.

As can be seen in Figure 5.6 and Figure 5.7, for both fibroid sizes the ablation time and consequently coverage appears to be more sensitive to displacement of applicator than the applicator insertion angle. Displacements towards the uterine cavity yield higher ablation efficiencies than the displacements in the opposite direction. This may be explained by the fact that the applicator shaft is farther from the myometrium boundary, where the rise of temperature is therefore delayed which allows more time for the ablation zone to grow within the fibroid before the safety threshold is exceeded. Overall, for the power levels investigated in this study, 3 cm fibroids could be ablated to coverage levels of 34.9– 83.6% within 140 – 400 s, while 1 cm fibroids could be ablated to coverage levels of 34.1– 67.9% within 30 – 50 s.

For symptom relief and preservation of fertility of the patient, the main aim is to maximally ablate the fibroid without damaging the critical structures around the fibroid. The data illustrated

in Figure 5.6 and Figure 5.7 summarize the fraction of the fibroid ablated and ablation duration for candidate applicator tip positions and insertion angles. The temperature profiles illustrated in Figure 5.8 and Figure 5.9 for 3 cm and 1 cm fibroid cases, respectively, illustrate the treatment profiles inside the fibroid with respect to the myometrium and uterine cavity. This representation can serve as an aid for the clinicians during procedure treatment planning to visualize how the ablation zone and thermal profiles extend within the fibroid and surrounding tissue. Depending upon the patient anatomy and fibroid size, location and depth inside the uterus wall, the clinician can identify the range of insertion angle and applicator tip positions which yield acceptable ablation profiles.

Figure 5.10 shows that for both fibroid sizes ablation coverage ~ 90% or higher can be achieved when the ablation duration is increased to 10 min for 3 cm fibroid case (a, b, c) and 5 min for 1 cm fibroid case (d, e, f). In this case, the temperature in myometrium adjacent to the fibroid may rise up to 65 ℃ (in 3 cm case) and 70 ℃ (in 1 cm case) when we allow the maximum thermal dose threshold in myometrium to exceed 40 CEM43. Our microwave generator had a limit of supplying a maximum of 35 W to the applicator. Higher power levels may facilitate shorter ablation times as well as ablation of larger fibroids.

Figure 5.11, Figure 5.12, and Table 5.4 shows the variation in ablation profiles as a function of dielectric properties. It can be seen in the Figure 5.11, for 1 cm fibroid since the time duration for heating is small (30 s), the ablation outcomes are primarily dependent on the SAR profiles which are significantly affected by the dielectric properties of the target tissue. The ablation coverage achieved while using lower envelope of fibroid dielectric properties are similar to the bovine muscle models for both 1 cm and 3 cm fibroid ablations which is supported by the Figure 3.4 where the dielectric properties of bovine muscle lie closer to the lower envelope of fibroid dielectric properties. The volume coverage achieved while using mean and upper envelope of fibroid dielectric properties are considerably higher than the lower envelope of fibroid and the bovine muscle properties in 1 cm fibroid case. For 3 cm fibroids, since the duration of heating is large, the thermal conduction effects become more prominent. A common set of thermal properties for fibroids and bovine muscle were employed in the models, contributing to the ablation outcomes in all four cases are not significantly different.

Table 5.3 illustrates the validation of the computational model. The observed differences between ablation contours from experiments and simulation can be explained by several factors, including: 1) errors in location of the sensors vs applicator in experiments, 2) geometric inaccuracies in the experimental setup, and 3) bovine muscle structural consistency. Figure 5.4 indicates the role of the first factor because it states registered offsets between simulation and experiments for which almost perfect alignment of temperature curves was achieved. The second factor could affect the actual volume of ablated tissue as well as the position of sensors and applicator because it deals with the precision of tissue preparation and therefore dimensions of mock fibroid and its central access with respect to applicator and sensors. The third factor could affect the experimental ablation sizes in direction of muscle fibers which were observed to enhance heat transfer in the respective direction.

Technologies for hysteroscopy-guided ablation of fibroids via a transcervical approach are attractive because of their reduced invasiveness compared to laparoscopic approaches. However, a hysteroscopic approach places constraints on the approach angle for advancing the applicator into the fibroid. Fibroids in the fundal region can be approached with the applicator almost perpendicular to the uterine wall, which may allow for more accurate placement of the applicator down the central axis of the fibroid. However, when targeting fibroids on the lateral walls of the uterus, the limited range of angles that can be achieved with a rigid hysteroscope may present technical limitations with regards to central placement of the applicator. Our simulations indicated more medial positioning of the applicator tip (2 mm off-centre) yielded improved ablation coverage compared to central or more lateral placement. Ultrasound imaging and electromagnetic tracking systems, such as those in clinical use for RFA of fibroids [40] [217], may provide a means to guide the operator in confirming suitable positioning of the applicator.

Limitations of this study include the simplified spherical shape assumed for fibroids, and the lack of tissue physical properties of fibroids, which were approximated by tissue properties of bovine muscle. Furthermore, the variability of tissue properties was not taken into account in this study. Computational model predictions of ablation extents and transient temperature at the fibroid – myometrium boundary were compared against observations from experiments in ex vivo tissue; such comparison of ablation profile and transient temperatures at a few discrete points is an established approach for assessing computational models of microwave ablation [165], [218], [219]. A more detailed validation of the model including transient temperatures at a wider range of points, such as that feasible with MR thermometry [220] would further add to model credibility and establish an even broader model validation. Another limitation in our experimental setup was the upper power limit of the generator of 35 W which resulted in rather small number of investigated power/time combinations where target volume was achieved. Future studies focusing on measurement of fibroid electrical and thermal properties and their temperature dependencies will enable more detailed and representative modelling of fibroid ablations.

5.5 Conclusion

A computational model for simulating microwave ablation of uterine fibroids was presented and validated with data from *ex vivo* experiments for target diameters ranging from 1 to 3 cm. We have demonstrated the impact of applicator positioning of the ablation applicator inside the fibroid on ablation coverage for symptomatic relief, under the constraint of maximum thermal preservation of adjacent normal tissue. Moreover, we have shown that the *ex vivo* bovine muscle tissue is a reasonable surrogate for the fibroid ablation in terms of dielectric properties. However, further studies are warranted to determine the differences in ablation outcomes due to the thermal, mechanical and structural properties of the fibroid and bovine tissues to evaluate the suitability of using bovine muscle as a surrogate tissue for evaluating fibroid ablation technologies.

Chapter 6 - Conclusion and Future Work

Technologies for hysteroscopy-guided ablation of fibroids via a transcervical approach are attractive because of their reduced invasiveness compared to other approaches. This dissertation demonstrates the technical feasibility of transcervical hysteroscopic microwave ablation for fibroid treatment and the relationship between applicator position within the fibroid and fraction of fibroid that can be ablated while limiting thermal dose in adjacent tissues.

The temperature dependent dielectric properties of uterine fibroid tissues over microwave frequency range are reported for the first time in Chapter 3 of this dissertation. Parametric models of uterine fibroid dielectric properties are also presented for incorporation within computational models of microwave ablation of fibroids. Since fibroids are highly heterogeneous tissues, this study could be improved in future to measure the dielectric and thermal properties of fibroids in a large tissue sample at the time of excision to eliminate any dehydration effects and include the fibroid variability analysis with respect to tissue composition with the pathology reports of the tissue samples. The preparation of tissue samples for histopathology analysis could be technically challenging as it would limit the amount of tissue sample available for the measurement of tissue properties.

In Chapter 4, a 5.8 GHz water-cooled monopole MWA applicator has been designed for transcervical ablation of 1-3 cm diameter fibroid via hysteroscopy and tested in *ex vivo* tissues and thermos-chromic tissue mimicking gel phantoms. This 2.15 mm diameter applicator incorporates a novel design for internal impedance matching, a short monopole (2.5 mm), a balun and dielectric loading providing an efficient power transmission to antenna (i.e. |S11| <-10 dB), spherical radiation profile and 33% faster radial transition from ablated (55 ℃) to non-ablated zone (43 ℃) than the previous applicator designs at 2.45 GHz. Themo-chromic tissue mimicking gel phantoms

evaluated in this dissertation can be used for quantitative assessment of the fabricated applicators, however for the quantitative assessment more studies are required to characterize the thermal properties of the gel at elevated temperatures for validation of simulation results with experimental data. These thermo-chromic phantoms could provide a suitable tool for validation of applicator performance during translation of medical devices from research labs to industrialized manufacturing environments.

In Chapter 5, the ablation performance of microwave applicator was evaluated as a function of applicator positioning within the target fibroids (1-3 cm diameter) in experimentally validated computational models developed for transcervical hysteroscopic microwave ablation of fibroids. The applicator performance was assessed in terms of ablation coverage under the constraint of maximum thermal preservation of adjacent normal tissue (thermal dose $\leq$ 40 CEM43). The ablation outcome was evaluated with respect to applicator insertion angles, depth and offset from the center of the fibroid. Power deposition was stopped when thermal dose of 40 cumulative equivalent minutes at 43 °C (CEM43) was accrued in adjacent myometrium. Within the range of all evaluated insertion angles (30°, 45°, 60°), depths and offsets from the fibroid center (± 2 mm for 3 cm fibroid and ± 1 mm for 1 cm fibroid) with 35 W and 15 W applied power for 3 cm and 1 cm fibroids, respectively, the ablation coverage ranged from 34.9 – 83.6% for 3 cm fibroid in 140 – 400 s and 34.1 – 67.9% for 1 cm fibroid in 30 – 50 s of heating duration. The study suggests that the ablation outcome in a hysteroscopic approach is considerably sensitive (requires mm of accuracy) to the applicator positioning within the fibroid. Therefore, during a clinical procedure ultrasound imaging and electromagnetic tracking systems, such as those in clinical use for RFA of fibroids [40] [217], may provide a means to guide the physician in confirming suitable positioning of the applicator which yields acceptable ablation profiles inside the fibroid while thermal

protecting the surrounding tissues. Future works will include assessment of ablation profiles in *ex vivo* uterine fibroids to evaluate the performance of the MWA applicators and thereafter conducting *in vivo* studies in fibroid patients (who are prescribed with hysterectomy) to assess the ablation extents in an actual human fibroid.

In this dissertation, the technical feasibility of using 5.8 GHz MWA systems for transcervical fibroid ablation has been presented in terms of radial thermal profiles for the treatment of small fibroids (< 3 cm) since currently available 2.45 GHz applicator designs are not suitable for this application. For the clinical implementation of the technology presented in this dissertation, there are potential practical challenges which need to be addressed. Due to the design complexity of higher frequency systems, there is limited availability of high power 5.8 GHz generators. In a clinical setting, while delivering power (from the generator to the handheld ablation device) via longer transmission cables, there will be more power attenuation at 5.8 GHz as compared to lower frequency systems. For RG400 coaxial cable [221], the attenuation is 36 dB/100 ft. at 5 GHz as compared to 14.7 dB/100 ft. at 1 GHz and for RG393 coaxial cable [222], the attenuation is 21 dB/100 ft. at 5 GHz as compared to 7.5 dB/100 ft. at 1 GHz). The higher power attenuation at 5.8 GHz frequency will cause under delivery of required power to the applicator for ablations and excessive heating of transmission cable which would lead to both performance and safety issues.

Bibliography

[1]   E. A. Stewart, C. L. Cookson, R. A. Gandolfo, and R. Schulze-Rath, "Epidemiology of uterine fibroids: a systematic review," *BJOG: An International Journal of Obstetrics & Gynaecology*, vol. 124, no. 10, pp. 1501–1512, 2017, doi: 10.1111/1471-0528.14640.

[2]   T. L. Edwards *et al.*, "A Trans-Ethnic Genome-Wide Association Study of Uterine Fibroids," *Front. Genet.*, vol. 10, 2019, doi: 10.3389/fgene.2019.00511.

[3]   J. Donnez and M.-M. Dolmans, "Uterine fibroid management: from the present to the future," *Human Reproduction Update*, vol. 22, no. 6, pp. 665–686, Nov. 2016, doi: 10.1093/humupd/dmw023.

[4]   G. Shifrin, M. Engelhardt, P. Gee, and G. Pschadka, "Transcervical fibroid ablation with the Sonata^TM system for treatment of submucous and large uterine fibroids," *International Journal of Gynecology & Obstetrics*, vol. n/a, no. n/a, doi: https://doi.org/10.1002/ijgo.13638.

[5]   D. D. Baird, D. B. Dunson, M. C. Hill, D. Cousins, and J. M. Schectman, "High cumulative incidence of uterine leiomyoma in black and white women: ultrasound evidence," *Am. J. Obstet. Gynecol.*, vol. 188, no. 1, pp. 100–107, Jan. 2003, doi: 10.1067/mob.2003.99.

[6]   T. L. Edwards *et al.*, "A Trans-Ethnic Genome-Wide Association Study of Uterine Fibroids," *Front. Genet.*, vol. 10, 2019, doi: 10.3389/fgene.2019.00511.

[7]   A. R. W. Williams, "Uterine fibroids – what's new?," *F1000Res*, vol. 6, p. 2109, Dec. 2017, doi: 10.12688/f1000research.12172.1.

[8]   G. A. Vilos *et al.*, "The Management of Uterine Leiomyomas," *Journal of Obstetrics and Gynaecology Canada*, vol. 37, no. 2, pp. 157–178, Feb. 2015, doi: 10.1016/S1701-2163(15)30338-8.

[9]   R. M. Merrill, "Hysterectomy surveillance in the United States, 1997 through 2005," *Medical Science Monitor*, vol. 14, no. 1, pp. CR24–CR31, 2008.

[10]   D. Pavone, S. Clemenza, F. Sorbi, M. Fambrini, and F. Petraglia, "Epidemiology and Risk Factors of Uterine Fibroids," *Best Practice & Research Clinical Obstetrics & Gynaecology*, vol. 46, pp. 3–11, Jan. 2018, doi: 10.1016/j.bpobgyn.2017.09.004.

[11]   "Benign and malignant pathology of the uterus," *Best Practice & Research Clinical Obstetrics & Gynaecology*, vol. 46, pp. 12–30, Jan. 2018, doi: 10.1016/j.bpobgyn.2017.10.004.

[12]   H. S. Saleh, H. E. Mowafy, A. A. A. E. Hameid, H. E. Sherif, and E. M. Mahfouz, "Does Uterine Fibroid Adversely Affect Obstetric Outcome of Pregnancy?," *BioMed Research International*, vol. 2018, pp. 1–5, 2018, doi: 10.1155/2018/8367068.

[13]   J. J. Kim and E. C. Sefton, "The role of progesterone signaling in the pathogenesis of uterine leiomyoma," *Molecular and Cellular Endocrinology*, vol. 358, no. 2, pp. 223–231, Jul. 2012, doi: 10.1016/j.mce.2011.05.044.

[14]   B. V. Voorhis, "A 41-Year-Old Woman With Menorrhagia, Anemia, and Fibroids: Review of Treatment of Uterine Fibroids," *JAMA*, vol. 301, no. 1, pp. 82–93, Jan. 2009, doi: 10.1001/jama.2008.791.

[15]   M. G. Munro, H. O. D. Critchley, I. S. Fraser, and the FIGO Menstrual Disorders Committee, "The two FIGO systems for normal and abnormal uterine bleeding symptoms and classification of causes of abnormal uterine bleeding in the reproductive years: 2018 revisions," *International Journal of Gynecology & Obstetrics*, vol. 143, no. 3, pp. 393–408, Dec. 2018, doi: 10.1002/ijgo.12666.

[16]   S. E. Bulun, "Uterine Fibroids," *New England Journal of Medicine*, vol. 369, no. 14, pp. 1344–1355, Oct. 2013, doi: 10.1056/NEJMra1209993.

[17]   Y. Yoshino, N. Yoshiki, R. Nakamura, Y. Iwahara, T. Ishikawa, and N. Miyasaka, "Large leiomyomatosis peritonealis disseminata after laparoscopic myomectomy: A case report with literature review," *Int J Surg Case Rep*, vol. 77, pp. 866–869, 2020, doi: 10.1016/j.ijscr.2020.12.005.

[18]   A. Fauconnier, C. Chapron, K. Babaki-Fard, and J. B. Dubuisson, "Recurrence of leiomyomata after myomectomy," *Hum Reprod Update*, vol. 6, no. 6, pp. 595–602, Dec. 2000, doi: 10.1093/humupd/6.6.595.

[19]   C. M. Farquhar and C. A. Steiner, "Hysterectomy rates in the United States 1990-1997," *Obstet Gynecol*, vol. 99, no. 2, pp. 229–234, Feb. 2002, doi: 10.1016/s0029-7844(01)01723-9.

[20]   D. I. Galen, R. R. Pemueller, J. G. Garza Leal, K. R. Abbott, J. L. Falls, and J. Macer, "Laparoscopic Radiofrequency Fibroid Ablation: Phase II and Phase III Results," *JSLS*, vol. 18, no. 2, pp. 182–190, 2014, doi: 10.4293/108680813X13693422518353.

[21]   J. K. Gupta, A. Sinha, M. A. Lumsden, and M. Hickey, "Uterine artery embolization for symptomatic uterine fibroids," *Cochrane Database Syst Rev*, no. 5, p. CD005073, May 2012, doi: 10.1002/14651858.CD005073.pub3.

[22]   I. Manyonda *et al.*, "Uterine-Artery Embolization or Myomectomy for Uterine Fibroids," *N. Engl. J. Med.*, vol. 383, no. 5, pp. 440–451, 30 2020, doi: 10.1056/NEJMoa1914735.

[23]   T. Wang, H. Tang, Z. Xie, and S. Deng, "Robotic-assisted vs. laparoscopic and abdominal myomectomy for treatment of uterine fibroids: a meta-analysis," *Minimally Invasive Therapy & Allied Technologies*, vol. 27, no. 5, pp. 249–264, Sep. 2018, doi: 10.1080/13645706.2018.1442349.

[24]   L. M. Glaser, J. Friedman, S. Tsai, A. Chaudhari, and M. Milad, "Laparoscopic myomectomy and morcellation: A review of techniques, outcomes, and practice

guidelines," *Best Practice & Research Clinical Obstetrics & Gynaecology*, vol. 46, pp. 99–112, Jan. 2018, doi: 10.1016/j.bpobgyn.2017.09.012.

[25]   K. Piecak and P. Milart, "Hysteroscopic myomectomy," *Prz Menopauzalny*, vol. 16, no. 4, pp. 126–128, Dec. 2017, doi: 10.5114/pm.2017.72757.

[26]   R. J. Gimpelson, "Hysteroscopic treatment of the patient with intracavitary pathology (myomectomy/polypectomy)," *Obstetrics and Gynecology Clinics of North America*, vol. 27, no. 2, pp. 327–337, Jun. 2000, doi: 10.1016/S0889-8545(00)80024-8.

[27]   S. G. Derman, J. Rehnstrom, and R. S. Neuwirth, "The long-term effectiveness of hysteroscopic treatment of menorrhagia and leiomyomas," *Obstet Gynecol*, vol. 77, no. 4, pp. 591–594, Apr. 1991.

[28]   R. Hart, B. G. Molnár, and A. Magos, "Long term follow up of hysteroscopic myomectomy assessed by survival analysis," *BJOG: An International Journal of Obstetrics & Gynaecology*, vol. 106, no. 7, pp. 700–705, 1999, doi: 10.1111/j.1471-0528.1999.tb08370.x.

[29]   P. Gambadauro, J. Gudmundsson, and R. Torrejón, "Intrauterine Adhesions following Conservative Treatment of Uterine Fibroids," *Obstet Gynecol Int*, vol. 2012, 2012, doi: 10.1155/2012/853269.

[30]   L. Torres-De La Roche *et al.*, "Adhesions and Anti-Adhesion Systems Highlights," *Facts Views Vis Obgyn*, vol. 11, no. 2, pp. 137–149.

[31]   M. Bongers *et al.*, "Evaluation of uterine patency following transcervical uterine fibroid ablation with the Sonata system (the OPEN clinical trial)," *European Journal of Obstetrics & Gynecology and Reproductive Biology*, vol. 242, pp. 122–125, Nov. 2019, doi: 10.1016/j.ejogrb.2019.09.013.

[32]   M. Camanni, L. Bonino, E. M. Delpiano, B. Ferrero, G. Migliaretti, and F. Deltetto, "Hysteroscopic Management of Large Symptomatic Submucous Uterine Myomas," *Journal of Minimally Invasive Gynecology*, vol. 17, no. 1, pp. 59–65, Jan. 2010, doi: 10.1016/j.jmig.2009.10.013.

[33]   K. Wamsteker and M. H. Emanuel, "Transcervical hysteroscopic resection of submucous fibroids for abnormal uterine bleeding: results regarding the degree of intramural extension.," *Obstetrics and Gynecology*, vol. 82, no. 5, pp. 736–740, 1993.

[34]   R. B. Lasmar, P. R. M. Barrozo, R. Dias, and M. A. P. de Oliveira, "Submucous myomas: A new presurgical classification to evaluate the viability of hysteroscopic surgical treatment—Preliminary report," *Journal of Minimally Invasive Gynecology*, vol. 12, no. 4, pp. 308–311, Aug. 2005, doi: 10.1016/j.jmig.2005.05.014.

[35]   R. Salim, C. Lee, A. Davies, B. Jolaoso, E. Ofuasia, and D. Jurkovic, "A comparative study of three-dimensional saline infusion sonohysterography and diagnostic hysteroscopy for

the classification of submucous fibroids," *Hum Reprod*, vol. 20, no. 1, pp. 253–257, Jan. 2005, doi: 10.1093/humrep/deh557.

[36]   A. Tinelli *et al.*, "A Combined Ultrasound and Histologic Approach for Analysis of Uterine Fibroid Pseudocapsule Thickness," *Reproductive Sciences*, vol. 21, no. 9, pp. 1177–1186, Sep. 2014, doi: 10.1177/1933719114537719.

[37]   C. L. Brace, "Microwave tissue ablation: biophysics, technology, and applications," *Critical Reviews*^{TM} *in Biomedical Engineering*, vol. 38, no. 1, 2010, Accessed: Oct. 29, 2016. [Online]. Available: http://www.dl.begellhouse.com/journals/4b27cbfc562e21b8,41996af914259394,6941e05 86b165112.html

[38]   K. F. Chu and D. E. Dupuy, "Thermal ablation of tumours: biological mechanisms and advances in therapy," *Nature Reviews Cancer*, vol. 14, no. 3, Art. no. 3, Mar. 2014, doi: 10.1038/nrc3672.

[39]   E. Zupi *et al.*, "Directed laparoscopic cryomyolysis: A possible alternative to myomectomy and/or hysterectomy for symptomatic leiomyomas," *American Journal of Obstetrics and Gynecology*, vol. 190, no. 3, pp. 639–643, Mar. 2004, doi: 10.1016/j.ajog.2003.10.687.

[40]   D. B. Toub, "A New Paradigm for Uterine Fibroid Treatment: Transcervical, Intrauterine Sonography-Guided Radiofrequency Ablation of Uterine Fibroids with the Sonata System," *Curr Obstet Gynecol Rep*, vol. 6, no. 1, pp. 67–73, 2017, doi: 10.1007/s13669-017-0194-2.

[41]   J. Zhang *et al.*, "Ultrasound-guided percutaneous microwave ablation for symptomatic uterine fibroid treatment–a clinical study," *International Journal of Hyperthermia*, vol. 27, no. 5, pp. 510–516, 2011.

[42]   M. Bongers *et al.*, "Correlation of Reductions in Perfused Fibroid Volume With Subsequent Reductions in Total Fibroid Volume After Transcervical Radiofrequency Ablation," *Journal of Minimally Invasive Gynecology*, vol. 22, no. 6, Supplement, pp. S42–S43, Nov. 2015, doi: 10.1016/j.jmig.2015.08.117.

[43]   E. A. Stewart, B. Gostout, J. Rabinovici, H. S. Kim, L. Regan, and C. M. C. Tempany, "Sustained Relief of Leiomyoma Symptoms by Using Focused Ultrasound Surgery," vol. 110, no. 2, p. 9, 2007.

[44]   G. Zia, J. Sebek, E. Alvarez, and P. Prakash, "Assessment of thermal damage to myometrium during microwave ablation of uterine fibroids," in *2020 42nd Annual International Conference of the IEEE Engineering in Medicine Biology Society (EMBC)*, Jul. 2020, pp. 5263–5266. doi: 10.1109/EMBC44109.2020.9176092.

[45]   G. Zia, J. Sebek, J. Schenck, and P. Prakash, "Transcervical microwave ablation in type 2 uterine fibroids via a hysteroscopic approach: analysis of ablation profiles," *Biomed. Phys. Eng. Express*, vol. 7, no. 4, p. 045014, Jun. 2021, doi: 10.1088/2057-1976/abffe4.

[46]   A. M. Ierardi *et al.*, "Uterine Myomas: Extravascular Treatment," *Seminars in Ultrasound, CT and MRI*, vol. 42, no. 1, pp. 56–74, Feb. 2021, doi: 10.1053/j.sult.2020.08.004.

[47]   C. L. Brace, "Radiofrequency and microwave ablation of the liver, lung, kidney, and bone: what are the differences?," *Current problems in diagnostic radiology*, vol. 38, no. 3, pp. 135–143, 2009.

[48]   A. M. Ierardi *et al.*, "Percutaneous High Frequency Microwave Ablation of Uterine Fibroids: Systematic Review," *BioMed Research International*, Jan. 08, 2018. https://www.hindawi.com/journals/bmri/2018/2360107/ (accessed Jul. 20, 2020).

[49]   Y. Kanaoka, C. Yoshida, T. Fukuda, K. Kajitani, and O. Ishiko, "Transcervical microwave myolysis for uterine myomas assisted by transvaginal ultrasonic guidance," *Journal of Obstetrics and Gynaecology Research*, vol. 35, no. 1, pp. 145–151, 2009.

[50]   Y. Kanaoka and H. Imoto, "Transcervical interstitial microwave ablation therapy for the treatment of adenomyosis: A novel alternative to hysterectomy," *Open Journal of Obstetrics and Gynecology*, vol. 4, no. 14, p. 840, 2014.

[51]   A. Tsuda and Y. Kanaoka, "Submyometrial vasopressin injection before microwave ablation of vascular-rich submucosal myomas: a preliminary case study," *International Journal of Hyperthermia*, vol. 36, no. 1, pp. 738–742, 2019.

[52]   A. Tsuda and Y. Kanaoka, "Outpatient transcervical microwave myolysis assisted by transabdominal ultrasonic guidance for menorrhagia caused by submucosal myomas," *International Journal of Hyperthermia*, vol. 31, no. 6, pp. 588–592, 2015.

[53]   Y. Yang *et al.*, "Ultrasound-Guided Percutaneous Microwave Ablation for Submucosal Uterine Fibroids," *Journal of Minimally Invasive Gynecology*, vol. 21, no. 3, pp. 436–441, May 2014, doi: 10.1016/j.jmig.2013.11.012.

[54]   Y. Kanaoka, C. Yoshida, T. Fukuda, K. Kajitani, and O. Ishiko, "Transcervical microwave myolysis for uterine myomas assisted by transvaginal ultrasonic guidance," *Journal of Obstetrics and Gynaecology Research*, vol. 35, no. 1, pp. 145–151, 2009.

[55]   Y. Kanaoka and H. Imoto, "Transcervical Interstitial Microwave Ablation Therapy for the Treatment of Adenomyosis: A Novel Alternative to Hysterectomy," *Open Journal of Obstetrics and Gynecology*, vol. 04, no. 14, pp. 840–845, 2014, doi: 10.4236/ojog.2014.414118.

[56]   A. Tsuda and Y. Kanaoka, "Submyometrial vasopressin injection before microwave ablation of vascular-rich submucosal myomas: a preliminary case study," *Int J Hyperthermia*, vol. 36, no. 1, pp. 739–743, 2019, doi: 10.1080/02656736.2019.1612102.

[57]   A. Tsuda and Y. Kanaoka, "Outpatient transcervical microwave myolysis assisted by transabdominal ultrasonic guidance for menorrhagia caused by submucosal myomas," *Int J Hyperthermia*, vol. 31, no. 6, pp. 588–592, 2015, doi: 10.3109/02656736.2015.1036385.

[58]   BruceBlaus, *English: Hysteroscopy. This image was donated by Blausen Medical. Please visit our website to see more medical illustrations and animations.* 2015. Accessed: Oct. 14, 2021. [Online]. Available: https://commons.wikimedia.org/wiki/File:Hysteroscopy.png

[59]   M. Lazebnik, M. C. Converse, J. H. Booske, and S. C. Hagness, "Ultrawideband temperature-dependent dielectric properties of animal liver tissue in the microwave frequency range," *Phys Med Biol*, vol. 51, no. 7, pp. 1941–1955, Apr. 2006, doi: 10.1088/0031-9155/51/7/022.

[60]   S. Gabriel, R. W. Lau, and C. Gabriel, "The dielectric properties of biological tissues: II. Measurements in the frequency range 10 Hz to 20 GHz," *Phys. Med. Biol.*, vol. 41, no. 11, pp. 2251–2269, Nov. 1996, doi: 10.1088/0031-9155/41/11/002.

[61]   C. Gabriel, S. Gabriel, E. H. Grant, E. H. Grant, B. S. J. Halstead, and D. Michael P. Mingos, "Dielectric parameters relevant to microwave dielectric heating," *Chem. Soc. Rev.*, vol. 27, no. 3, p. 213, 1998, doi: 10.1039/a827213z.

[62]   P. R. Stauffer, F. Rossetto, M. Prakash, D. G. Neuman, and T. Lee, "Phantom and animal tissues for modelling the electrical properties of human liver," *Int J Hyperthermia*, vol. 19, no. 1, pp. 89–101, Feb. 2003, doi: 10.1080/0265673021000017064.

[63]   J. Sebek, R. Bortel, and P. Prakash, "Broadband lung dielectric properties over the ablative temperature range: Experimental measurements and parametric models," *Medical Physics*, vol. 46, no. 10, pp. 4291–4303, 2019, doi: 10.1002/mp.13704.

[64]   H. Fallahi, J. Sebek, and P. Prakash, "Broadband Dielectric Properties of Ex Vivo Bovine Liver Tissue Characterized at Ablative Temperatures," *IEEE Transactions on Biomedical Engineering*, vol. 68, no. 1, pp. 90–98, Jan. 2021, doi: 10.1109/TBME.2020.2996825.

[65]   J. G. Garza-Leal *et al.*, "Transcervical, intrauterine ultrasound-guided radiofrequency ablation of uterine fibroids with the VizAblate System: safety, tolerability, and ablation results in a closed abdomen setting," *Gynecological Surgery*, vol. 8, no. 3, pp. 327–334, Sep. 2011, doi: 10.1007/s10397-010-0655-3.

[66]   Q. Duan *et al.*, "Characterization of a dielectric phantom for high-field magnetic resonance imaging applications," *Med Phys*, vol. 41, no. 10, p. 102303, Oct. 2014, doi: 10.1118/1.4895823.

[67]   C. Rossmann and D. Haemmerich, "Review of temperature dependence of thermal properties, dielectric properties, and perfusion of biological tissues at hyperthermic and ablation temperatures," *Crit Rev Biomed Eng*, vol. 42, no. 6, pp. 467–492, 2014.

[68]   J. A. Pearce, "Comparative analysis of mathematical models of cell death and thermal damage processes," *Int J Hyperthermia*, vol. 29, no. 4, pp. 262–280, Jun. 2013, doi: 10.3109/02656736.2013.786140.

[69]   N. McDannold *et al.*, "Uterine Leiomyomas: MR Imaging– based Thermometry and Thermal Dosimetry during Focused Ultrasound Thermal Ablation," *Radiology*, vol. 240, no. 1, pp. 263–272, Jul. 2006, doi: 10.1148/radiol.2401050717.

[70]   P. S. Yarmolenko *et al.*, "Thresholds for thermal damage to normal tissues: An update," *International Journal of Hyperthermia*, vol. 27, no. 4, pp. 320–343, Jun. 2011, doi: 10.3109/02656736.2010.534527.

[71]   J. Donnez, "Laparoscopic myolysis," *Human Reproduction Update*, vol. 6, no. 6, pp. 609–613, Nov. 2000, doi: 10.1093/humupd/6.6.609.

[72]   B. B. Lee and S. P. Yu, "Radiofrequency Ablation of Uterine Fibroids: a Review," *Curr Obstet Gynecol Rep*, vol. 5, no. 4, pp. 318–324, Dec. 2016, doi: 10.1007/s13669-016-0183-x.

[73]   D. D. Rattray, L. Weins, L. C. Regush, J. M. Bowen, D. O'Reilly, and J. A. Thiel, "Clinical outcomes and health care utilization pre- and post-laparoscopic radiofrequency ablation of symptomatic fibroids and laparoscopic myomectomy: a randomized trial of uterine-sparing techniques (TRUST) in Canada," *Clinicoecon Outcomes Res*, vol. 10, pp. 201–212, Apr. 2018, doi: 10.2147/CEOR.S155038.

[74]   S. Yu, K. Silverberg, B. Bhagavath, S. A. Shobeiri, A. Propst, and D. Eisenstein, "Post-Market Safety of Laparoscopic Ultrasound-Guided Radiofrequency Ablation," *JSLS*, vol. 24, no. 4, 2020, doi: 10.4293/JSLS.2020.00050.

[75]   S. Y. Brucker, M. Hahn, D. Kraemer, F. A. Taran, K. B. Isaacson, and B. Krämer, "Laparoscopic radiofrequency volumetric thermal ablation of fibroids versus laparoscopic myomectomy," *International Journal of Gynecology & Obstetrics*, vol. 125, no. 3, pp. 261–265, Jun. 2014, doi: 10.1016/j.ijgo.2013.11.012.

[76]   A. Al-Hendy and S. Salama, Eds., *Leiomyomas: risk factors, clinical manifestations and treatment options*. New York: Nova Biomedical, 2015.

[77]   S. G. Chudnoff, J. M. Berman, D. J. Levine, M. Harris, R. S. Guido, and E. Banks, "Outpatient procedure for the treatment and relief of symptomatic uterine myomas," *Obstet Gynecol*, vol. 121, no. 5, pp. 1075–1082, May 2013, doi: 10.1097/AOG.0b013e31828b7962.

[78]   C. Våpenstad *et al.*, "Laparoscopic ultrasound: A survey of its current and future use, requirements, and integration with navigation technology," *Surgical endoscopy*, vol. 24, pp. 2944–53, Dec. 2010, doi: 10.1007/s00464-010-1135-6.

[79]   R. Santambrogio, E. Opocher, M. Costa, A. Cappellani, and M. Montorsi, "Survival and intra-hepatic recurrences after laparoscopic radiofrequency of hepatocellular carcinoma in patients with liver cirrhosis," *J Surg Oncol*, vol. 89, no. 4, pp. 218–225; discussion 225-226, Mar. 2005, doi: 10.1002/jso.20204.

[80]   A. M. Silas, J. B. Kruskal, and R. A. Kane, "INTRAOPERATIVE ULTRASOUND," *Radiologic Clinics of North America*, vol. 39, no. 3, pp. 429–448, May 2001, doi: 10.1016/S0033-8389(05)70290-6.

[81]   R. Angioli *et al.*, "Intraoperative contact ultrasonography during open myomectomy for uterine fibroids," *Fertility and Sterility*, vol. 94, no. 4, pp. 1487–1490, Sep. 2010, doi: 10.1016/j.fertnstert.2009.08.015.

[82]   P. C. Lin, A. Thyer, and M. R. Soules, "Intraoperative ultrasound during a laparoscopic myomectomy," *Fertility and Sterility*, vol. 81, no. 6, pp. 1671–1674, Jun. 2004, doi: 10.1016/j.fertnstert.2003.10.049.

[83]   B. D. Schirmer, *Intra-operative and laparoscopic ultrasound*. Zuckschwerdt, 2001. Accessed: Sep. 08, 2021. [Online]. Available: https://www.ncbi.nlm.nih.gov/books/NBK6975/

[84]   V. Bergamini *et al.*, "Laparoscopic radiofrequency thermal ablation: A new approach to symptomatic uterine myomas," *American Journal of Obstetrics and Gynecology*, vol. 192, no. 3, pp. 768–773, Mar. 2005, doi: 10.1016/j.ajog.2004.10.591.

[85]   K. M. Braun *et al.*, "Surgeons' early experience with the Acessa[TM] procedure: gaining proficiency with new technology," *Int J Womens Health*, vol. 8, pp. 669–675, Nov. 2016, doi: 10.2147/IJWH.S119265.

[86]   R. García-Marcos *et al.*, "Percutaneous Ultrasound-Guided Radiofrequency Thermal Ablation for Treatment of Uterine Fibroids," *Open Journal of Obstetrics and Gynecology*, vol. 04, pp. 716–724, Jan. 2014, doi: 10.4236/ojog.2014.412100.

[87]   P. Law, W. M. W. Gedroyc, and L. Regan, "Magnetic resonance-guided percutaneous laser ablation of uterine fibroids," *Journal of Magnetic Resonance Imaging*, vol. 12, no. 4, pp. 565–570, 2000, doi: https://doi.org/10.1002/1522-2586(200010)12:4<565::AID-JMRI8>3.0.CO;2-4.

[88]   Y. Yang *et al.*, "Ultrasound-Guided Percutaneous Microwave Ablation for Subserosal Uterine Myomas," *Journal of Minimally Invasive Gynecology*, vol. 26, no. 3, pp. 544–550, Mar. 2019, doi: 10.1016/j.jmig.2018.06.014.

[89]   C. Recaldini *et al.*, "Percutaneous Sonographically Guided Radiofrequency Ablation of Medium-Sized Fibroids: Feasibility Study," *American Journal of Roentgenology*, vol. 189, no. 6, pp. 1303–1306, Dec. 2007, doi: 10.2214/AJR.07.2184.

[90]   F. Wang *et al.*, "Imaging manifestation of conventional and contrast-enhanced ultrasonography in percutaneous microwave ablation for the treatment of uterine fibroids," *European Journal of Radiology*, vol. 81, no. 11, pp. 2947–2952, Nov. 2012, doi: 10.1016/j.ejrad.2011.12.037.

[91]   A. M. Ierardi *et al.*, "Percutaneous microwave ablation of uterine fibroids: correlation between shrinkage and trend symptoms," *Minimally Invasive Therapy & Allied Technologies*, pp. 1–7, Sep. 2019, doi: 10.1080/13645706.2019.1668417.

[92]   G. Yüce, A. Tayarer, H. L. Keskin, B. Genc, and M. Canyigit, "Ultrasound guided percutaneous radiofrequency thermal ablation of symptomatic uterine fibroids — results from a single center and 52 weeks of follow up," *Ginekologia Polska*, vol. 91, no. 8, Art. no. 8, 2020, doi: 10.5603/GP.2020.0074.

[93]   W.-P. Zhao, Z.-Y. Han, J. Zhang, and P. Liang, "A retrospective comparison of microwave ablation and high intensity focused ultrasound for treating symptomatic uterine fibroids," *European Journal of Radiology*, vol. 84, no. 3, pp. 413–417, Mar. 2015, doi: 10.1016/j.ejrad.2014.11.041.

[94]   G. Shifrin, M. Engelhardt, P. Gee, and G. Pschadka, "Transcervical fibroid ablation with the Sonata® system for treatment of submucous and large uterine fibroids," *International Journal of Gynecology & Obstetrics*, vol. n/a, no. n/a, doi: https://doi.org/10.1002/ijgo.13638.

[95]   M. Bongers, H. Brölmann, J. Gupta, J. G. Garza-Leal, and D. Toub, "Transcervical, intrauterine ultrasound-guided radiofrequency ablation of uterine fibroids with the VizAblate® System: three- and six-month endpoint results from the FAST-EU study," *Gynecol Surg*, vol. 12, no. 1, pp. 61–70, 2015, doi: 10.1007/s10397-014-0873-1.

[96]   "AAGL Practice Report: Practice Guidelines for the Management of Hysteroscopic Distending Media," *Journal of Minimally Invasive Gynecology*, vol. 20, no. 2, pp. 137–148, Mar. 2013, doi: 10.1016/j.jmig.2012.12.002.

[97]   E. Mazza, A. Nava, M. Bauer, R. Winter, M. Bajka, and G. A. Holzapfel, "Mechanical properties of the human uterine cervix: An in vivo study," *Medical Image Analysis*, vol. 10, no. 2, pp. 125–136, Apr. 2006, doi: 10.1016/j.media.2005.06.001.

[98]   S. Chudnoff, R. Guido, K. Roy, D. Levine, L. Mihalov, and J. G. Garza-Leal, "Ultrasound-Guided Transcervical Ablation of Uterine Leiomyomas," *Obstetrics & Gynecology*, vol. 133, no. 1, pp. 13–22, Jan. 2019, doi: 10.1097/AOG.0000000000003032.

[99]   M. H. Emanuel, "Hysteroscopy and the treatment of uterine fibroids," *Best Practice & Research Clinical Obstetrics & Gynaecology*, vol. 29, no. 7, pp. 920–929, Oct. 2015, doi: 10.1016/j.bpobgyn.2015.03.014.

[100] H. Brölmann *et al.*, "The FAST-EU trial: 12-month clinical outcomes of women after intrauterine sonography-guided transcervical radiofrequency ablation of uterine fibroids," *Gynecol Surg*, vol. 13, pp. 27–35, 2016, doi: 10.1007/s10397-015-0915-3.

[101] J. Donnez, S. Gillerot, D. Bourgonjon, F. Clerckx, and M. Nisolle, "Neodymium:YAG laser hysteroscopy in large submucous fibroids," *Fertility and Sterility*, vol. 54, no. 6, pp. 999–1003, Dec. 1990, doi: 10.1016/S0015-0282(16)53994-6.

[102] M. Nisolle, M. Smets, V. Malvaux, V. Anaf, and J. Donnez, "Laparoscopic Myolysis with the Nd:YAG Laser," *Journal of Gynecologic Surgery*, vol. 9, no. 2, pp. 95–99, Jan. 1993, doi: 10.1089/gyn.1993.9.95.

[103] L. Carroll and T. R. Humphreys, "LASER-tissue interactions," *Clinics in Dermatology*, vol. 24, no. 1, pp. 2–7, Jan. 2006, doi: 10.1016/j.clindermatol.2005.10.019.

[104] S. Parker, "Laser-tissue interaction," *British Dental Journal*, vol. 202, no. 2, Art. no. 2, Jan. 2007, doi: 10.1038/bdj.2007.24.

[105] A. J. Welch, J. H. Torres, and W.-F. Cheong, "Laser Physics and Laser-Tissue Interaction," *Tex Heart Inst J*, vol. 16, no. 3, pp. 141–149, 1989.

[106] G. J. Müller and A. Roggan, *Laser-induced Interstitial Thermotherapy*. SPIE Press, 1995.

[107] E. Schena, P. Saccomandi, and Y. Fong, "Laser Ablation for Cancer: Past, Present and Future," *J Funct Biomater*, vol. 8, no. 2, Jun. 2017, doi: 10.3390/jfb8020019.

[108] N. Bhatta, K. Isaacson, K. M. Bhatta, R. R. Anderson, and I. Schiff, "Comparative study of different laser systems," *Fertility and Sterility*, vol. 61, no. 4, pp. 581–591, Apr. 1994, doi: 10.1016/S0015-0282(16)56629-1.

[109] J. Heisterkamp, R. van Hillegersberg, and J. N. M. IJzermans, "Interstitial laser coagulation for hepatic tumours," *British Journal of Surgery*, vol. 86, no. 3, pp. 293–304, Mar. 1999, doi: 10.1046/j.1365-2168.1999.01059.x.

[110] A. L. Gough-Palmer and W. M. W. Gedroyc, "Laser ablation of hepatocellular carcinoma-A review," *World J Gastroenterol*, vol. 14, no. 47, pp. 7170–7174, Dec. 2008, doi: 10.3748/wjg.14.7170.

[111] P. Tombesi, F. D. Vece, and S. Sartori, "Radiofrequency, microwave, and laser ablation of liver tumors: time to move toward a tailored ablation technique?," *Hepatoma Research*, vol. 1, pp. 52–57, Jul. 2015, doi: 10.4103/2394-5079.155697.

[112] M. F. Marqa, S. Mordon, and N. Betrouni, "Laser interstitial thermotherapy of small breast fibroadenomas: Numerical simulations," *Lasers in Surgery and Medicine*, vol. 44, no. 10, pp. 832–839, 2012, doi: 10.1002/lsm.22097.

[113] H. A. Goldfarb, "Nd:YAG laser laparoscopic coagulation of symptomatic myomas," *J Reprod Med*, vol. 37, no. 7, pp. 636–638, Jul. 1992.

[114] H. A. Goldfarb, "LAPAROSCOPIC COAGULATION OF MYOMA (MYOLYSIS)," *Obstetrics and Gynecology Clinics of North America*, vol. 22, no. 4, pp. 807–819, Dec. 1995, doi: 10.1016/S0889-8545(21)00667-7.

[115] J. T. Hindley, "Clinical outcomes following percutaneous magnetic resonance image guided laser ablation of symptomatic uterine fibroids," *Human Reproduction*, vol. 17, no. 10, pp. 2737–2741, Oct. 2002, doi: 10.1093/humrep/17.10.2737.

[116] D. Visvanathan, R. Connell, M. A. Hall-Craggs, A. S. Cutner, and S. G. Bown, "Interstitial laser photocoagulation for uterine myomas," *American Journal of Obstetrics and Gynecology*, vol. 187, no. 2, pp. 382–384, Aug. 2002, doi: 10.1067/mob.2002.123892.

[117] P. Law and L. Regan, "Interstitial thermo-ablation under MRI guidance for the treatment of fibroids," *Current Opinion in Obstetrics and Gynecology*, vol. 12, no. 4, pp. 277–282, Aug. 2000.

[118] R. Chapman, "Low power interstitial photocoagulation of uterine leiomyomas by KTP/YAG laser," *Laser Med Sci*, vol. 9, no. 1, pp. 37–46, Mar. 1994, doi: 10.1007/BF02594183.

[119] R. Chapman, "Percutaneous laser-induced interstitial thermotherapy (LITT) for the treatment of very large uterine leiomyomas," in *Lasers in Surgery: Advanced Characterization, Therapeutics, and Systems VII*, May 1997, vol. 2970, pp. 561–568. doi: 10.1117/12.275091.

[120] S. Sartori, F. Di Vece, F. Ermili, and P. Tombesi, "Laser ablation of liver tumors: An ancillary technique, or an alternative to radiofrequency and microwave?," *World Journal of Radiology*, vol. 9, p. 91, Mar. 2017, doi: 10.4329/wjr.v9.i3.91.

[121] S. D. Quinn and W. M. Gedroyc, "Thermal ablative treatment of uterine fibroids," *International Journal of Hyperthermia*, vol. 31, no. 3, pp. 272–279, Apr. 2015, doi: 10.3109/02656736.2015.1010608.

[122] S. Jones, P. O'Donovan, and D. Toub, "Radiofrequency Ablation for Treatment of Symptomatic Uterine Fibroids," *Obstetrics and Gynecology International*, 2012. https://www.hindawi.com/journals/ogi/2012/194839/abs/ (accessed Aug. 19, 2019).

[123] M. Taheri, L. Galo, C. Potts, K. Sakhel, and S. D. Quinn, "Nonresective treatments for uterine fibroids: a systematic review of uterine and fibroid volume reductions," *International Journal of Hyperthermia*, vol. 36, no. 1, pp. 294–300, Jan. 2019, doi: 10.1080/02656736.2018.1564843.

[124] D. Haemmerich, "Biophysics of Radiofrequency Ablation," *Crit Rev Biomed Eng*, vol. 38, no. 1, pp. 53–63, 2010, doi: 10.1615/CritRevBiomedEng.v38.i1.50.

[125] W. Schramm, D. Yang, and D. Haemmerich, "Contribution of Direct Heating, Thermal Conduction and Perfusion during Radiofrequency and Microwave Ablation," in *2006 International Conference of the IEEE Engineering in Medicine and Biology Society*, Aug. 2006, pp. 5013–5016. doi: 10.1109/IEMBS.2006.259288.

[126] S. K. Hall, E. H. Ooi, and S. J. Payne, "Cell death, perfusion and electrical parameters are critical in models of hepatic radiofrequency ablation," *International Journal of Hyperthermia*, vol. 31, no. 5, pp. 538–550, Jul. 2015, doi: 10.3109/02656736.2015.1032370.

[127] H. A. Goldfarb, "Bipolar laparoscopic needles for myoma coagulation," *The Journal of the American Association of Gynecologic Laparoscopists*, vol. 2, no. 2, pp. 175–179, Feb. 1995, doi: 10.1016/S1074-3804(05)80013-1.

[128] B. B. Lee, "Radiofrequency Ablation of Uterine Leiomyomata: A New Minimally Invasive Hysterectomy Alternative," *Obstetrics & Gynecology*, vol. 99, no. 4, p. 9S, Apr. 2002.

[129] D. I. Galen, K. B. Isaacson, and B. B. Lee, "Does menstrual bleeding decrease after ablation of intramural myomas? A retrospective study," *J Minim Invasive Gynecol*, vol. 20, no. 6, pp. 830–835, Dec. 2013, doi: 10.1016/j.jmig.2013.05.007.

[130] C. Arnreiter and P. Oppelt, "A Systematic Review of the Treatment of Uterine Myomas Using Transcervical Ultrasound-Guided Radiofrequency Ablation with the Sonata System," *Journal of Minimally Invasive Gynecology*, Apr. 2021, doi: 10.1016/j.jmig.2021.04.009.

[131] C. L. Brace, "Microwave Ablation Technology: What Every User Should Know," *Current Problems in Diagnostic Radiology*, vol. 38, no. 2, pp. 61–67, Mar. 2009, doi: 10.1067/j.cpradiol.2007.08.011.

[132] H. Fallahi and P. Prakash, "Antenna Designs for Microwave Tissue Ablation," *CRB*, vol. 46, no. 6, 2018, doi: 10.1615/CritRevBiomedEng.2018028554.

[133] 42] M. Kuang, "Liver Cancer: Increased Microwave Delivery to Ablation Zone with Cooled-Shaft Antenna—Experimental and Clinical Studies 1," *Radiology*, vol. 242, no. 3, pp. 914–924, 2007.

[134] C. L. Brace, "Microwave Tissue Ablation: Biophysics, Technology, and Applications," *CRB*, vol. 38, no. 1, 2010, doi: 10.1615/CritRevBiomedEng.v38.i1.60.

[135] H. Fallahi, J. Sebek, and P. Prakash, "Broadband Dielectric Properties of Ex Vivo Bovine Liver Tissue Characterized at Ablative Temperatures," *IEEE Transactions on Biomedical Engineering*, pp. 1–1, 2020, doi: 10.1109/TBME.2020.2996825.

[136] M. Xia *et al.*, "Research of dose-effect relationship parameters of percutaneous microwave ablation for uterine leiomyomas - a quantitative study," *Sci Rep*, vol. 4, no. 1, p. 6469, Sep. 2014, doi: 10.1038/srep06469.

[137] M. Xia *et al.*, "Feasibility study on energy prediction of microwave ablation upon uterine adenomyosis and leiomyomas by MRI," *Br J Radiol*, vol. 87, no. 1040, p. 20130770, Aug. 2014, doi: 10.1259/bjr.20130770.

[138] H. Liu *et al.*, "Effectiveness of ultrasound-guided percutaneous microwave ablation for symptomatic uterine fibroids: a multicentre study in China," *International Journal of Hyperthermia*, vol. 32, no. 8, pp. 876–880, Nov. 2016, doi: 10.1080/02656736.2016.1212276.

[139] A. M. Ierardi *et al.*, "Percutaneous High Frequency Microwave Ablation of Uterine Fibroids: Systematic Review," *BioMed Research International*, vol. 2018, pp. 1–9, 2018, doi: 10.1155/2018/2360107.

[140] J. Zhang *et al.*, "Ultrasound-guided percutaneous microwave ablation for symptomatic uterine fibroid treatment – A clinical study," *International Journal of Hyperthermia*, vol. 27, no. 5, pp. 510–516, Aug. 2011, doi: 10.3109/02656736.2011.562872.

[141] A. M. Ierardi *et al.*, "Percutaneous High Frequency Microwave Ablation of Uterine Fibroids: Systematic Review," *BioMed Research International*, Jan. 08, 2018. https://www.hindawi.com/journals/bmri/2018/2360107/ (accessed Aug. 11, 2020).

[142] M. G. Munro, H. O. D. Critchley, M. S. Broder, and I. S. Fraser, "FIGO classification system (PALM-COEIN) for causes of abnormal uterine bleeding in nongravid women of reproductive age," *International Journal of Gynecology & Obstetrics*, vol. 113, no. 1, pp. 3–13, 2011, doi: 10.1016/j.ijgo.2010.11.011.

[143] M. G. Munro, H. O. D. Critchley, and I. S. Fraser, "The FIGO classification of causes of abnormal uterine bleeding in the reproductive years," *Fertility and Sterility*, vol. 95, no. 7, pp. 2204-2208.e3, Jun. 2011, doi: 10.1016/j.fertnstert.2011.03.079.

[144] J. T. Hindley *et al.*, "Clinical outcomes following percutaneous magnetic resonance image guided laser ablation of symptomatic uterine fibroids," *Human Reproduction*, vol. 17, no. 10, pp. 2737–2741, Oct. 2002, doi: 10.1093/humrep/17.10.2737.

[145] J. Donnez, S. Gillerot, D. Bourgonjon, F. Clerckx, and M. Nisolle, "Neodymium:YAG laser hysteroscopy in large submucous fibroids," *Fertility and Sterility*, vol. 54, no. 6, pp. 999–1003, Dec. 1990, doi: 10.1016/S0015-0282(16)53994-6.

[146] L. Zhang, W. Zhang, F. Orsi, W. Chen, and Z. Wang, "Ultrasound-guided high intensity focused ultrasound for the treatment of gynaecological diseases: A review of safety and efficacy," *International Journal of Hyperthermia*, vol. 31, no. 3, pp. 280–284, Apr. 2015, doi: 10.3109/02656736.2014.996790.

[147] S.-W. Yoon, S. H. Cha, Y. G. Ji, H. C. Kim, M. H. Lee, and J. H. Cho, "Magnetic resonance imaging-guided focused ultrasound surgery for symptomatic uterine fibroids: estimation of treatment efficacy using thermal dose calculations," *European Journal of Obstetrics & Gynecology and Reproductive Biology*, vol. 169, no. 2, pp. 304–308, Jul. 2013, doi: 10.1016/j.ejogrb.2013.02.023.

[148] E. A. Stewart, "Uterine Fibroids," *New England Journal of Medicine*, vol. 372, no. 17, pp. 1646–1655, Apr. 2015, doi: 10.1056/NEJMcp1411029.

[149] M. S. Islam, A. Ciavattini, F. Petraglia, M. Castellucci, and P. Ciarmela, "Extracellular matrix in uterine leiomyoma pathogenesis: a potential target for future therapeutics," *Human Reproduction Update*, vol. 24, no. 1, pp. 59–85, Jan. 2018, doi: 10.1093/humupd/dmx032.

[150] H. Ueda *et al.*, "Unusual Appearances of Uterine Leiomyomas: MR Imaging Findings and Their Histopathologic Backgrounds," *RadioGraphics*, vol. 19, no. suppl_1, pp. S131–S145, Oct. 1999, doi: 10.1148/radiographics.19.suppl_1.g99oc04s131.

[151] Hasgall PA *et al.*, "IT'IS Database for thermal and electromagnetic parameters of biological tissues." IT'IS Foundation, May 15, 2018. doi: 10.13099/VIP21000-04-0.

[152] R. DeLonzor, R. K. Spero, and J. J. Williams, "The electrical conductivity of in vivo human uterine fibroids," *International Journal of Hyperthermia*, vol. 27, no. 3, pp. 255–265, May 2011, doi: 10.3109/02656736.2011.555875.

[153] S. Etoz and C. L. Brace, "Analysis of microwave ablation antenna optimization techniques," *International Journal of RF and Microwave Computer-Aided Engineering*, vol. 28, no. 3, p. e21224, 2018, doi: 10.1002/mmce.21224.

[154] Z. Ji and C. L. Brace, "Expanded modeling of temperature-dependent dielectric properties for microwave thermal ablation," *Phys Med Biol*, vol. 56, no. 16, pp. 5249–5264, Aug. 2011, doi: 10.1088/0031-9155/56/16/011.

[155] A. La Gioia *et al.*, "Open-Ended Coaxial Probe Technique for Dielectric Measurement of Biological Tissues: Challenges and Common Practices," *Diagnostics (Basel)*, vol. 8, no. 2, Jun. 2018, doi: 10.3390/diagnostics8020040.

[156] A. Gregory and R. Clarke, *Tables of the complex permittivity of dielectric reference liquids at frequencies up to 5 GHz*. 2012.

[157] J. M. Anderson, C. L. Sibbald, and S. S. Stuchly, "Dielectric measurements using a rational function model," *IEEE Transactions on Microwave Theory and Techniques*, vol. 42, no. 2, pp. 199–204, Feb. 1994, doi: 10.1109/22.275247.

[158] D. Popovic *et al.*, "Precision open-ended coaxial probes for in vivo and ex vivo dielectric spectroscopy of biological tissues at microwave frequencies," *IEEE Transactions on Microwave Theory and Techniques*, vol. 53, no. 5, pp. 1713–1722, May 2005, doi: 10.1109/TMTT.2005.847111.

[159] A. Mirbeik-Sabzevari and N. Tavassolian, "Characterization and Validation of the Slim-Form Open-Ended Coaxial Probe for the Dielectric Characterization of Biological Tissues at Millimeter-Wave Frequencies," *IEEE Microwave and Wireless Components Letters*, vol. 28, no. 1, pp. 85–87, Jan. 2018, doi: 10.1109/LMWC.2017.2772187.

[160] G. Deshazer, D. Merck, M. Hagmann, D. E. Dupuy, and P. Prakash, "Physical modeling of microwave ablation zone clinical margin variance," *Medical Physics*, vol. 43, no. 4, pp. 1764–1776, 2016, doi: 10.1118/1.4942980.

[161] J. G. Garza-Leal *et al.*, "Transcervical, intrauterine ultrasound-guided radiofrequency ablation of uterine fibroids with the VizAblate System: safety, tolerability, and ablation results in a closed abdomen setting," *Gynecol Surg*, vol. 8, no. 3, pp. 327–334, Sep. 2011, doi: 10.1007/s10397-010-0655-3.

[162] J. Chiang, P. Wang, and C. L. Brace, "'Computational Modelling of Microwave Tumour Ablations,'" *Int J Hyperthermia*, vol. 29, no. 4, pp. 308–317, Jun. 2013, doi: 10.3109/02656736.2013.799295.

[163] A. J. Welch, J. H. Torres, and W.-F. Cheong, "Laser Physics and Laser-Tissue Interaction," *Tex Heart Inst J*, vol. 16, no. 3, pp. 141–149, 1989.

[164] A. J. Welch, M. Motamedi, S. Rastegar, G. L. LeCarpentier, and D. Jansen, "Laser Thermal Ablation," *Photochemistry and Photobiology*, vol. 53, no. 6, pp. 815–823, 1991, doi: 10.1111/j.1751-1097.1991.tb09896.x.

[165] G. Deshazer, P. Prakash, D. Merck, and D. Haemmerich, "Experimental measurement of microwave ablation heating pattern and comparison to computer simulations," *International Journal of Hyperthermia*, vol. 33, no. 1, pp. 74–82, Jan. 2017, doi: 10.1080/02656736.2016.1206630.

[166] V. Lopresto, R. Pinto, G. A. Lovisolo, and M. Cavagnaro, "Changes in the dielectric properties of ex vivo bovine liver during microwave thermal ablation at 2.45 GHz," *Phys Med Biol*, vol. 57, no. 8, pp. 2309–2327, Apr. 2012, doi: 10.1088/0031-9155/57/8/2309.

[167] A. Martellosio *et al.*, "Dielectric Properties Characterization From 0.5 to 50 GHz of Breast Cancer Tissues," *IEEE Transactions on Microwave Theory and Techniques*, vol. 65, no. 3, pp. 998–1011, Mar. 2017, doi: 10.1109/TMTT.2016.2631162.

[168] A. P. O'Rourke *et al.*, "Dielectric properties of human normal, malignant and cirrhotic liver tissue: *in vivo* and *ex vivo* measurements from 0.5 to 20 GHz using a precision open-ended coaxial probe," *Phys. Med. Biol.*, vol. 52, no. 15, pp. 4707–4719, Aug. 2007, doi: 10.1088/0031-9155/52/15/022.

[169] A. Fornes-Leal, C. Garcia-Pardo, M. Frasson, V. Pons Beltrán, and N. Cardona, "Dielectric characterization of healthy and malignant colon tissues in the 0.5–18 GHz frequency band," *Phys. Med. Biol.*, vol. 61, no. 20, pp. 7334–7346, Oct. 2016, doi: 10.1088/0031-9155/61/20/7334.

[170] V. Lopresto, R. Pinto, and M. Cavagnaro, "Experimental characterisation of the thermal lesion induced by microwave ablation," *International Journal of Hyperthermia*, vol. 30, no. 2, pp. 110–118, Mar. 2014, doi: 10.3109/02656736.2013.879744.

[171] S. Etoz and C. L. Brace, "Computed Tomography-Based Modeling of Water Vapor-Induced Changes in Permittivity During Microwave Ablation," *IEEE Transactions on Biomedical Engineering*, vol. 67, no. 9, pp. 2427–2433, Sep. 2020, doi: 10.1109/TBME.2019.2962363.

[172] J. Bonello, M. A. Elahi, E. Porter, M. O'Hollaran, L. Farrugia, and C. V. Sammut, "An investigation of the variation of dielectric properties of ovine lung tissue with temperature," *Biomed. Phys. Eng. Express*, vol. 5, no. 4, p. 045024, Jun. 2019, doi: 10.1088/2057-1976/aaee40.

[173] "Accurate in vivo dielectric properties of liver from 500 MHz to 40 GHz and their correlation to ex vivo measurements: Electromagnetic Biology and Medicine: Vol 35, No 4."
https://www.tandfonline.com/doi/abs/10.3109/15368378.2015.1120221?journalCode=ieb m20 (accessed Jul. 16, 2021).

[174] D. A. Pollacco, L. Farina, P. S. Wismayer, L. Farrugia, and C. V. Sammut, "Characterization of the dielectric properties of biological tissues and their correlation to tissue hydration," *IEEE Transactions on Dielectrics and Electrical Insulation*, vol. 25, no. 6, pp. 2191–2197, Dec. 2018, doi: 10.1109/TDEI.2018.007346.

[175] S. Labonte, A. Blais, S. R. Legault, H. O. Ali, and L. Roy, "Monopole antennas for microwave catheter ablation," *IEEE Transactions on Microwave Theory and Techniques*, vol. 44, no. 10, pp. 1832–1840, Oct. 1996, doi: 10.1109/22.539941.

[176] W. Hurter, F. Reinbold, and W. J. Lorenz, "A dipole antenna for interstitial microwave hyperthermia," *IEEE Transactions on Microwave Theory and Techniques*, vol. 39, no. 6, pp. 1048–1054, Jun. 1991, doi: 10.1109/22.81680.

[177] L. Hamada, K. Saito, H. Yoshimura, and K. Ito, "Dielectric-loaded coaxial-slot antenna for interstitial microwave hyperthermia: longitudinal control of heating patterns," *Int J Hyperthermia*, vol. 16, no. 3, pp. 219–229, Jun. 2000, doi: 10.1080/026567300285240.

[178] A. Dabbagh, B. J. J. Abdullah, C. Ramasindarum, and N. H. Abu Kasim, "Tissue-Mimicking Gel Phantoms for Thermal Therapy Studies," *Ultrason Imaging*, vol. 36, no. 4, pp. 291–316, Oct. 2014, doi: 10.1177/0161734614526372.

[179] A. Eranki, A. S. Mikhail, A. H. Negussie, P. S. Katti, B. J. Wood, and A. Partanen, "Tissue-mimicking thermochromic phantom for characterization of HIFU devices and applications," *International Journal of Hyperthermia*, vol. 36, no. 1, pp. 517–528, Jan. 2019, doi: 10.1080/02656736.2019.1605458.

[180] M. McDonald, S. Lochhead, R. Chopra, and M. J. Bronskill, "Multi-modality tissue-mimicking phantom for thermal therapy," *Phys. Med. Biol.*, vol. 49, no. 13, pp. 2767–2778, Jun. 2004, doi: 10.1088/0031-9155/49/13/001.

[181] M. Lazebnik, E. L. Madsen, G. R. Frank, and S. C. Hagness, "Tissue-mimicking phantom materials for narrowband and ultrawideband microwave applications," *Physics in Medicine and Biology*, vol. 50, no. 18, pp. 4245–4258, Sep. 2005, doi: 10.1088/0031-9155/50/18/001.

[182] A. H. Negussie *et al.*, "Thermochromic tissue-mimicking phantom for optimisation of thermal tumour ablation," *International Journal of Hyperthermia*, vol. 32, no. 3, pp. 239–243, Apr. 2016, doi: 10.3109/02656736.2016.1145745.

[183] R. K. Chen and A. J. Shih, "Multi-modality gellan gum-based tissue-mimicking phantom with targeted mechanical, electrical, and thermal properties," *Phys. Med. Biol.*, vol. 58, no. 16, pp. 5511–5525, Jul. 2013, doi: 10.1088/0031-9155/58/16/5511.

[184] A. S. Mikhail, A. H. Negussie, C. Graham, M. Mathew, B. J. Wood, and A. Partanen, "Evaluation of a tissue-mimicking thermochromic phantom for radiofrequency ablation," *Med Phys*, vol. 43, no. 7, pp. 4304–4311, Jul. 2016, doi: 10.1118/1.4953394.

[185] G. Rajeshkumar, R. Vishnupriyan, and S. Selvadeepak, "Tissue Mimicking Material an Idealized Tissue Model for Clinical Applications: A Review," *Materials Today: Proceedings*, vol. 22, pp. 2696–2703, Jan. 2020, doi: 10.1016/j.matpr.2020.03.400.

[186] Y. Yuan *et al.*, "A heterogeneous human tissue mimicking phantom for RF heating and MRI thermal monitoring verification," *Phys. Med. Biol.*, vol. 57, no. 7, pp. 2021–2037, Mar. 2012, doi: 10.1088/0031-9155/57/7/2021.

[187] F. Hojjatollah and P. Punit, "Antenna Designs for Microwave Tissue Ablation," *Crit Rev Biomed Eng*, vol. 46, no. 6, pp. 495–521, 2018, doi: 10.1615/CritRevBiomedEng.2018028554.

[188] H. Fallahi, D. Clausing, A. Shahzad, M. O'Halloran, M. C. Dennedy, and P. Prakash, "Microwave antennas for thermal ablation of benign adrenal adenomas," *Biomed. Phys. Eng. Express*, vol. 5, no. 2, p. 025044, Feb. 2019, doi: 10.1088/2057-1976/ab068b.

[189] P. Prakash, M. C. Converse, J. G. Webster, and D. M. Mahvi, "An Optimal Sliding Choke Antenna for Hepatic Microwave Ablation," *IEEE Trans Bio Med Eng*, vol. 56, no. 10, pp. 2470–2476, Oct. 2009, doi: 10.1109/TBME.2009.2025264.

[190] R. D. Nevels, G. D. Arndt, G. W. Raffoul, J. R. Carl, and A. Pacifico, "Microwave catheter design," *IEEE Transactions on Biomedical Engineering*, vol. 45, no. 7, pp. 885–890, Jul. 1998, doi: 10.1109/10.686796.

[191] I. Longo, G. B. Gentili, M. Cerretelli, and N. Tosoratti, "A coaxial antenna with miniaturized choke for minimally invasive interstitial heating," *IEEE Transactions on Biomedical Engineering*, vol. 50, no. 1, pp. 82–88, Jan. 2003, doi: 10.1109/TBME.2002.807320.

[192] S. Pisa, M. Cavagnaro, P. Bernardi, and J. C. Lin, "A 915-MHz antenna for microwave thermal ablation treatment: physical design, computer modeling and experimental measurement," *IEEE Trans Biomed Eng*, vol. 48, no. 5, pp. 599–601, May 2001, doi: 10.1109/10.918599.

[193] H.-M. Chiu, A. Sanagavarapu, A. Weily, D. Guy, and D. Ross, "Analysis of a novel expanded tip wire (ETW) antenna for microwave ablation of cardiac arrhythmias," *Biomedical Engineering, IEEE Transactions on*, vol. 50, pp. 890–899, Aug. 2003, doi: 10.1109/TBME.2003.813541.

[194] J. C. Lin and Y.-J. Wang, "The cap-choke catheter antenna for microwave ablation treatment," *IEEE Transactions on Biomedical Engineering*, vol. 43, no. 6, pp. 657–660, Jun. 1996, doi: 10.1109/10.495286.

[195] S. Curto, M. Taj-Eldin, D. Fairchild, and P. Prakash, "Microwave ablation at 915 MHz vs 2.45 GHz: A theoretical and experimental investigation," *Medical Physics*, vol. 42, no. 11, pp. 6152–6161, 2015, doi: 10.1118/1.4931959.

[196] J. Sebek, S. Curto, R. Bortel, and P. Prakash, "Analysis of minimally invasive directional antennas for microwave tissue ablation," *International Journal of Hyperthermia*, vol. 33, no. 1, pp. 51–60, Jan. 2017, doi: 10.1080/02656736.2016.1195519.

[197] T. P. Ryan and C. L. Brace, "Interstitial microwave treatment for cancer: historical basis and current techniques in antenna design and performance," *Int J Hyperthermia*, vol. 33, no. 1, pp. 3–14, Feb. 2017, doi: 10.1080/02656736.2016.1214884.

[198] J. A. Pearce, "Models for Thermal Damage in Tissues: Processes and Applications," *CRB*, vol. 38, no. 1, 2010, doi: 10.1615/CritRevBiomedEng.v38.i1.20.

[199] J. A. Pearce, "Relationship between Arrhenius models of thermal damage and the CEM 43 thermal dose," in *Energy-based Treatment of Tissue and Assessment V*, Feb. 2009, vol. 7181, p. 718104. doi: 10.1117/12.807999.

[200] H. Fallahi, "Antenna and system design for controlled delivery of microwave thermal ablation," p. 203.

[201] M. Orbán, K. Kurin-Csörgei, A. M. Zhabotinsky, and I. R. Epstein, "Pattern Formation during Polymerization of Acrylamide in the Presence of Sulfide Ions," *J. Phys. Chem. B*, vol. 103, no. 1, pp. 36–40, Jan. 1999, doi: 10.1021/jp982968b.

[202] J. Sebek and P. Prakash, "Broadband dielectric properties of porcine lung as a function of temperature," in *2019 13th European Conference on Antennas and Propagation (EuCAP)*, Mar. 2019, pp. 1–5.

[203] "20645 TEMPOS_Manual_Web.pdf." Accessed: Aug. 18, 2020. [Online]. Available: http://publications.metergroup.com/Manuals/20645%20TEMPOS_Manual_Web.pdf

[204] "Thermal dose determination in cancer therapy - ScienceDirect." https://www.sciencedirect.com/science/article/abs/pii/0360301684903791?via%3Dihub (accessed Sep. 07, 2021).

[205] E. E. Marsh, A. Al-Hendy, D. Kappus, A. Galitsky, E. A. Stewart, and M. Kerolous, "Burden, Prevalence, and Treatment of Uterine Fibroids: A Survey of U.S. Women," *Journal of Women's Health*, vol. 27, no. 11, pp. 1359–1367, Sep. 2018, doi: 10.1089/jwh.2018.7076.

[206] A. Torre, A. Fauconnier, V. Kahn, O. Limot, L. Bussierres, and J. P. Pelage, "Fertility after uterine artery embolization for symptomatic multiple fibroids with no other infertility factors," *Eur Radiol*, vol. 27, no. 7, pp. 2850–2859, Jul. 2017, doi: 10.1007/s00330-016-4681-z.

[207] L. Zhang, W. Zhang, F. Orsi, W. Chen, and Z. Wang, "Ultrasound-guided high intensity focused ultrasound for the treatment of gynaecological diseases: a review of safety and efficacy," *International Journal of Hyperthermia*, vol. 31, no. 3, pp. 280–284, 2015.

[208] S. Jones, P. O'Donovan, and D. Toub, "Radiofrequency ablation for treatment of symptomatic uterine fibroids," *Obstetrics and gynecology international*, vol. 2012, 2012.

[209] Department of Obstetrics and Gynaecology, Queen Elizabeth Hospital, Jordan, Hong Kong, M. M. Lee, and T. Matsuzono, "Hysteroscopic intrauterine morcellation of submucosal fibroids: preliminary results in Hong Kong and comparisons with conventional hysteroscopic monopolar loop resection," *Hong Kong Medical Journal*, Jan. 2016, doi: 10.12809/hkmj154600.

[210] P. Gambadauro, J. Gudmundsson, and R. Torrejón, "Intrauterine Adhesions following Conservative Treatment of Uterine Fibroids," *Obstetrics and Gynecology International*, Nov. 28, 2011. https://www.hindawi.com/journals/ogi/2012/853269/ (accessed Jan. 19, 2021).

[211] D. Georgiou, A. Tranoulis, and T. L. Jackson, "Hysteroscopic tissue removal system (MyoSure) for the resection of polyps, sub-mucosal leiomyomas and retained products of conception in an out-patient setting: A single UK institution experience," *European Journal of Obstetrics & Gynecology and Reproductive Biology*, vol. 231, pp. 147–151, Dec. 2018, doi: 10.1016/j.ejogrb.2018.10.030.

[212] M. H. Emanuel, "New developments in hysteroscopy," *Best Practice & Research Clinical Obstetrics & Gynaecology*, vol. 27, no. 3, pp. 421–429, Jun. 2013, doi: 10.1016/j.bpobgyn.2012.11.005.

[213] A. Stogryn, "Equations for Calculating the Dielectric Constant of Saline Water (Correspondence)," *IEEE Transactions on Microwave Theory and Techniques*, vol. 19, no. 8, pp. 733–736, Aug. 1971, doi: 10.1109/TMTT.1971.1127617.

[214] N. Ellens and K. Hynynen, "Simulation study of the effects of near- and far-field heating during focused ultrasound uterine fibroid ablation using an electronically focused phased array: A theoretical analysis of patient safety," *Medical Physics*, vol. 41, no. 7, p. 072902, 2014, doi: 10.1118/1.4883777.

[215] C. Nyström, L. Forssman, and B. Roos, "Myometrial Blood Flow Studies in Carcinoma of the Corpus Uteri: A preliminary report on the clearance method using xenon 133," *Acta Radiologica: Therapy, Physics, Biology*, vol. 8, no. 3, pp. 193–198, Jan. 1969, doi: 10.3109/02841866909134450.

[216] J. Sebek, N. Albin, R. Bortel, B. Natarajan, and P. Prakash, "Sensitivity of microwave ablation models to tissue biophysical properties: A first step toward probabilistic modeling and treatment planning," *Medical physics*, vol. 43, no. 5, pp. 2649–2661, 2016.

[217] D. I. Galen, "Electromagnetic image guidance in gynecology: prospective study of a new laparoscopic imaging and targeting technique for the treatment of symptomatic uterine

fibroids," *BioMedical Engineering OnLine*, vol. 14, no. 1, p. 90, Oct. 2015, doi: 10.1186/s12938-015-0086-5.

[218] M. Cavagnaro, R. Pinto, and V. Lopresto, "Numerical models to evaluate the temperature increase induced byex vivomicrowave thermal ablation," *Phys. Med. Biol.*, vol. 60, no. 8, pp. 3287–3311, Mar. 2015, doi: 10.1088/0031-9155/60/8/3287.

[219] J. Chiang, S. Birla, M. Bedoya, D. Jones, J. Subbiah, and C. L. Brace, "Modeling and Validation of Microwave Ablations With Internal Vaporization," *IEEE Transactions on Biomedical Engineering*, vol. 62, no. 2, pp. 657–663, Feb. 2015, doi: 10.1109/TBME.2014.2363173.

[220] P. Faridi, P. Keselman, H. Fallahi, and P. Prakash, "Experimental assessment of microwave ablation computational modeling with MR thermometry," *Medical Physics*, vol. 47, no. 9, pp. 3777–3788, 2020, doi: https://doi.org/10.1002/mp.14318.

[221] P. Enterprises, "Flexible RG400 Coax Cable Double Shielded with Tan FEP Jacket," p. 3.

[222] "Flexible RG393 Coax Cable Double Shielded with Tan FEP Jacket." https://www.pasternack.com/flexible-rg393u-fep-jacket-silver-plated-copper-braid-over-silver-plated-copper-braid-outer-conductor-double-shielded-rg393-u-p.aspx (accessed Oct. 04, 2021).

Appendix A - Parametric Fitting for Fibroid Properties

We employed a two dimensional function to describe the dielectric properties of uterine fibroid tissue as a function of tissue temperature and frequency, similar to previous studies [63], [135]. Piecewise linear functions used to represent tissue dielectric properties as a function of temperature, T, and frequency, f, are listed in equation A1.

$$\hat{d}_{e,p}(f,T) = \begin{cases} \dfrac{b_0(f).(T_1-T)+b_1(f).(T-23)}{(T_1-23)}, & 23\,°C < T < T_1, \\[3mm] \dfrac{b_1(f).(T_2-T)+b_2(f).(T_1-23)}{(T_2-T_1)}, & T_1 < T < T_2, \\[3mm] b_2(f), & T_2 < T < 150\,°C, \end{cases} \qquad (A1)$$

Here, $\hat{d}_{e,p}(f,T)$ represents the parametrized quantity for the range of observed data values; T_1 and T_2 represent the temperatures between which the dielectric data take on different values. To capture the full range of fibroid dielectric data distribution, separate envelopes for the mean, maximum and minimum values were generated, denoted as mean, upper and lower envelopes. This process was conducted for both relative permittivity and for effective conductivity.

The fitting coefficients were modeled using the following quadratic functions.

$$b_0(f) = b_{01} \, . \, f^2 + \ b_{02} \, . \, f + b_{03} \, ,$$

$$b_1(f) = b_{11} \, . \, f^2 + \ b_{12} \, . \, f + b_{13} \, ,$$

$$b_2(f) = b_{21} \, . \, f^2 + \ b_{22} \, . \, f + b_{23} \, ,$$

The fitting coefficients were defined separately for each envelope of fibroid tissue separately for relative permittivity, ε_r, and effective conductivity, σ_{eff}, values. Least squares optimization technique [63] was employed to estimate the fitting coefficients for the given transition temperatures T_1 and T_2.

Appendix B - Parametric Fitting Coefficients of Fibroids as a Function of Thermal Isoeffective Dose (CEM43)

Table B1 provides the fitting parameters for the parametric distribution of human uterine fibroid dielectric data with respect to the thermal dose as illustrated in Figure 3.8.

Table B1. Fitting parameters for dielectric properties of fibroids with respect to thermal dose. The fitting co-efficient, $b_{01}, b_{02}, b_{03}, b_{11}, b_{12}, b_{13}, b_{21}, b_{22}, b_{23}$, are defined for the relative permittivity, ε_r and effective conductivity, σ_{eff} for the three envelopes (mean, upper and lower) separately. In addition, corresponding transition logarithmic thermal doses TD_1 and TD_2 are also presented.

Parameters	Mean Envelope		Upper Envelope		Lower Envelope	
	For ε_r	For σ_{eff}	For ε_r	For σ_{eff}	For ε_r	For σ_{eff}
b_{01}	0.1067	0.0866	0.0803	0.1094	0.2296	0.0870
b_{02}	-2.4011	0.2914	-1.9200	0.2353	-3.5787	0.2102
b_{03}	57.552	0.6933	65.423	0.9811	48.799	0.5387
b_{11}	0.4571	0.0082	0.4591	-0.0093	0.4260	0.0131
b_{12}	-4.4374	0.2553	-3.9518	0.2745	-4.3187	0.0848
b_{13}	50.073	1.7368	51.778	2.6133	41.430	1.2501
b_{21}	0.0649	-0.0048	0.2740	-8.931×10^{-4}	2.487×10^{-4}	-4.1673×10^{-4}
b_{22}	-0.7031	0.0674	-2.8765	0.1453	0.0467	0.0018
b_{23}	6.2797	0.1711	21.791	0.3982	1.2022	0.0539
TD_1	15	21	21	22	16	18
TD_2	24	23	25	23	20	18

Appendix C - Fabrication of 5.8 GHz MWA applicator

List of Materials

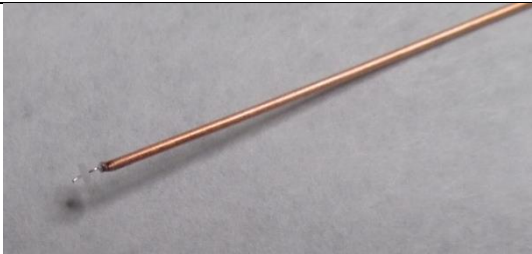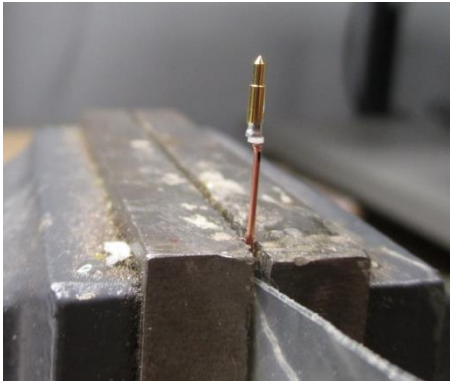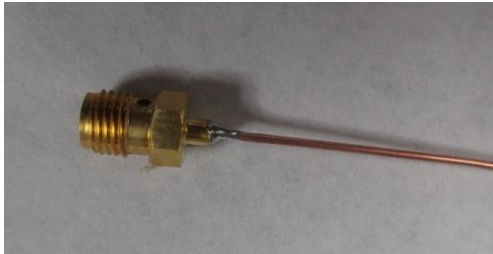| Sr. No	Materials	Details
1.	UT-34 Coaxial Cable	Microstock inc. https://www.microstock-inc.com/pdfshow01.php?item=UT-034
2.	SMA connector	From pasternack SMA (female) jack for UT-034
3.	Copper Tape	From Digikey (3M (TC) 1/2-6-1125)
4.	Silicone	Cotronics Duraseal 1533, www.cotronics.com/vo/cotr/rm_silicones.htm
5.	Polyimide Tubes	American Durafilm
6.	Y adaptor	Y Connector with Two Female Luers Technical Features:160 inch (4.1 mm) ID http://www.qosina.com/y-connector-with-two-female-luers-11658
7.	Hemostasis valve	Qosina part
8.	Thin metal wire	0.1 mm diameter
9.	Solder equipment	
10.	Epoxy	Jbweld clear weld
11.	PTFE inflow tube	Zeus inc. 0.056" etched liner

Schematics of Applicator
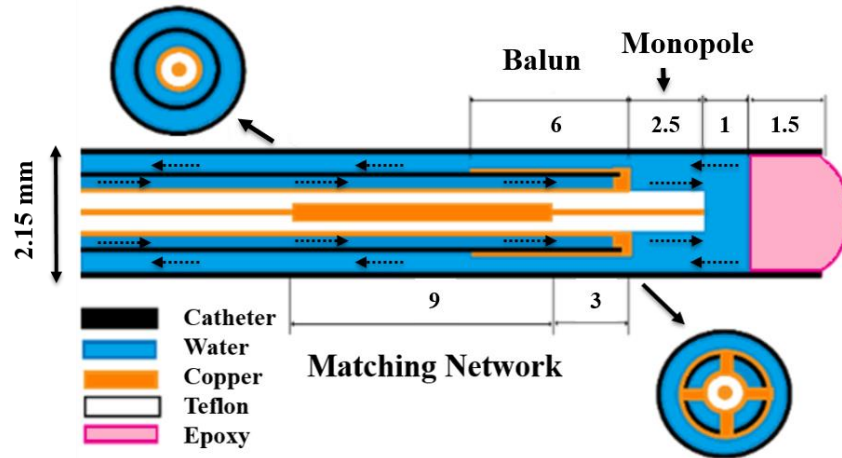
a. Applicator model schematics
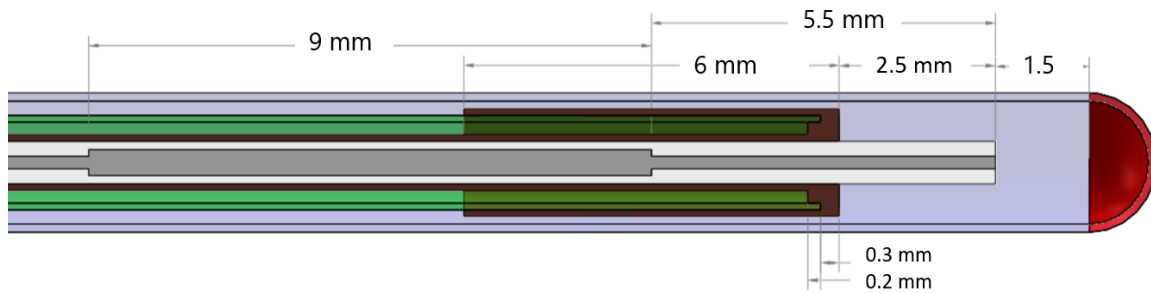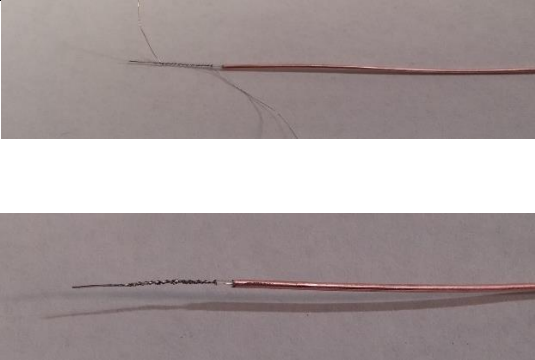

b. Applicator fabrication design
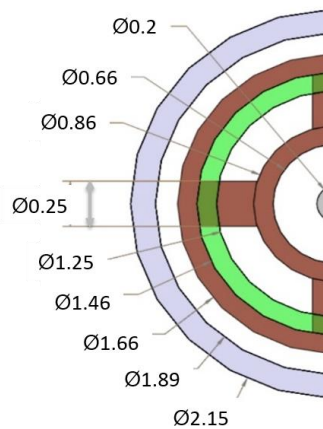
c.

d. Cross-sectional view of applicator fabrication design illustrating water cooling below the balun

Fabrication Procedure

Sr. No	Procedure	Details
Coaxial Cable and Connector At one end of the coaxial cable, SMA connector is placed		
1.	Take 20 cm of UT-34 coaxial cable.	
2.	Attach the SMA connector on one end of the cable • Remove 2mm of outer conductor and dielectric. • Add the Teflon piece of connector into the part of the cable that has been stripped. • Introduce the cable in one of the pin-connector tip. • Apply solder in the pin-connector holes. • Be careful and do not solder the edge of the pin because you can easily create a short circuit. • Introduce the pin and the cable to the part of the connector with the SMA connection and apply solder to the outer cable to connector. • Apply glue in the holes of the connector. • With a digital multi-meter check if there is any short circuit between the pin inside the connector and outer conductor.	

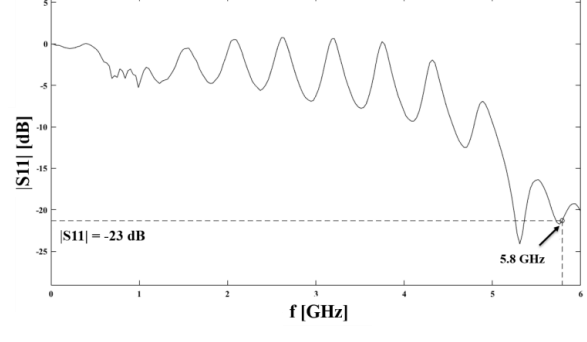| **Monopole and Matching Network**		
The matching network has to be built inside the coaxial cable.		
3.	At the end of the cable which is opposite to the connector side, remove 16.5 mm (2.5 mm for the monopole and 3+9+2 mm for the matching network) of outer conductor of coaxial cable.	
4.	Remove 5.5 mm of dielectric from the distal end of the cable and save it for later use.	
5.	Now remove 9 mm of dielectric which will leave only 2 mm of dielectric on the cable.	
6.	Coil a 0.1 mm wire around the inner conductor of the cable over the 9 mm area and solder it uniformly over the wire. Check the diameter to be < 0.5 mm (ideally 0.4 mm) after soldering otherwise use Dremel for smoothing it to < 0.5 mm diameter.	
7.	Put 5.5 mm dielectric extracted in step 4 over the inner conductor.	
8.	Put silicone evenly over the 9 mm area. And let it dry for about 60 minutes.	
9.	Put the Copper tape of thickness 0.15 mm over the silicone, 3 mm of the dielectric and 2 mm on the proximal end of the matching network.	
10.	Check continuity and insulation of the coaxial cable with the digital	

	multimeter. The matching network and the monopole are ready. Go to step 27 for return loss measurement.	
Water cooling (Inflow)		
11.	For the inflow channel, put the hemostasis valve over the shaft and lock it.	
12.	Put the inflow tube (PTFE Streamliner/Polyimide tube) of length such that the one end of the tube is 1 mm behind the junction. The second end of the inflow tube should end right next to the 90 degree inflow section inside the hemostasis valve. The internal diameter of tube is ~0.056".	
13.	At the proximal end of the inflow tube, make a 45° cut and slide it into the Touhy Boast Adapter (Blue end) such that it is not touching the top most part which would otherwise clog the flow in the hemostasis valve.	
14.	Put epoxy carefully between the outer surface of inflow tube and the hemostasis valve. Be careful, not to put too much epoxy to avoid clogging. Leave it for at least 1 h. to dry.	
15.	Epoxy the hemostasis valve to the SMA connector. Care should be taken not to put too much epoxy that it clogs the threads of the SMA.	

Balun		
16.	Leave 1 mm from the monopole junction and put 7 mm of silicone over the copper tape.	
17.	Put copper tape 5.5 mm over the silicone. Leave 0.5 mm for the solder at the junction point. Solder the copper tape at least on 1 point near the junction at the outer conductor of Coaxial cable such that there is space for the inflow of water.	
18.	Check the insulation and continuity of the cable with digital multi-meter. Go to step 27 for return loss measurement.	
Water cooling (Outflow)		
19.	For the outflow channel, put Y connector and lock it with the hemostasis valve.	
20.	Take a 2.15 mm diameter polyimide tube of appropriate length and place it 1 cm inside the Y connector and cut its length 3 mm beyond the monopole (1 mm space and 2 mm for epoxy).	
21.	Epoxy the proximal end of the tube with the Y-connector and leave it for at least 1 hr to dry.	
22.	Carefully epoxy the distal end of the outer polyimide tube. Place the applicator in an upright position with the help of clips and stand and carefully put a small amount of epoxy with a Q-tip	

169

	such that the epoxy does not climb to the monopole and there should be at least 1-1.5 mm gap between the monopole and the epoxy. Leave it to dry for at least 1 hr.	
Insertion tip		
23.	Take a piece of inner conductor wire and try to place it with epoxy at the distal end of the applicator. Create a blob of epoxy and leave it to dry. Dremel it after it has been completely dried into at 120° angles from three sides thus creating a pointed tip of the applicator. The other method of creating an insertion tip is to use a sharp metal tips of a suitable size and epoxy it at the distal end of applicator. Please be careful that there should be no epoxy in front of the monopole.	
Checking the water flow		
24.	Connect the water circuit (applicator, pump, tubing and 500 ml beaker).Check and measure the flow rate.	
Check the antenna return loss		
25.	Calibrate the Vector Network Analyzer for S11 measurement (Short, Open and Load).	

26.	Put the applicator (already connected with water flow) in a 1000 ml water beaker. Measure S11 inside the water and check if the S11 < -10 dB at 5.8 GHz frequency.	
27.	For intermediate checking of S11, measure the S11 after step 13 i.e. before connecting the water channels. Follow step 23 then place the applicator in a water beaker and check if the S11 < -10 dB at 5.8 GHz frequency. Afterwards, dry the applicator carefully and proceed to the Step 14.	

The 5.8 GHz water-cooled omnidirectional microwave ablation applicator is ready.

Appendix D - Fitting coefficients of Dielectric Properties of Gel Phantoms

Piecewise linear functions are used to model the temperature dependent dielectric properties of the thermochromic tissue mimicking gel phantom which are described in the following equations.

$$\hat{d}_{e,p}(f,T) = \begin{cases} \dfrac{b_0(f).(T_1-T)+b_1(f).(T-22)}{(T_1-31)}, & 22\,°C < T < T_1, \\[3mm] \dfrac{b_1(f).(T_2-T)+b_2(f).(T_1-22)}{(T_2-T_1)}, & T_1 < T < T_2, \\[3mm] b_2(f), & T_2 < T < 120\,°C, \end{cases}$$

Where $\hat{d}_{e,p}(f,T)$ is the parametrized envelop indicating the range of observed data values at 5.8 GHz. $T_1 = 86\,°C\ and\ T_2 = 96\,°C$ are the transition temperatures within the heating temperature intervals. The frequency dependent fitting coefficients are modelled using the quadratic equations as follows.

$b_0(f) = b_{01}\,.\,f^2 + b_{02}\,.\,f + b_{03}\,,$

$b_1(f) = b_{11}\,.\,f^2 + b_{12}\,.\,f + b_{13}\,,$

$b_0(f) = b_{21}\,.\,f^2 + b_{22}\,.\,f + b_{23}\,,$

Where the fitting coefficients i.e. $b_{01}, b_{02}, b_{03}, b_{11}, b_{12}, b_{13}, b_{21}, b_{22}, b_{23}$ for mean envelope of gel phantom are defined in the table D.1 for the relative permittivity, ε_r, and effective electrical conductivity, σ, values.

Table D.1. Fitting coefficients for dielectric properties of gel phantom.

Coefficients	for ε_r	for σ
b_{01}	0.0353	0.1365
b_{02}	-1.0755	0.0801
b_{03}	68.87	1.6407
b_{11}	0.0848	0.0237
b_{12}	-0.1469	-0.0817
b_{13}	43.9679	3.0111
b_{21}	0.2308	2.857 x 10⁻⁴
b_{22}	-1.4337	-0.0295
b_{23}	20.776	0.3482
$T_1(°C)$	87	86
$T_2(°C)$	97	96

Appendix E - Temperature Dependent Properties used in Chapter 5

Dielectric Properties

In the study [63], piecewise linear functions are used to model the temperature dependent dielectric properties of the tissues which are described in the following equations.

$$\hat{d}_{e,p}(f,T) = \begin{cases} \dfrac{b_0(f).(T_1-T)+b_1(f).(T-31)}{(T_1-31)}, & 31\,°C < T < T_1, \\[2ex] \dfrac{b_1(f).(T_2-T)+b_2(f).(T_1-31)}{(T_2-T_1)}, & T_1 < T < T_2, \\[2ex] b_2(f), & T_2 < T < 150\,°C, \end{cases}$$

Where $\hat{d}_{e,p}(f,T)$ is the parametrized envelop indicating the range of observed data values at 5.8 GHz. $T_1 = 96\,°C\ and\ T_2 = 118\,°C$ are the transition temperatures within the heating temperature intervals. The frequency dependent fitting coefficients are modelled using the quadratic equations as follows.

$b_0(f) = b_{01} \cdot f^2 + b_{02} \cdot f + b_{03}$,

$b_1(f) = b_{11} \cdot f^2 + b_{12} \cdot f + b_{13}$,

$b_0(f) = b_{21} \cdot f^2 + b_{22} \cdot f + b_{23}$,

Where the fitting coefficients i.e. $b_{01}, b_{02}, b_{03}, b_{11}, b_{12}, b_{13}, b_{21}, b_{22}, b_{23}$ for mean envelope of bovine muscle [202] are defined in the table E.1 for the relative permittivity, ε_r, and effective electrical conductivity, σ, values.

Table E.1. Fitting coefficients for dielectric properties of bovine muscle.

Coefficients	for ε_r	for σ
b_{01}	0.4161	0.0495
b_{02}	-4.4579	0.3234
b_{03}	56.5798	0.8783
b_{11}	0.6746	-0.0141
b_{12}	-5.9807	0.3283
b_{13}	41.6728	1.0382
b_{21}	0.0581	-0.0083
b_{22}	-0.5843	0.0632
b_{23}	7.4576	-0.0184

Thermal Properties

In the study [126], the volumetric heat capacity, ρc is given by the following piecewise linear equation.

$$\rho c = \begin{cases} \rho_0 c_0, & T \leq T_1 \\[2mm] \frac{\rho_0 c_0 + \rho_{vap} c_{vap}}{2} + \rho_w LC \frac{1}{T_u - T_1}, & T_1 \leq T \leq T_u \\[2mm] \rho_{vap} c_{vap}, & T_u < T \end{cases}$$

Where volumetric heat capacity of normal tissue, $\rho c = 4$ MJ m^{-3} °C^{-1} [151], volumetric heat capacity of vaporized tissue, $\rho_{vap} c_{vap} = 0.6$ MJ m^{-3} °C^{-1}, density of water, $\rho_w = 1000$ kgm^{-3}, latent heat of vaporization, L = 2257x10^3 Jkg^{-1} and tissue water fraction, C = 0.73. $T_1 = 95$ °C and $T_u = 105$ °C are the transition temperatures for the volumetric heat capacity function.

The temperature dependence of thermal conductivity k is given by the following piecewise continuous function [126].

$$k(T) = \begin{cases} k_0 + \Delta k \ [T - T_0], & T \leq 100 \ °C, \\[2mm] k_0 + \Delta k \ [100 - T_0], & T > 100 \ °C, \end{cases}$$

Where baseline thermal conductivity for muscle tissue is $k_0 = 0.5$ W m^{-1} °C^{-1} [151], change in thermal conductivity w.r.t temperature, $\Delta k = 0.003$ W m^{-1} °C^{-1} and the baseline temperature $T_0 = 37$ °C. In the study [126], the temperature dependence of blood perfusion is such that initially the blood perfusion rises due to the body's homeostatic mechanism and tries to lower the local temperature. However, at $T_0 = 60$ °C due to the collapse of vasculature within the coagulation zone, the perfusion stops. The dependence of blood perfusion term is given by the following equation.

$$m_{bl} \ c_{bl} = \begin{cases} m_{bl} c_{bl}, & T < T_0, \\[2mm] 0, & T \geq T_0, \end{cases}$$

Where m_{bl} is the temperature dependent blood perfusion in fibroid and surrounding myometrium = 1.89 kg m^{-3} s^{-1} [214] [215] and c_{bl} is the specific heat capacity of blood = 3617 J kg^{-1} °C^{-1} [151].